

A STUDY OF THE ELECTRONIC AND OPTICAL PROPERTIES OF  
VISIBLE STRAINED QUANTUM WELL DIODE LASERS

By  
YOUNGSOH PARK

A DISSERTATION PRESENTED TO THE GRADUATE SCHOOL  
OF THE UNIVERSITY OF FLORIDA  
IN PARTIAL FULFILLMENT OF THE REQUIREMENTS  
FOR THE DEGREE OF DOCTOR OF PHILOSOPHY

UNIVERSITY OF FLORIDA

1994

## ACKNOWLEDGEMENTS

I would like to express my deep gratitude to my advisor Dr. Peter S. Zory for his expert guidance and constant encouragement throughout my study. I would also like to thank Dr. Sheng S. Li, Dr. Gijs Bosman, Dr. Ramacant Srivastava, and Dr. Timothy J. Anderson for serving on my supervisory committee.

I am very grateful to Dr. D. Bour at Xerox Palo Alto Research Center and Dr. M. Haase at 3M Company for having supplied us with GaInP and CdZnSe quantum well laser materials. I wish to express thank to Dr. Masahiro Asada at Tokyo Institute of Technology for fruitful discussions for line shape functions.

Thanks are extended to my fellow graduate students and researchers: particularly Dr. Yu Guan, Dr. Gab-gyu Lim, Maj. Mike Grove, Mr. Hyoun Soo Kim, Mr. Sang Kook Han, Mr. Doug Hudson, Capt. Craig Largent, Mr. Chi-Lin Young, and Mr. Chih-Hung Wu for the informative discussions.

I wish to thank Mr. J. Chamblee and Mr. J. Hales of the Microelectronics Laboratory for all the technical assistance they provided over the years. I also thank Mr. A. Herlinger for machining of components used in my experimental set-ups.

I would like to acknowledge Samsung Electronics for financial support.

This work was also supported by ARPA/ONR Grant N00014-92-J-1895.

I am indebted to my parents for their emotional supports during all the years of my life. I also thank my parents-in-law for their encouragements.

Last, but not least, I thank my wife Sohyoung and my daughters Sumin and Sujin for their patience and indispensable support during this work.

## TABLE OF CONTENTS

	<u>Page</u>
ACKNOWLEDGEMENTS .....	ii
ABSTRACT.....	vi
CHAPTERS	
I. INTRODUCTION.....	1
II. THE MULTIBAND EFFECTIVE MASS THEORY AND ENERGY DISPERSION .....	11
2.1. Introduction .....	11
2.2. The Multiband Effective Mass Theory and Valence Band Mixing .....	12
2.3. Carrier Potential well .....	16
2.3.1. The Model Solid Theory .....	17
2.3.2. The Electron Affinity Rule .....	18
2.3.3. The Strain Effect .....	20
2.3.4. The Potential Well Structure of GaInP and CdZnSe QW Lasers .....	22
2.4. Energy Dispersion .....	29
2.5. Summary .....	35
III. POLARIZATION ANISOTROPY OF RED LASERS .....	36
3.1. Introduction .....	36
3.2. Transition Matrix Element .....	37
3.3. Polarization Anisotropy .....	46
3.4. Experiment .....	48
3.5. Discussion .....	61



IV. TEMPERATURE DEPENDENCE OF THE THRESHOLD CURRENT DENSITY OF CdZnSe BLUE-GREEN QUANTUM WELL LASERS .....	65
4.1. Introduction .....	65
4.2. Spontaneous Emission rate and Gain Spectra .....	66
4.3. Intraband Relaxation and Line Shape Function .....	72
4.4. Temperature Dependence of the Threshold Current Density of CdZnSe Blue-Green Quantum Well Lasers .....	76
4.5. Summary .....	91
V. DUAL WAVELENGTH OPERATION OF AlGaAs AND CdZnSe QW LASERS .....	93
5.1. Introduction .....	93
5.2. Dual Wavelength Operation of AlGaAs QW Lasers .....	94
5.3. Dual Wavelength Operation of CdZnSe QW Lasers .....	104
5.4. Summary .....	113
APPENDIX .....	116
REFERENCES.....	117
BIOGRAPHICAL SKETCH.....	123

Abstract of Dissertation Presented to the Graduate School of  
the University of Florida in Partial Fulfillment of the  
Requirements for the Degree of Doctor of Philosophy

A STUDY OF THE ELECTRONIC AND OPTICAL PROPERTIES OF  
VISIBLE STRAINED QUANTUM WELL DIODE LASERS

By

YOUNGSOH PARK

April, 1994

Chairman: Peter S. Zory  
Major Department: Electrical Engineering

A theoretical and experimental study of GaInP and CdZnSe visible strained quantum well (QW) lasers is presented. The strain in the QW active layer is either compressive or tensile and is due to the difference in lattice parameter between the QW and the adjacent sandwiching barrier layers.

Energy vs. in-plane  $k$  vector dispersion curves for strained QW active layers are obtained using the multiband effective mass theory (or  $k \cdot p$  method). The carrier potential well structures are estimated using the electron affinity rule for CdZnSe and the model solid theory for GaInP QW lasers.

The Luttinger-Kohn Hamiltonian is derived and the Schrodinger-like equations are solved numerically by using the finite difference method.

The spontaneous emission polarization anisotropy of  $\text{Ga}_x\text{In}_{1-x}\text{P}$  strained QW lasers for  $x=0.3, 0.4$  (compressive strain),  $x=0.5$  (lattice matched), and  $x=0.6$  (tensile strain) were measured and compared to predictions. The correlation between threshold current density ( $J_{\text{th}}$ ) and the energy dispersion curve of the strained QW are also discussed.

Incorporating the dispersion curves calculated from the  $\mathbf{k} \cdot \mathbf{p}$  method into electron-hole plasma (EHP) theory, the temperature dependence of  $J_{\text{th}}$  of CdZnSe strained QW lasers is calculated. Good agreement with experiment is obtained up to 300K provided a hole-hole scattering time of 60 femtoseconds is assumed. Above 300K, the measured  $J_{\text{th}}$  is much higher than predicted, the discrepancy being due most likely to carrier leakage.

To further test the validity of EHP theory in predicting the lasing behavior of CdZnSe QW lasers, dual wavelength lasers (both CdZnSe and AlGaAs) were designed, fabricated, and characterized. For the AlGaAs QW lasers, dual wavelength operation was clearly demonstrated. For the CdZnSe QW lasers, dual wavelength laser operation could not be obtained although below threshold spectral data showed a double peak feature.



## CHAPTER I INTRODUCTION

Quantum confinement of carriers in a semiconductor quantum well (QW) leads to the formation of discrete energy levels and a modified density of states function. A fundamental advantage is that QW lasers deliver more gain per injected carrier than conventional double heterojunction (DH) lasers, which results in lower threshold currents. In addition, the spectral gain becomes quite anisotropic with respect to transverse-electric (TE) and transverse magnetic (TM) polarization when compared to that of the bulk semiconductor lasers.

In the early years of semiconductor lasers, it was thought that the lattice constants of the active and barrier layer should be matched in order to make a high quality heterostructure diode laser. However, recent advances in epitaxial growth have allowed a mismatch of the lattice constants between the QW and the barrier layer. The strain due to the lattice mismatch perturbs the crystal symmetry and leads to the prospect of an artificial modification of the electronic structure or band structure of semiconductor materials. The combination of strain and quantum confinement in the valence band can lead to substantially more favorable energy dispersion curves for laser action than those existing in the unstrained semiconductor crystal.

In recent years, the conjecture [Yabl 86, Adam 86] that strained active layers in QW lasers should lead to improved performance compared with lattice matched lasers has been verified with visible lasers by experiment. In fact, a strained QW design was utilized in fabricating the world's first blue-green diode lasers [Haas 91]. Moreover, it has been shown that strained QW lasers can have reliability as well as performance characteristics that are substantially superior to unstrained devices. In this study, GaInP (red) and CdZnSe (blue-green) strained QW lasers are analyzed. The applications and the fundamental characteristics to be analyzed are listed in Table 1.1.

In semiconductor lasers, the condition required for positive gain is

$$E_g < h\nu < E_{fc} - E_{fv} \quad (1.1)$$

where  $E_g$  is the band gap energy,  $h\nu$  is the photon energy, and  $E_{fc}(E_{fv})$  is the quasi-Fermi level for the conduction (valence) band. The condition in Eq. (1.1) was first pointed out by Bernard and Duraffourg [Bern 61]. When the quasi-Fermi level separation is equal to the band gap energy, the material will become transparent for the photon energy equal to the band gap. The electron and hole density that is required to provide this separation is known as the transparency carrier density,  $N_{tr}$ , and its magnitude is fundamentally related to the densities of states of conduction ( $\rho_c$ ) and valence band ( $\rho_v$ ) of a given material. The transparency condition is illustrated for  $m_v=m_c$  and  $m_v>m_c$  where  $m_c(m_v)$  is the effective mass of the conduction (valence) band in Fig. 1.1. In the latter case, the asymmetry of the density of state shifts both



Table 1.1  
The Characteristics of the Red and the Blue-Green Lasers

	Red Lasers	Blue-Green Lasers
Material (QW/Barrier)	$\text{Ga}_x\text{In}_{1-x}\text{P}/$ $(\text{Al}_{0.6}\text{Ga}_{0.4})_{0.5}\text{In}_{0.5}\text{P}$	$\text{Cd}_{.2}\text{Zn}_{.8}\text{Se}/$ $\text{ZnS}_{.06}\text{Se}_{.94}$
Wavelength	707nm (x=0.3) 630nm (x=0.6)	496nm (85K) 516nm (294K)
Applications	<ul style="list-style-type: none"> <li>• Optical bar code scanning</li> <li>• Optical Recording</li> <li>• He-Ne laser substitutes</li> <li>• Laser printers</li> </ul>	<ul style="list-style-type: none"> <li>• Optical memory</li> <li>• Compact disk player optical source</li> <li>• Under sea communications</li> <li>• Color display</li> </ul>
Characteristics	Polarization Anisotropy	Temperature Dependence of $J_{th}$

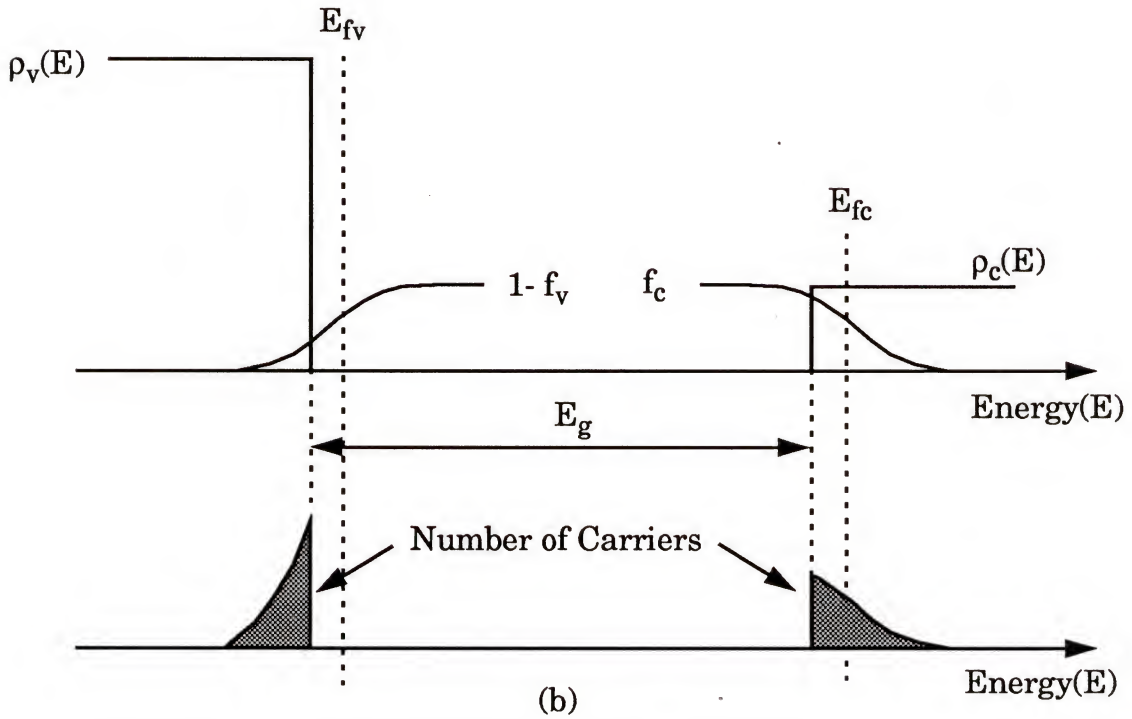
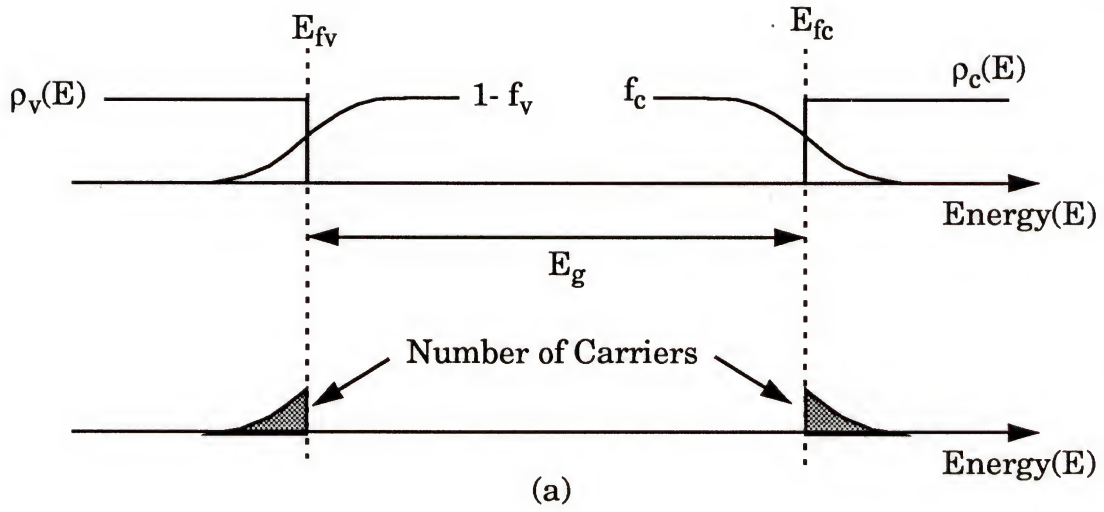


Figure 1.1 Band edge transparency condition ( $E_{fc} - E_{fv} = E_g$ ) for (a)  $m_c = m_v$  and (b)  $m_c < m_v$

Fermi functions toward the conduction band in order to maintain equal numbers of carriers in both bands. The result is a larger  $N_{tr}$  than in the symmetric case.

In most semiconductor lasers, there is a serious asymmetry between the light conduction band effective mass and the very heavy valence band effective mass. Ideally both masses should be as light as possible. The density of states would be very small and the carrier density required for the transparency would be minimized. Due to the heavy valence band effective mass, the hole quasi-Fermi level is above the top of the valence band and the hole distribution is classical. This situation is illustrated in Fig. 1.2(a) and the more ideal situation is illustrated in Fig. 1.2(b). Due to the effective mass asymmetry of the typical III-V semiconductor as illustrated in Fig. 1.2(a), the quasi-Fermi levels are offset from the symmetrical position by an energy  $\delta$ . This requires an excess population of carriers as is evident by comparing the electron Fermi level in Fig. 1.2(a) and (b). When both hole and electron masses are light as in Fig. 1.2(b), the transparency condition can be achieved at lower carrier injection.

The valence band effective mass can be reduced significantly by applying strain in the QW layer. The strain splits the degeneracy of the heavy and light hole states, accessing a wide range of subband structures, including the possibility of the highest valence subband being light hole-like, of significant benefit for semiconductor lasers in terms of the threshold

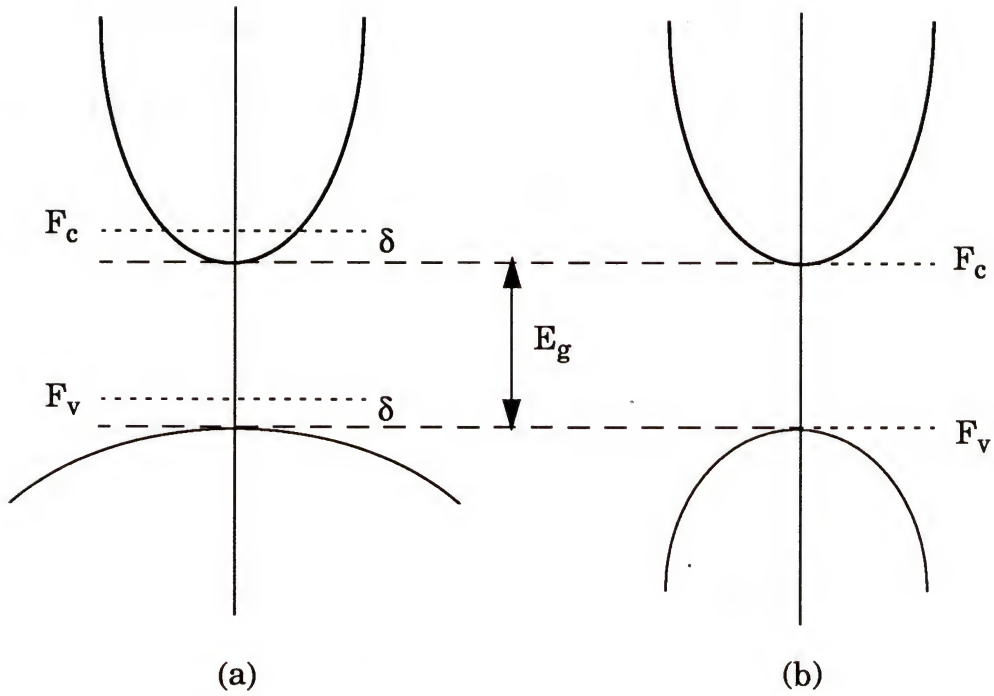


Figure 1.2 The  $E$  vs.  $k$  band structure diagram of (a) a typical III-V semiconductor and (b) an idealized strained QW.



current density. Moreover, the Auger recombination and the intervalence band absorption, which are the major loss mechanisms in long wavelength lasers, can be reduced [Yabl 86, Wang 93].

Another change accompanied by the strain effect involves the polarization anisotropy. The transition probability between the conduction band and heavy hole band is greatest for TE polarization. Conversely, TM polarization is strongest for the conduction band and the light hole band transition. For most unstrained semiconductor lasers, the heavy hole band is the ground state. Therefore, the heavy hole population is most easily inverted and the gain polarization asymmetry of the heavy hole transition favors the TE mode over TM mode. If the quantum well active layer is strained, the polarization anisotropy is modified. For instance, Bour *et al* [Bour 93] fabricated and analyzed red light emitting  $\text{Ga}_x\text{In}_{1-x}\text{P}/(\text{Al}_{0.6}\text{Ga}_{0.4})_{0.5}\text{In}_{0.5}\text{P}$  strained QW lasers grown on GaAs substrates. For the Gallium (Ga) mole fraction ( $x$ ) less than 0.5, the quantum well layer is compressively strained and the heavy hole is the ground state. In this case, TE mode emission dominates. On the other hand, for the tensile strain ( $x$  greater than 0.5), the light hole is the ground state and the emission is predominantly TM. In either case, the polarization anisotropy is important in order to predict the diode laser performance.

In this study, a theoretical and experimental study of  $\text{Ga}_x\text{In}_{1-x}\text{P}/(\text{Al}_{0.6}\text{Ga}_{0.4})_{0.5}\text{In}_{0.5}\text{P}$  (red) and  $\text{Cd}_{0.2}\text{Zn}_{0.8}\text{Se}/\text{ZnS}_{0.6}\text{Se}$  (blue-green) strained



QW lasers is presented. For  $\text{Ga}_x\text{In}_{1-x}\text{P}$  QW lasers, polarization anisotropy of the compressive as well as the tensile strain is analyzed. The electron hole plasma (EHP) model, that optical gain is derived from k-conserved stimulated processes between free electrons and holes in quantum well subbands, is used for CdZnSe QW lasers to predict the temperature dependence of the threshold current density and compared to the recently demonstrated [Gain 93] experimental results.

In chapter II, the energy vs. in-plane dispersion curves for red and blue-green lasers are calculated using the multiband effective mass theory. The Luttinger-Kohn Hamiltonians are derived in a simplified form and the Schrodinger equations are solved using the finite difference method (FDM). The theories for a heterojunction band lineup are introduced and the strain effects on the band offsets are discussed. The carrier potential wells for  $\text{Ga}_x\text{In}_{1-x}\text{P}/(\text{Al}_{0.6}\text{Ga}_{0.4})_{0.5}\text{In}_{0.5}\text{P}$  and  $\text{Cd}_{0.2}\text{Zn}_{0.8}\text{Se}/\text{ZnS}_{0.6}\text{Se}$  strained QW lasers are derived with the model solid theory and the electron affinity rule, respectively.

In chapter III, the polarization anisotropy of  $\text{Ga}_x\text{In}_{1-x}\text{P}/(\text{Al}_{0.6}\text{Ga}_{0.4})_{0.5}\text{In}_{0.5}\text{P}$  strained QW lasers for  $x=0.3, 0.4$  (compressive strain),  $x=0.5$  (lattice matched), and  $x=0.6$  (tensile strain) is described in detail. Based on the energy dispersion curves derived in chapter II, the peak emission differences between the TE and TM polarization are calculated and compared to the experiment. The threshold current densities are measured and

discussed in terms of the in-plane effective masses and quasi-Fermi levels.

In chapter IV, the temperature dependence of threshold current density of  $\text{Cd}_{0.2}\text{Zn}_{0.8}\text{Se}/\text{ZnS}_{0.6}\text{Se}$  is predicted and compared to the experiment. A modified Lorentzian line shape function is used to include the intraband relaxation process caused by carrier scattering. The spontaneous emission rate and the spectral gain are calculated based on the energy dispersion curve derived in chapter II. The peak gain ( $g$ ) vs. the current density ( $J$ ) curves at various temperatures are derived by relating  $g$  and  $J$  at each carrier density. The temperature and the carrier density are specified first, and then the spontaneous emission rate and the spectral gain are calculated. The corresponding  $J$  is calculated by integrating the spontaneous emission rate and  $g$  is determined from the maximum of the spectral gain. The threshold current densities at various temperatures are determined from the  $g$ - $J$  curve by estimating the threshold gain.

There have been reports [Ding 90, Ding 92] that the optical gain in CdZnSe QW lasers is not derived from stimulated processes between free electrons and holes but between bound electron and holes or excitons. However, the predicted temperature dependence of threshold current density of  $\text{Cd}_{0.2}\text{Zn}_{0.8}\text{Se}/\text{ZnS}_{0.6}\text{Se}$  QW lasers is in good agreement with experiment without any excitonic effect consideration. To further test the validity of EHP theory in predicting the lasing behavior of CdZnSe QW lasers, dual wavelength lasers (both CdZnSe and AlGaAs) were designed, fabricated, and

characterized as discussed in chapter V. For the AlGaAs QW lasers, dual wavelength operation was clearly demonstrated. For the CdZnSe QW lasers, the spectral data appeared to show dual wavelength operation although with considerably reduced resolution.



## CHAPTER II

### THE MULTIBAND EFFECTIVE MASS THEORY AND ENERGY DISPERSION

#### 2.1 Introduction

The multiband effective mass theory, often called  $k \cdot p$  method, has been widely used to treat problems involving valence band and strongly non-parabolic bands in narrow gap semiconductors [Dres 55, Lutt 55, Kane 57, Piku 60]. In recent times, it has been used to describe quantum wells and superlattices [Whit 81, Bast 81, Alta 85] and regarded as the single most important theoretical procedure for predicting and analyzing the energy band structures of semiconductors.

In order to calculate the energy vs. in-plane  $k$  vector dispersion of  $\text{Ga}_x\text{In}_{1-x}\text{P}/(\text{Al}_{0.6}\text{Ga}_{0.4})_{0.5}\text{In}_{0.5}\text{P}$  and  $\text{Cd}_{0.2}\text{Zn}_{0.8}\text{Se}/\text{ZnS}_{0.6}$  QW lasers with the multiband effective mass theory, one must first define the carrier confinement, or potential well structure of these material systems. The carrier confinement can be determined either by experiment such as magneto-optical spectroscopy or by theory such as the model solid theory [Van 86, Van 88, Van 89] or the electron affinity rule. Since the experimental data are not known for these materials, the carrier confinement was estimated theoretically. Moreover, the lattice constants of the QW layers of

these structure are different from those of the barrier layers, and hence, the QW layers are strained. Since the strain perturbs the band structure, it should be taken into account in the carrier confinement calculation section.

In section 2.2, the band effective mass theory is developed from the fundamental Bloch theorem and in section 2.3, the carrier potential wells for  $\text{Ga}_x\text{In}_{1-x}\text{P}/(\text{Al}_{0.6}\text{Ga}_{0.4})_{0.5}\text{In}_{0.5}\text{P}$  and  $\text{Cd}_{0.2}\text{Zn}_{0.8}\text{Se}/\text{ZnS}_{0.6}$  QW laser structures are derived with the strain effect considered. The energy vs. in-plane  $k$  vector dispersion curves are then calculated using the multiband effective mass theory in section 2.4.

## 2.2 The Multiband Effective Mass Theory and Valence Band Mixing

The Bloch theorem states that the eigenfunctions of the wave equation for a periodic potential  $V(r)$  are of the form of the product of a plane wave  $e^{ik \cdot r}$  times a function  $u_{nk}(r)$  with the periodicity of the crystal. Hence, the eigenvalue equation for the energy  $E$  in band  $n$  is .

$$H_0 \Psi_{nk} = \left\{ -\frac{p^2}{2m_0} + V(r) \right\} \Psi_0 = E_n \Psi_{nk} \quad (2.1)$$

$$\Psi_{nk} = e^{ik \cdot r} u_{nk}(r) = |n, k\rangle \quad (2.2)$$

where  $u_{nk}(r)$  is the normalized Bloch function with the periodicity of  $V(r)$  and wave vector  $k$ . Assume that the Bloch function is a slow varying function of  $k$  in a *localized state* such as in quantum wells. Then the Bloch



function with arbitrary  $k$  is approximately  $u_{nk}(r) \approx u_{n0}(r)$  where  $u_{n0}(r)$  is the Bloch function at the band edge  $k=0$ . Since  $\psi_{nk}(r)$  is complete for functions having the periodicity of  $V(r)$  for any given  $k$  [Lutt 55], a *localized wave function*  $\psi_{nk}^{\text{loc}}(r)$  may be expressed in terms of the linear combination of  $\psi_{nk}(r)$  using an arbitrary set of coefficients  $A_n(k)$ .

$$\begin{aligned}\psi_{nk}^{\text{loc}}(r) &= \sum_k A_n(k) e^{ik \cdot r} u_{n,k}(r) \\ &= u_{0,k}(r) \sum_k A_n(k) e^{ik \cdot r} \\ &= u_{0,k}(r) F_n(r)\end{aligned}\tag{2.3}$$

where  $F_n(r)$  is an envelope function. The description used in Eq. (2.3) is known as the envelope function approximation. By combining Eq. (2.1) through Eq. (2.3), the matrix element of the Hamiltonian  $H$  can be derived as follows:

$$\langle n', k' | H | n, k \rangle = \left( E_n(0) + \frac{\hbar^2 k^2}{2m} \right) \delta_{nn'} \delta_{k,k'} + \frac{\hbar}{m_0} \mathbf{k} \cdot \mathbf{p}_{nn'} \delta_{k,k'}\tag{2.4}$$

$$\begin{aligned}\mathbf{p}_{nn'} &= \langle u_{n,0} | \mathbf{p} | u_{n',0} \rangle \\ &= -i \hbar \langle u_{n,0} | \nabla | u_{n',0} \rangle\end{aligned}\tag{2.5}$$

The detailed derivation of Eq. (2.4) and Eq. (2.5) is shown in the Appendix. The last term in Eq. (2.4), as well as the usually very small term in  $k^2$ , can be treated as a perturbation of the normal crystal Hamiltonian.

The Hamiltonian in matrix form can be constructed using Eq. (2.4) and Eq. (2.5). For simplicity, it is assumed that the conduction and valence

bands are decoupled, which is in fact a good approximation in a wide band gap material. The matrix is then derived in terms of  $|J, m_J\rangle$  representation, for  $J=3/2$  by considering a heavy hole and a light hole band with spin up and down in each state and shown in Table 2.1. The four by four matrix can be greatly simplified using the method first suggested by Kane [Kane 57] and later refined by Broido *et al* [Broi 85, Broi 86], Altarelli *et al* [Alta 85], and Ahn *et al* [Ahn 88]. They pointed out that a unitary transformation with a proper choice of basis set can decouple the four by four matrix into a pair of identical two by two matrix systems.

With this simplification, the Schrodinger equation for heavy and light holes is expressed as

$$\begin{bmatrix} H_h & W \\ W^\dagger & H_l \end{bmatrix} \begin{bmatrix} F_h \\ F_l \end{bmatrix} = \begin{bmatrix} E_h F_h \\ E_l F_l \end{bmatrix} \quad (2.6)$$

where  $H_h$ ,  $H_l$  are the Hamiltonian of the heavy and light holes,  $W$  and  $W^\dagger$  are the coupling terms and  $F_h$  and  $F_l$  are the envelope functions of the heavy and the light holes. Assuming the plane wave solutions,  $H_h$  and  $H_l$  can be written as

$$\begin{aligned} H_h &= (\gamma_1 - 2\gamma_2)k_z^2 + (\gamma_1 + \gamma_2)k_t^2 + V_h \\ H_l &= (\gamma_1 + 2\gamma_2)k_z^2 + (\gamma_1 - \gamma_2)k_t^2 + V_l \end{aligned} \quad (2.7)$$

where  $\gamma_i$ 's are the Luttinger parameters and  $V_h$ ,  $V_l$  are the potential well depth of the heavy and light holes. In the above equation,  $k_z$  and  $k_t$  are the  $k$

Table 2.1  
The Luttinger-Kohn Matrix for Heavy and Light Hole Bands

	$ \frac{3}{2}, \frac{3}{2}\rangle$	$ \frac{3}{2}, -\frac{1}{2}\rangle$	$ \frac{3}{2}, \frac{1}{2}\rangle$	$ \frac{3}{2}, -\frac{3}{2}\rangle$
$ \frac{3}{2}, \frac{3}{2}\rangle$	P+Q	R	-S	0
$ \frac{3}{2}, -\frac{1}{2}\rangle$	R*	P-Q	0	S
$ \frac{3}{2}, \frac{1}{2}\rangle$	-S*	0	P-Q	R
$ \frac{3}{2}, -\frac{3}{2}\rangle$	0	S*	R*	P+Q

$$P = \frac{1}{2} \left( \frac{\hbar^2}{m_0} \right) \gamma_1 (k_x^2 + k_y^2 + k_z^2)$$

$$Q = \frac{1}{2} \left( \frac{\hbar^2}{m_0} \right) \gamma_2 (k_x^2 + k_y^2 + k_z^2)$$

$$S = \sqrt{3} \left( \frac{\hbar^2}{m_0} \right) \gamma_3 k_z (k_x - ik_y)$$

$$R = - \left( \frac{\hbar^2}{m_0} \right) \left[ \frac{\sqrt{3}}{4} (\gamma_2 + \gamma_3) (k_x - ik_y)^2 - \frac{\sqrt{3}}{4} (\gamma_3 - \gamma_2) (k_x + ik_y)^2 \right]$$

vector components with  $k_z$  directed along the epi growth direction and  $k_t$  directed along the epi layer. The coupling terms  $W$  and  $W^+$  for the {100} plane are defined as [Zory 93]

$$\begin{aligned} W &= \sqrt{3}k_t(\gamma_2k_t - i2\gamma_3k_z) \\ W^\dagger &= \sqrt{3}k_t(\gamma_2k_t + i2\gamma_3k_z) \end{aligned} \quad (2.8)$$

For  $k_t=0$ , the coupling term vanishes so we can solve the coupled Schrodinger like equations for the valence band separately, but for finite  $k_t$ , we need to solve them simultaneously. It is noted that from Eq. (2.7), the Luttinger parameter and the effective masses can be related for  $k_t=0$  as follows [Zory 93]:

$$\begin{aligned} \frac{1}{\gamma_1 - 2\gamma_2} &\equiv \frac{\hbar^2}{2m_{hh}} \\ \frac{1}{\gamma_1 + 2\gamma_2} &\equiv \frac{\hbar^2}{2m_{lh}} \end{aligned} \quad (2.9)$$

### 2.3 Carrier Potential Well

In order to calculate the energy dispersion of given QW structures, it is essential to know the carrier potential well structure, or potential well depth. In this section, the quantum well structures of  $\text{Ga}_x\text{In}_{1-x}\text{P}/(\text{Al}_{0.6}\text{Ga}_{0.4})_{0.5}\text{In}_{0.5}\text{P}$  and  $\text{Cd}_{0.2}\text{Zn}_{0.8}\text{Se}/\text{ZnS}_{0.06}\text{Se}$  are estimated. In general, determining the band lineups in a heterostructure is a very complicated problem. So it is hard to predict the band offsets with great accuracy even with the best theory known.



In other words, the exact band offset can be determined only using experimental techniques such as magneto-optical spectroscopy. However, unfortunately, the experimental data for the band offsets of these material systems are not known yet. In this section, two methods for estimating the carrier confinement will be introduced: the *electron affinity rule* which is the simplest model and the *model solid theory* by Van de Walle and Martin [VAN 86] which is nowadays widely accepted and supported by experiment.

### 2.3.1 The Model Solid Theory

Recently, Van de Walle *et al* [Van 88] have reported a series of calculations for a number of heterojunction interfaces. In that work, the large number of interfaces is treated in a uniform way. In the model solid theory, the common reference energy level is accomplished by modeling the solid as a superposition of neutral atoms. In each atom, the electrostatic potential is rigorously defined with respect to the vacuum level. Therefore, the average electrostatic potential ( $E_{av}$ ) is specified on the absolute energy scale by superposition. The relative positions of valence band ( $E_v$ ) and conduction band ( $E_c$ ) edge with respect to the average potential are simply given by

$$\begin{aligned} E_v &= E_{v, av} + \frac{\Delta_0}{3} \\ E_c &= E_v + E_g \end{aligned} \tag{2.10}$$

where  $\Delta_0$  is the spin-orbit splitting and  $E_g$  is the energy band gap. The average potential itself contains no information. But when two different



semiconductors consist of a heterojunction, we can define the band offset by comparing the average potential (and hence,  $E_c$ 's and  $E_v$ 's) of each material. The band offset parameters of  $\text{Ga}_x\text{In}_{1-x}\text{P}/(\text{Al}_{0.6}\text{Ga}_{0.4})_{0.5}\text{In}_{0.5}\text{P}$  for  $x=0.3, 0.4, 0.5$ , and  $0.6$  are summarized in Table 2.2.

### 2.3.2 The Electron Affinity Rule

Although the model solid theory is regarded as significantly more accurate than the earlier ones for heterostructure band lineups, the average electrostatic potential ( $E_{av}$ ) of CdSe (which is needed for interpolation for  $\text{Cd}_{0.2}\text{Zn}_{0.8}\text{Se}$ ) is not known yet because of the lack of material parameters for cubic CdSe (most hexagonal CdSe parameters are known). Hence, the simple electron affinity rule was used for the CdZnSe system.

To define the band lineups of the  $\text{Cd}_{0.2}\text{Zn}_{0.8}\text{Se}/\text{ZnS}_{0.6}\text{Se}_{0.94}$  heterojunction, the conduction and valence band offset in the absence of strain was estimated using the electron affinity rule. The vacuum level was used for a reference and the relative positions of the conduction band edges of  $\text{Cd}_{0.2}\text{Zn}_{0.8}\text{Se}$  and  $\text{ZnS}_{0.6}\text{Se}_{0.94}$  were determined from the electron affinity of each material, that is, the energy to remove an electron from the conduction minimum to the vacuum level. Then the valence band offset was derived by subtracting the energy band gap from the conduction band edge of each material. The electron affinity is  $4.079\text{eV}$  for  $\text{ZnS}_{0.6}\text{Se}_{0.94}$  and  $4.262\text{eV}$  for  $\text{Cd}_{0.2}\text{Zn}_{0.8}\text{Se}$  as interpolated from the host materials (ZnS, ZnSe and CdSe).

Table 2.2  
Ga<sub>x</sub>In<sub>1-x</sub>P Parameters

<b>Ga<sub>x</sub>In<sub>1-x</sub>P</b>	<b>E<sub>v,av</sub></b>	<b>Δ<sub>o</sub></b>	<b>E<sub>g</sub></b>	<b>E<sub>v</sub></b>	<b>E<sub>c</sub></b>
x=0 (InP)	-7.04	0.11	1.349	-7.003	-5.654
x=0.3	-7.15	0.10	1.624	-7.117	-5.493
x=0.4	-7.19	0.10	1.746	-7.157	-5.411
x=0.5	-7.23	0.10	1.883	-7.197	-5.314
x=0.6	-7.26	0.108	2.035	-7.224	-5.189
x=1 (GaP)	-7.40	0.08	2.797	-7.373	-4.576
(Al <sub>0.6</sub> Ga <sub>0.4</sub> ) <sub>0.5</sub> In <sub>0.5</sub> P	-7.44	0.13	2.31	-7.397	-5.087

The problem of this approach is that the electron affinity is not necessarily the property of the heterojunction interface [Capa 87]. Another problem with the electron affinity rule is that there may be charge transfer at the interface, which would alter the band lineup. So it should be noted that our results will be just a rough approximation.

### 2.3.3 The Strain Effect

When the lattice constant of QW material is different from the barrier material, the QW layer is subject to either compressive or tensile strain as illustrated in Fig. 2.3. The strain reduces the crystal symmetry and results in the energy shifts of the conduction and valence band. As a consequence, the energy vs. in-plane  $k$  vector dispersion varies and hence the in-plane effective masses are changed. The energy shifts due to the hydrostatic strain are expressed as [Poll 68, Gavi 70, Chan 77]

$$\begin{aligned} \Delta E_c(\text{hydrostatic}) &= a_c \frac{\Delta\Omega}{\Omega} && \text{for conduction band} \\ \Delta E_v(\text{hydrostatic}) &= a_v \frac{\Delta\Omega}{\Omega} && \text{for valence band} \end{aligned} \quad (2.11)$$

where  $a_c(a_v)$  are hydrostatic deformation potential for the conduction (valence) band, and  $\frac{\Delta\Omega}{\Omega}$  is the fractional volume change. For (001) substrates,  $\Delta\Omega/\Omega = \epsilon_{xx} + \epsilon_{yy} + \epsilon_{zz}$  where  $\epsilon_{ij}$  are the components of the strain tensor defined as  $\epsilon_{xx} = \epsilon_{yy} = (a_{cb}/a_{qw}) - 1$  for the direction parallel to the surface, where  $a_b$  ( $a_{qw}$ ) is the lattice constant of the cladding (quantum well) layer and  $\epsilon_{zz} = -\frac{2C_{12}}{C_{11}}\epsilon_{xx}$  for the direction perpendicular to the surface



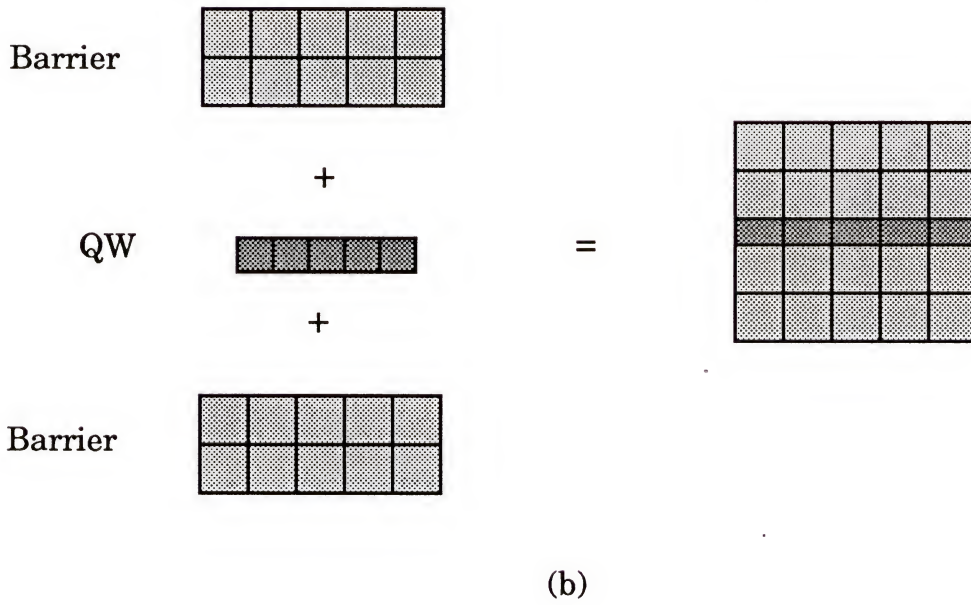
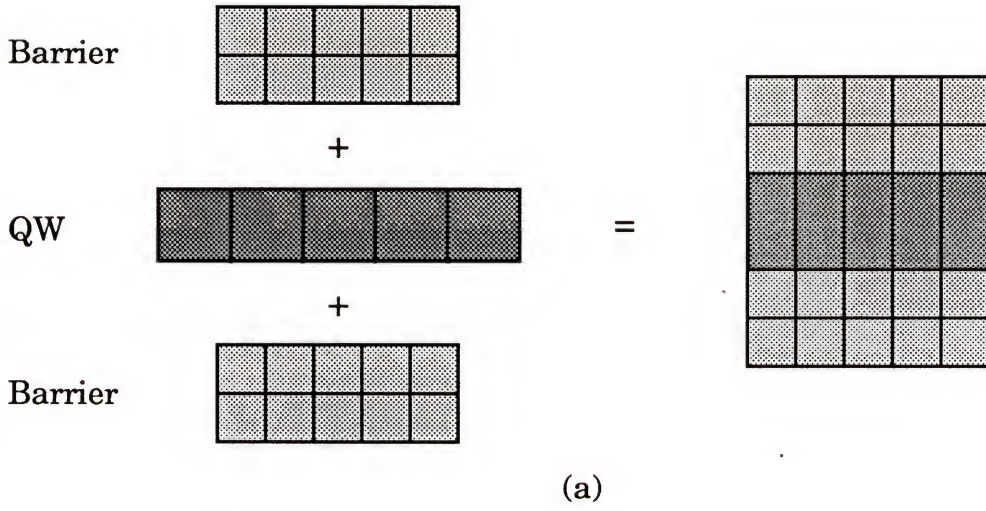


Figure 2.3 Schematics of strain effect for (a) compressive and (b) tensile strain.



where  $C_{ij}$  are the elastic moduli. The shear strain splits the degeneracy of the valence band at  $\Gamma$  peak. For the strain along the (001) plane, the energy shifts of heavy and light hole states are expressed as [Poll 68, Gavi 70, Chan 77]

$$\begin{aligned}\Delta E_h(\text{shear}) &= \frac{1}{2} \delta E_{001} \\ \Delta E_l(\text{shear}) &= -\frac{1}{2} \delta E_{001} - \frac{1}{2} \cdot \frac{(\delta E_{001})^2}{\Delta_o}\end{aligned}\tag{2.12}$$

with  $\delta E_{001} = 2b(\epsilon_{zz} - \epsilon_{xx})$  where  $b$  is the shear deformation potential. The parameters for band lineups are summarized in Table 2.3.

#### 2.3.4 The Potential Well Structure of GaInP and CdZnSe QW Lasers

Based on the methods discussed in the previous sections, the potential well structures of  $\text{Ga}_x\text{In}_{1-x}\text{P}/(\text{Al}_{0.6}\text{Ga}_{0.4})_{0.5}\text{In}_{0.5}\text{P}$  and  $\text{Cd}_{0.2}\text{Zn}_{0.8}\text{Se}/\text{ZnS}_{0.06}\text{Se}$  quantum well, shown in Fig. 2.4 and Fig. 2.5, are calculated in two steps; First, the band offset is estimated in the absence of the strain effect with the model solid theory for  $\text{Ga}_x\text{In}_{1-x}\text{P}/(\text{Al}_{0.6}\text{Ga}_{0.4})_{0.5}\text{In}_{0.5}\text{P}$  quantum wells and with electron affinity for  $\text{Cd}_{0.2}\text{Zn}_{0.8}\text{Se}/\text{ZnS}_{0.06}\text{Se}$  quantum wells. Then the strain effect is taken into account for each quantum well and finally the carrier confinements are derived. The results are shown in Fig. 2.6, Fig. 2.7, and Fig. 2.8 schematically for  $\text{Ga}_x\text{In}_{1-x}\text{P}/(\text{Al}_{0.6}\text{Ga}_{0.4})_{0.5}\text{In}_{0.5}\text{P}$  for  $x=0.3$ (compressive strain) and  $x=0.6$  (tensile strain) and  $\text{Cd}_{0.2}\text{Zn}_{0.8}\text{Se}/\text{ZnS}_{0.06}\text{Se}$  quantum well lasers.

For  $\text{Ga}_x\text{In}_{1-x}\text{P}/(\text{Al}_{0.6}\text{Ga}_{0.4})_{0.5}\text{In}_{0.5}\text{P}$  quantum wells, an important

Table 2.3  
Ga<sub>x</sub>In<sub>1-x</sub>P Material Parameters

	<b>InP</b> x=0	x=0.3	x=0.4	x=0.5	x=0.6	<b>GaP</b> x=1
a <sub>0</sub>	5.8686	5.7434	5.7016	5.6599	5.6182	5.4512
C <sub>11</sub>	10.22	11.46	11.86	12.25	12.66	14.12
C <sub>12</sub>	5.76	5.92	5.97	6.02	6.07	6.25
a <sub>v</sub>	1.27	1.41	1.45	1.49	1.53	1.70
a <sub>c</sub>	-5.04	-5.72	-5.92	-6.12	-6.33	-7.14
a	-6.31	-7.12	-7.37	-7.62	-7.87	-8.84
b	-2.0	-1.94	-1.92	-1.90	-1.88	-1.80
m <sub>hh</sub>	0.45	0.464	0.462	0.460	0.458	0.47
m <sub>lh</sub>	0.12	0.135	0.14	0.145	0.15	0.17

GaAs	1000Å	$p=2 \times 10^{19} \text{cm}^{-3}$	
$\text{Al}_{0.5}\text{In}_{0.5}\text{P}$	1000Å	$p=4 \times 10^{18} \text{cm}^{-3}$	
$\text{Al}_{0.5}\text{In}_{0.5}\text{P}$	0.9μm	$p=6 \times 10^{17} \text{cm}^{-3}$	
$(\text{Al}_{0.6}\text{Ga}_{0.4})_{0.5}\text{In}_{0.5}\text{P}$	1400Å	undoped	
			← $\text{Ga}_x\text{In}_{1-x}\text{P}$ 80Å QW
$(\text{Al}_{0.6}\text{Ga}_{0.4})_{0.5}\text{In}_{0.5}\text{P}$	1400Å	undoped	
$\text{Al}_{0.5}\text{In}_{0.5}\text{P}$	0.9μm	$p=5 \times 10^{18} \text{cm}^{-3}$	
$\text{Ga}_{0.5}\text{In}_{0.5}\text{P}$	$n=5 \times 10^{18} \text{cm}^{-3}$		
GaAs Buffer			
GaAs: Si	Substrate 10 degree tilt (100) toward (011)		

Figure 2.4 The epitaxial layer structure of  $\text{Ga}_x\text{In}_{1-x}\text{P}$  QW lasers.

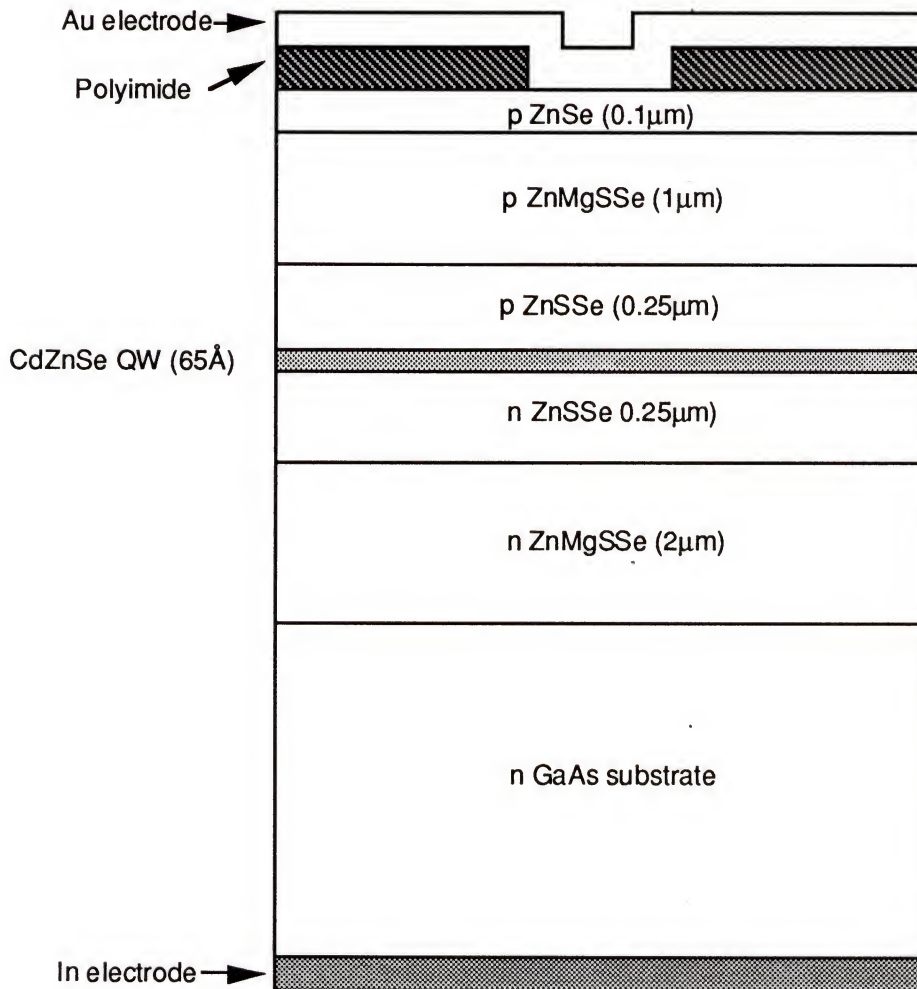


Figure 2.5 The epitaxial layer structure of CdZnSe QW lasers.



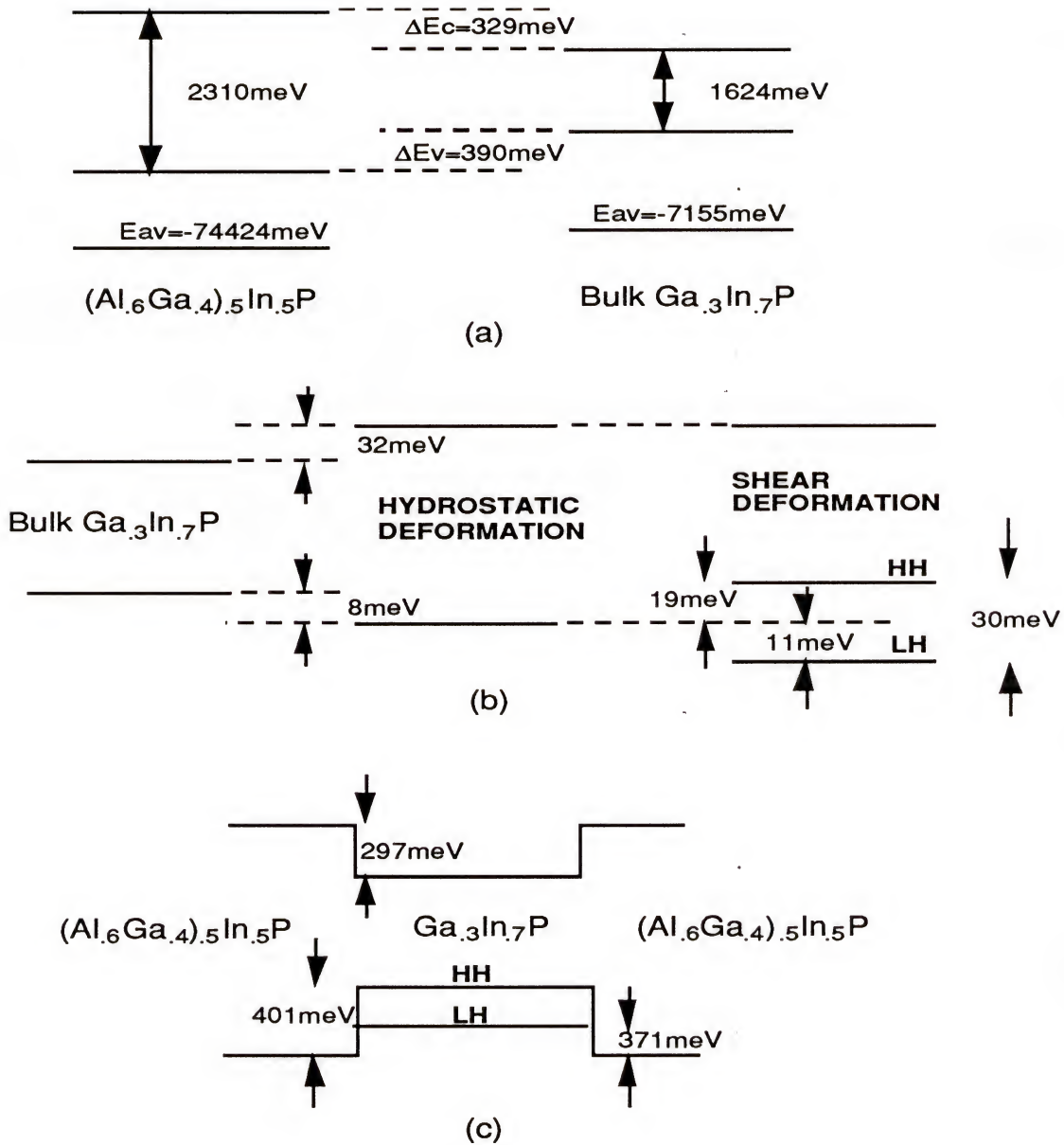


Figure 2.6 Band line-ups of  $Ga_{0.3}In_{0.7}P/(Al_{0.6}Ga_{0.4})_{0.5}In_{0.5}P$  QW structure; (a) bulk (b) strain effect (c) carrier confinement with strain.

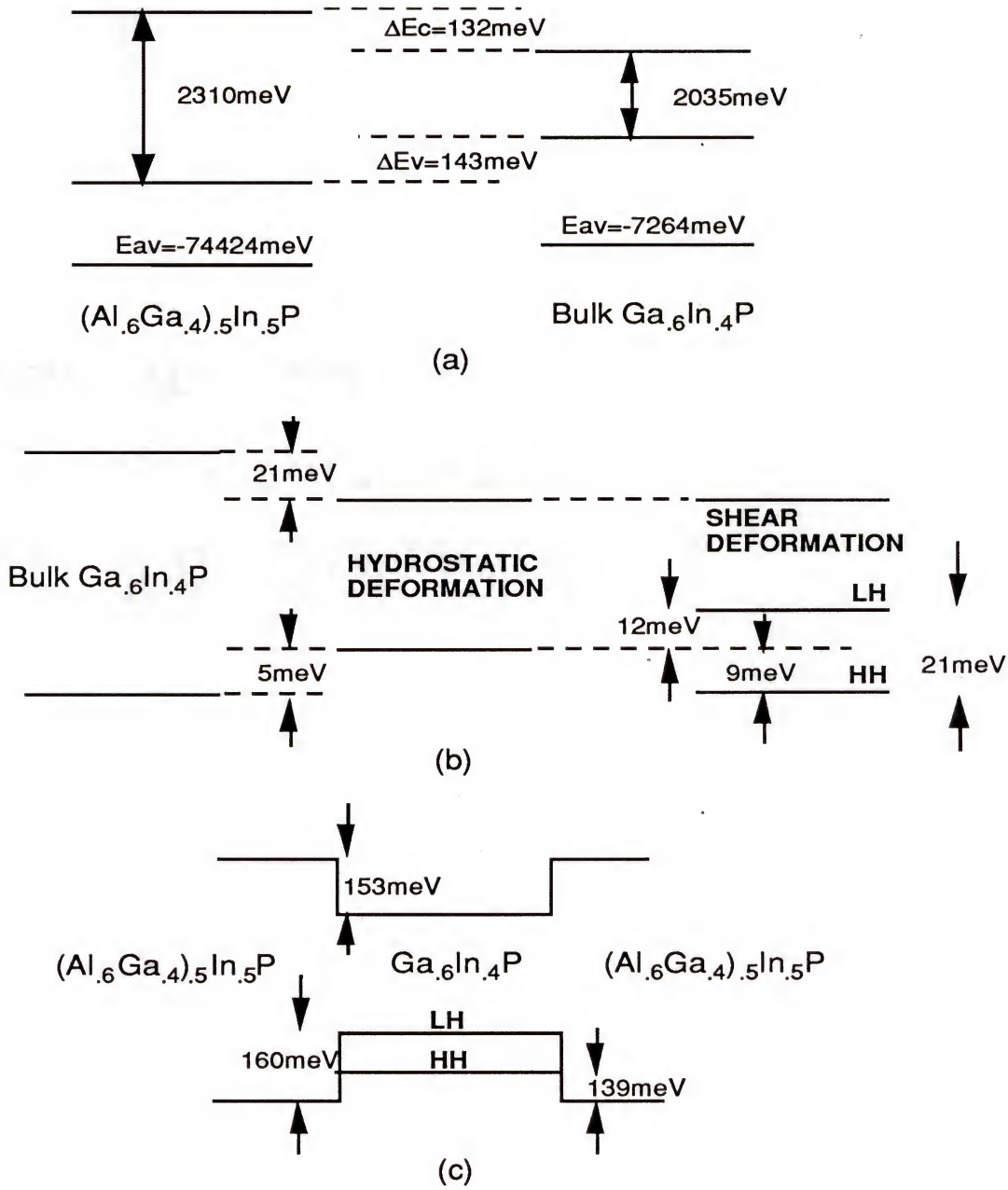


Figure 2.7 Band line-ups of  $Ga_{0.6}In_{0.4}P/(Al_{0.6}Ga_{0.4})_{0.5}In_{0.5}P$  QW structure; (a) bulk (b) strain effect (c) carrier confinement with strain.

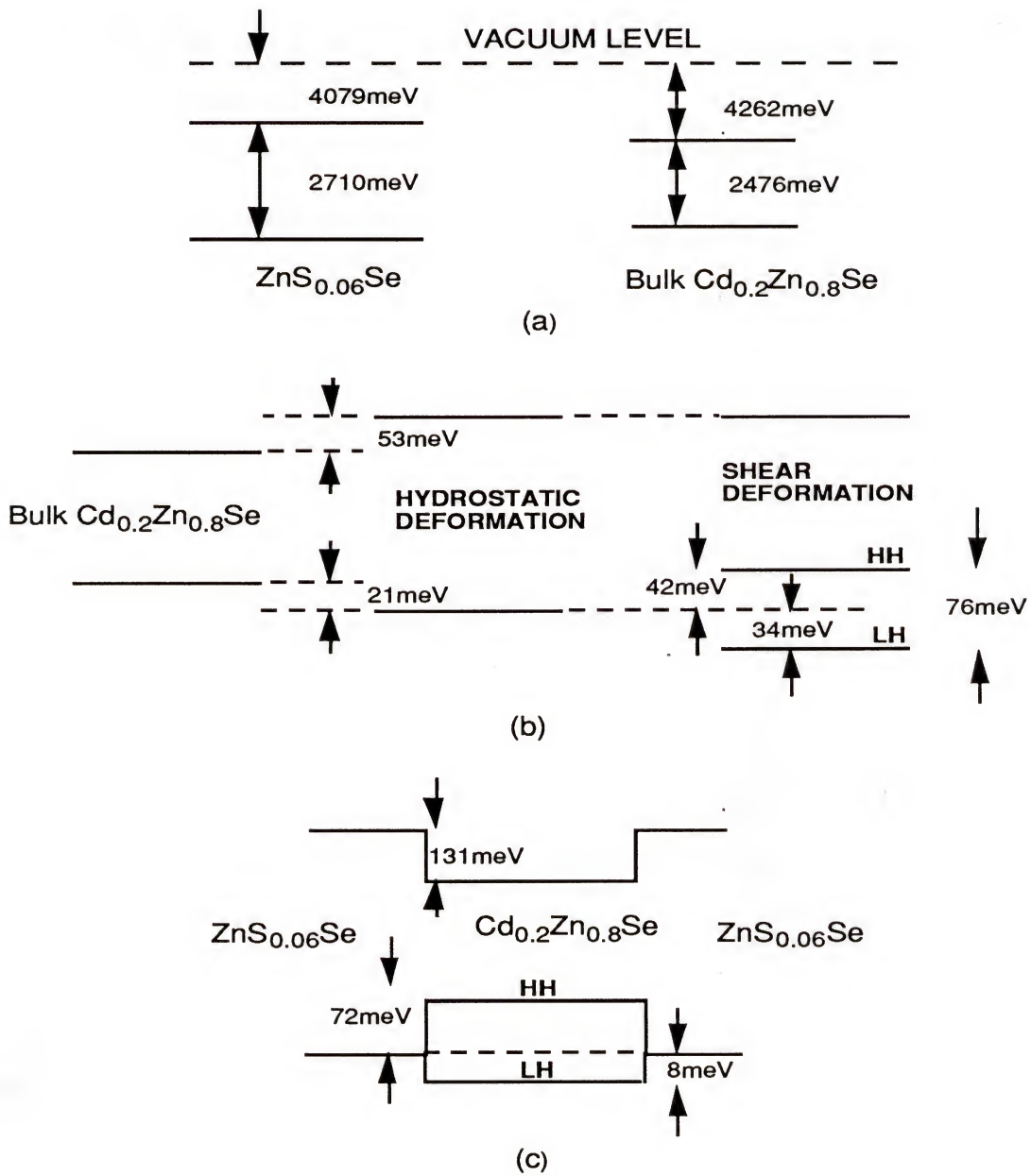


Figure 2.8 Band line-ups of  $\text{Cd}_{0.2}\text{Zn}_{0.8}\text{Se}/\text{ZnS}_{0.06}\text{Se}$  QW structure; (a) bulk (b) strain effect (c) carrier confinement with strain.

feature can be seen. The heavy hole is the ground state for compressive strain ( $x=0.3$ ) while the light hole is the ground state for tensile strain ( $x=0.6$ ). These differences lead to polarization anisotropy and will be discussed in detail in chapter III. For CdZnSe quantum wells, the potential well depth of the heavy hole state is 72meV, but the light hole state is almost lined up with the barrier layer. So it is expected that most transitions occur between conduction electrons and relatively well confined heavy hole states.

## 2.4 Energy Dispersion

Based on the band diagram under strain effect derived in the previous section, we now derive the energy vs. in-plane  $k$  vector dispersion. We assume that the conduction band is parabolic and take the band mixing effect into account for the valence band. The multiband effective mass theory was used to calculate the band structure and electron (hole) wave functions of a quantum well.

For the conduction band, the subband structure of a quantum well is obtained by solving the Schrodinger-like equation using the envelope function approximation.

$$H_c F_c = E_c F_c \quad (2.13)$$

where  $H_c$  is the hamiltonian for the conduction band simply given by

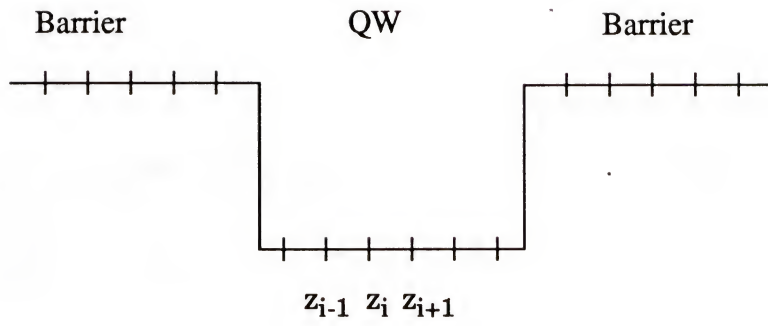
$$H_c = \frac{\hbar^2}{2m} \cdot \frac{d^2}{dz^2} + V_c \quad (2.14)$$

where  $F_c$  is the envelope function of the conduction band,  $m_c$  is the



conduction band effective mass, and  $V_c$  is the potential well depth for the conduction band electron. The assumption that the interaction between energy subbands is weak makes the calculation of the conduction band electron structure simple. Since this does not hold in the valence band, the  $k \cdot p$  method was used for the valence band and band mixing was taken into account.

The finite difference method (FDM) was used for the numerical calculation of the energy dispersion. This method is particularly well suited to simple device geometries and has been used extensively to model one and two dimensional rectangular geometry (planar) devices such as quantum well lasers. The FDM produces solutions for the physical variables as discretized values at specific nodes contained within a mesh superimposed on the solution domain. The finite difference equations are derived from truncated Taylor series for continuous function  $f(x+\Delta x)$  and  $f(x-\Delta x)$  [Lim 92]. For simplicity, the uniform meshes were used in the calculation. The quantum well region was divided into 20 to 40 regions, depending on the thickness, and about 200 mesh points in the barrier layer were included for a better convergence. Then the Schrodinger equations Eq. (2.6) and Eq. (2.13) were discretized at each node as schematically illustrated in Fig. 2.9. The energy dispersion for  $\text{Ga}_x\text{In}_{1-x}\text{P}/(\text{Al}_{0.6}\text{Ga}_{0.4})_{0.5}\text{In}_{0.5}\text{P}$  and  $\text{Cd}_{0.2}\text{Zn}_{0.8}\text{Se}/\text{ZnS}_{0.6}$  QW lasers are shown in Fig. 2.10, Fig. 2.11, and Fig. 2.12.



$$\frac{df}{dz_i} = \frac{f(z_{i+1}) - f(z_{i-1}))}{2\Delta z}$$

$$\frac{d^2f}{dz^2} = \frac{f(z_{i+1}) + f(z_{i-1})) - 2f(z_i)}{(\Delta z)^2}$$

Figure 2.9 Mesh points and discretized function of a QW structure

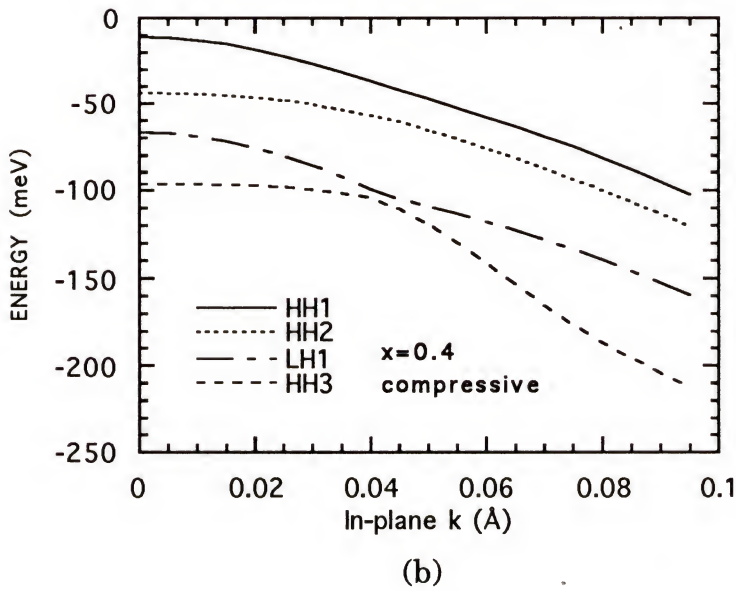
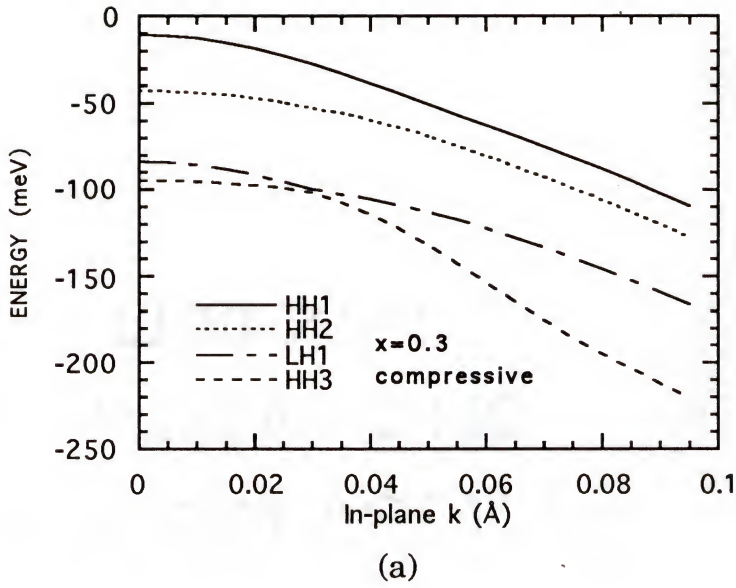


Figure 2.10 The energy vs. in-plane  $k$  vector dispersion of  $\text{Ga}_x\text{In}_{1-x}\text{P}/(\text{Al}_{0.6}\text{Ga}_{0.4})_{0.5}\text{In}_{0.5}\text{P}$ . (a)  $x=0.3$  and (b)  $x=0.4$ .

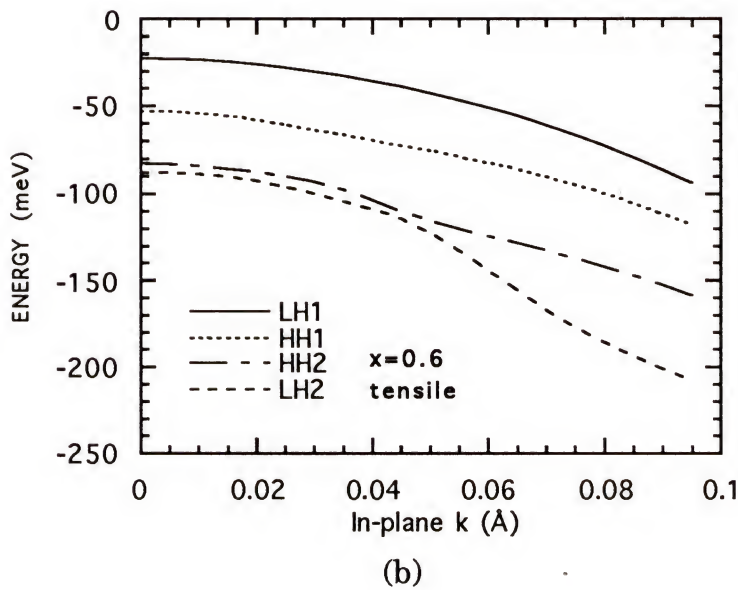
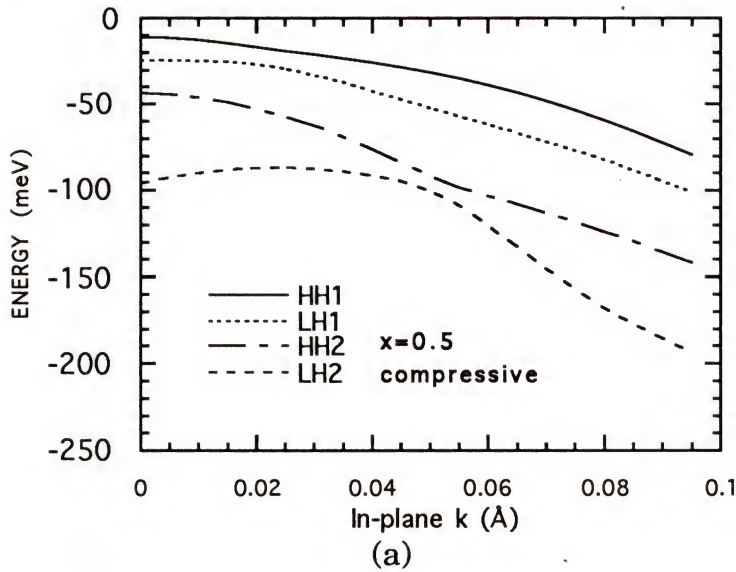


Figure 2.11 The energy vs. in-plane  $k$  vector dispersion of  $\text{Ga}_x\text{In}_{1-x}\text{P}/(\text{Al}_{0.6}\text{Ga}_{0.4})_{0.5}\text{In}_{0.5}\text{P}$ . (a)  $x=0.5$  and (b)  $x=0.6$ .



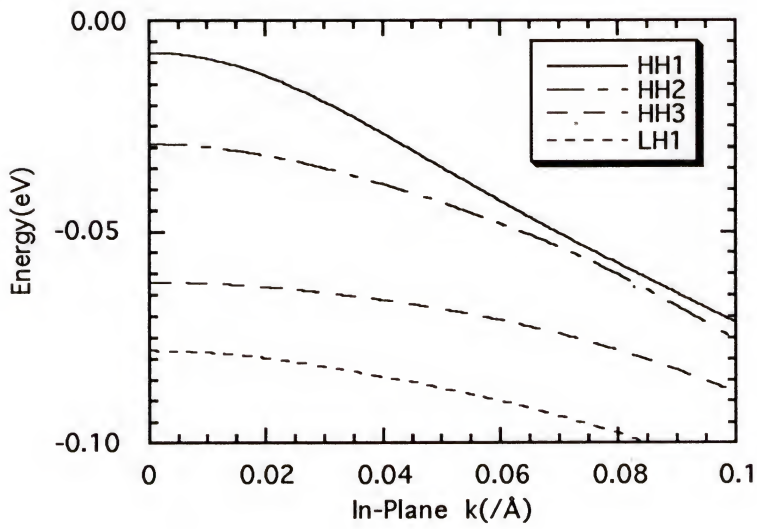


Figure 2.12 The energy vs. in-plane  $k$  vector dispersion of  $\text{Cd}_{0.2}\text{Zn}_{0.8}\text{Se}/\text{ZnS}_{0.6}$  QW lasers.

## 2.5 Summary

The energy vs. in-plane  $k$  vector dispersions of GaInP and CdZnSe quantum wells were derived. For the conduction band, the parabolic approximation was used neglecting the interaction between the energy subbands. For the valence band, the multiband effective mass theory was used and the band mixing effect was taken into account. In order to define the carrier potential well structures, the electron affinity rule and the model solid theory were used. The strain on the QW layer perturbed the crystal symmetry and resulted in energy shifts of the conduction and valence bands. The strain is either compressive or tensile and the energy gap is increased for a compressive strain and reduced for a tensile strain by a hydrostatic deformation. The shear strain splits degeneracy of the valence band at the band edge. With the strain effect taken into account, it was shown that the valence band ground state of  $\text{Ga}_x\text{In}_{1-x}\text{P}/(\text{Al}_{0.6}\text{Ga}_{0.4})_{0.5}\text{In}_{0.5}\text{P}$  QW lasers can be either a heavy hole state or light hole state depending on the GaP alloy content. For CdZnSe QW lasers whose active layer is compressively strained, the light hole state was almost lined up with the barrier layer while the heavy hole state was well confined. The energy dispersion curves for GaInP and CdZnSe QW lasers were numerically calculated using the finite difference method.

## CHAPTER III POLARIZATION ANISOTROPY OF RED LASERS

### 3.1 Introduction

Red diode lasers with peak wavelength around 680 nm are of interest for numerous application areas. Important uses include laser pointers, solid state laser pumping, medicine, printing, bar code scanning, and optical data storage. It is known that such lasers are most successfully made with GaInP quantum well lasers with AlGaInP barrier layer. However, depends on the GaP alloy content in the active layer, the quantum well is subject to the strain.

Shear strain perturbs the valence band structure of quantum wells, and are important in determining the threshold current density, wavelength, and polarization state of quantum well diode laser. In fact, quantum well lasers most often oscillate in the transverse electric (TE) polarization, because the heavy hole (hh) band is the ground state for both lattice matched and compressive strained quantum wells [Chin 88, Zory 93]. Therefore, the hh population is most easily inverted, and the polarization anisotropy of the hh transition's gain favors the TE mode. Conversely, transverse magnetic (TM) mode oscillation prevails in some tensile strained quantum well lasers, where the light hole (lh) band becomes the ground state through a strain induced



reversal of the lh and hh band edges [Welc 91, Boer 90, Thij 91]. In this chapter, the polarization dependent effects and the in-plane spontaneous emission of 80Å  $\text{Ga}_x\text{In}_{1-x}\text{P}/(\text{Al}_{0.6}\text{Ga}_{0.4})_{0.5}\text{In}_{0.5}\text{P}$  quantum well lasers with  $x=0.3$  and  $0.4$  (compressive strain),  $x=0.5$  (lattice matched), and  $x=0.6$  (tensile strain) are investigated theoretically and experimentally. In the section 3.2, the relative transition strength is derived and the polarization anisotropy is discussed in the section 3.3. The experimental results are given in the section 3.4. and discussion is given in section 3.5.

### 3.2 Transition Matrix Element

For quantum well lasers, the carrier transition occurs mostly near the band edge where the in-plane  $k$  vector is negligible. Hence by estimating the transition matrix element near the band edge, the polarization anisotropy can be estimated qualitatively as well as quantitatively. The transition matrix element, or the transition strength which will be discussed later in this section, can be established by defining the Bloch functions in each band. In fact, each energy band can be viewed as originating from the discrete atomic energy levels of the isolated atoms that composed the crystal [Kane 57]. In this sense, the conduction band can be thought as a remnant of an  $s$  orbital, while the three valence bands are the remnants of the three  $p$  atomic orbitals:  $p_x$ ,  $p_y$ , and  $p_z$ . The corresponding Bloch functions for these orbitals are denoted as  $u_s$  ( $s$  orbital), and  $u_x$ ,  $u_y$ , and  $u_z$ , or  $u_i$  ( $p$  orbital) where  $i$



denotes either x, y, or z. The conduction band Bloch function  $u_s$  has even symmetry in all three directions while  $u_i$  has odd symmetry along  $i$  direction but even symmetry in the other two directions so  $\langle u_s | u_i \rangle = 0$ . However,  $\langle u_s | p_i | u_i \rangle$  is in general non zero because  $p = (\hbar/i) (d/dx)$  and hence, operating on  $u_i$  with  $p_i$  inverts the symmetry. From these arguments, some symmetry relations can be written as follows [Zory 93]:

$$\begin{aligned} \langle u_s | p_i | u_i \rangle &= 0 & \text{for } i \neq j \\ \langle u_s | \mathbf{p} | u_i \rangle &= \langle u_s | p_i | u_i \rangle = M \\ \langle u_s | \mathbf{p} | \bar{u}_i \rangle &= 0 \end{aligned} \quad (3.1)$$

where  $u_i$ , and  $\bar{u}_i$  indicate spin-up and spin-down functions. The constant  $M$  is defined here as the basis function momentum matrix element.

The valence band Bloch functions  $u_{hh}$  (heavy hole),  $u_{lh}$  (light hole), and  $u_{so}$  (spin-orbit) can be expressed in terms of the linear combination of the basis functions  $u_x$ ,  $u_y$ , and  $u_z$  [Kane 57, Lutt 55, Zory 93]. Defining the electron's  $k$  vector to be directed along  $z$ , the normalized valence band Bloch functions can be written as [Zory 93]

$$\begin{aligned} u_{hh} &= -\frac{1}{\sqrt{2}} (u_x + i u_y) & u_{hh} &= \frac{1}{\sqrt{2}} (\bar{u}_x - i \bar{u}_y) \\ u_{lh} &= -\frac{1}{\sqrt{6}} (\bar{u}_x + i \bar{u}_y - 2 u_z) & u_{lh} &= \frac{1}{\sqrt{6}} (u_x - i u_y + 2 \bar{u}_z) \\ u_{so} &= -\frac{1}{\sqrt{3}} (\bar{u}_x + i \bar{u}_y + u_z) & u_{so} &= -\frac{1}{\sqrt{3}} (u_x - i u_y - \bar{u}_z) \end{aligned} \quad (3.2)$$

Using the above expressions, the matrix element which determines the transition probability between  $u_s$  and the basis functions ( $u_i$ ) can be derived.

The conduction band effective mass along the electron's  $k$  vector (assume  $z$  direction) is expressed as [Kane 57, Made 78]

$$\frac{1}{m_c} = \frac{1}{m_0} \left[ 1 + \sum_{n \neq c} \frac{2}{m_0} \cdot \frac{|\langle u_c | p_z | u_n \rangle|^2}{E_c - E_n} \right] \quad (3.3)$$

where the summation sums over all  $n$  energy bands, and the  $E_n$  and  $E_c$  are the band edge energies of each bands. By neglecting all but the three valence bands in the summation, an approximate expression for the conduction band effective mass is obtained using the relation given in Eq. (3.1) and Eq. (3.2). From Eq. (3.2), it is noted that the heavy hole Bloch function does not contain  $u_z$ , and hence the contribution to the sum is zero. Thus, summing over the light hole and spin-orbit band energy separations in Eq. (3.3) yields

$$\frac{1}{m^*} = \frac{1}{m_0} \left[ 1 + \frac{2|M|^2}{m_0} \left( \frac{2}{3} \cdot \frac{1}{E_g} + \frac{1}{3} \cdot \frac{1}{(E_g + \Delta)} \right) \right] \quad (3.4)$$

Since the higher energy bands are neglected in this approximation, the effective mass  $m^*$  is expected to be smaller than the true one as illustrated in Fig.3.1. The true conduction band effective mass can be measured experimentally to a good degree of precision using cyclotron resonance technique. By assuming that  $m^*$  is close to the true effective mass  $m_c$ , Eq. (3.4) can be rearranged to obtain

$$|M|^2 = \left( \frac{m_0}{m^*} - 1 \right) \frac{(E_g + \Delta)}{2 \left( E_g + \frac{2}{3} \Delta \right)} m_0 E_g \quad (3.5)$$

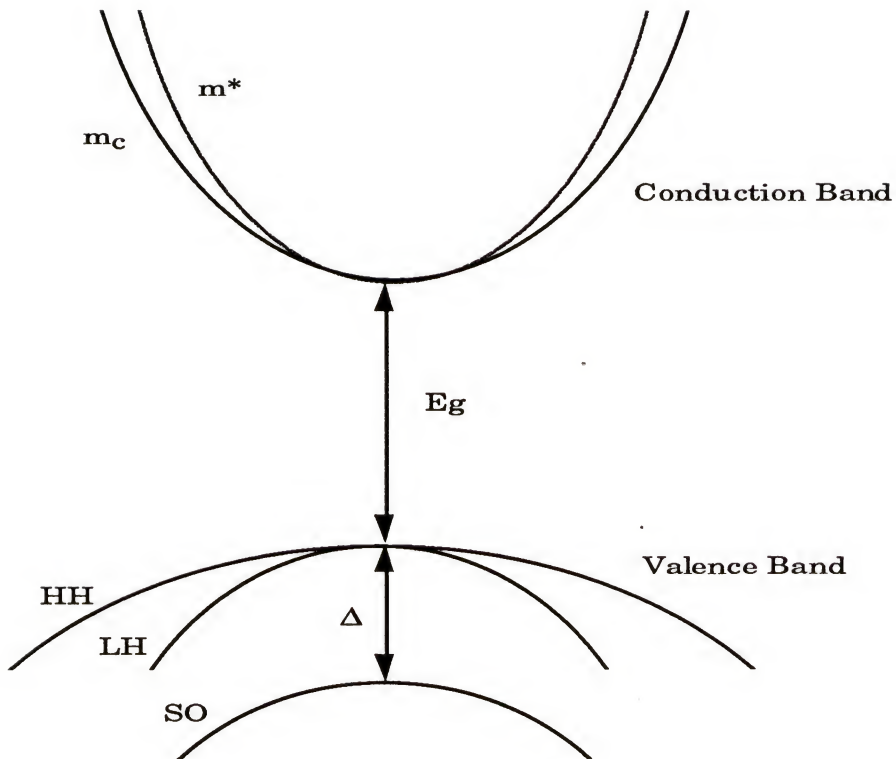


Figure 3.1 Typical III-V semiconductor band structure schematic. The dashed line of conduction band shows the approximated effective mass.

Although this approximation provides comprehensive relationship between the matrix element and the energy gaps, it should be noted that the assumption,  $m^*$  is close to  $m_c$ , may not be valid when the contribution from the higher energy bands in Eq. (3.3) is significant. For instance, in GaAs,  $m^* = 0.057m_0$ , compared with the true effective mass  $0.067m_0$ . However, it is a useful formula for a material that has not been fully characterized. The most accurate estimate of the transition matrix element can be obtained by electron spin resonance techniques.

Having obtained the magnitude of  $|M|^2$ , the transition matrix element  $|M_T|^2$  which determines the transition probability between conduction band and valence band Bloch functions can be quantified. The transition matrix element  $|M_T|^2$  is defined by [Zory 93]

$$|M_T|^2 = |\langle u_v | \hat{e} \cdot \mathbf{p} | u_c \rangle|^2 |\langle F_h | F_e \rangle|^2 \quad (3.6)$$

where  $\hat{e}$  is the unit polarization vector,  $\mathbf{p}$  is the momentum operator, and  $F_h(F_e)$  is the envelope function of the valence (conduction) band. As shown in Fig. 3.2, there are four possible transitions between the spin-degenerated conduction and valence bands. Summing over these transitions, Eq. (3.6) becomes

$$|M_T|_V^2 = \sum_{u_c} \sum_{u_c, u_v, u_v} |\langle u_v | (\hat{e} \cdot \mathbf{p}) | u_c \rangle|^2 \quad (3.7)$$

The envelope function overlap integral  $|\langle F_h | F_l \rangle|^2$  is assumed equal to unity, because for the momentum transitions between two bulk plane wave



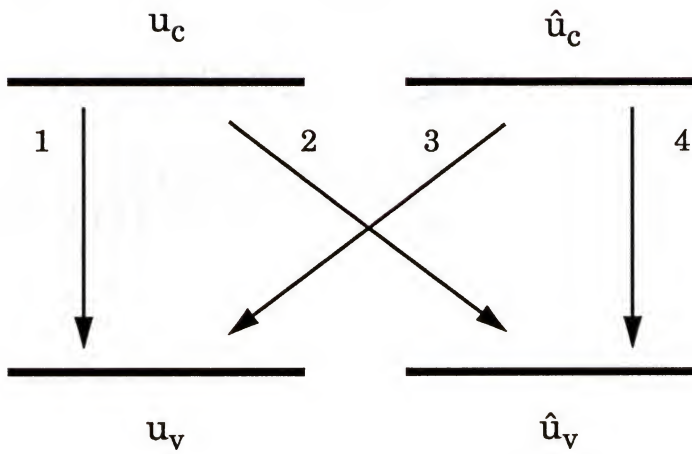


Figure 3.2 Diagram illustrating the four possible transitions between the spin-degeneracy conduction and valence band.  $u_c$  ( $u_v$ ) is the spin-up conduction (valence) band Bloch function and  $\hat{u}_c$  ( $\hat{u}_v$ ) is the spin-down conduction (valence) band Bloch function.

electron states are considered. Later in this section, more general form of the above equation in the quantum well will be discussed. To simplify Eq. (3.7), the dot product between the unit polarization vector and the electron momentum operator is expended in the form of  $e_x p_x + e_y p_y + e_z p_z$ . Then by using Eq. (3.1) and Eq. (3.2), the expression for  $|M_T|^2$  is reduced to a very simple form as follows:

$$\begin{aligned}
 |M_T|_{hh}^2 &= \frac{1}{2} |M| \{ |-e_x - ie_y|^2 + 0 + 0 + |e_x - ie_y|^2 \} \\
 |M_T|_{lh}^2 &= \frac{1}{6} |M| \{ |2e_z|^2 + |e_x - ie_y|^2 + |-e_x - ie_y|^2 + |2e_z|^2 \} \\
 |M_T|_{so}^2 &= \frac{1}{3} |M| \{ |-e_z|^2 + |e_x - ie_y|^2 + |-e_x - ie_y|^2 + |-e_z|^2 \}
 \end{aligned} \tag{3.8}$$

Since  $e_x^2 + e_y^2 + e_z^2 = 1$ , every term of  $e_x^2 + e_y^2$  can be replaced by  $1 - e_z^2$ . The direction of  $\mathbf{k}$  vector is again assumed  $z$  direction. By this assumption,  $e_z$  can be replaced by  $\hat{\mathbf{k}} \cdot \hat{\mathbf{e}}$  where  $\hat{\mathbf{k}}$  is unit vector directed along  $\mathbf{k}$ . Then Eq. (3.7) can be rewrited in terms of  $|M_T|_v^2 / |M|^2$ , or relative transition strength as follows:

$$\frac{|M_T|_v^2}{|M|^2} = \begin{cases} e_x^2 + e_y^2 = 1 - |\hat{\mathbf{k}} \cdot \hat{\mathbf{e}}|^2 & \text{HH - band} \\ \frac{1}{3} (e_x^2 + e_y^2 + 4e_z^2) = \frac{1}{3} + |\hat{\mathbf{k}} \cdot \hat{\mathbf{e}}|^2 & \text{LH - band} \\ \frac{2}{3} (e_x^2 + e_y^2 + e_z^2) = \frac{2}{3} & \text{SO - band} \end{cases} \tag{3.9}$$

Note that Eq. (3.9) does not include any reference frame, but the relative orientation between the field polarization  $\hat{\mathbf{e}}$  and the electron  $\mathbf{k}$  vector. In Fig. 3.3 and Fig. 3.4, the dependence of the relative transition strength

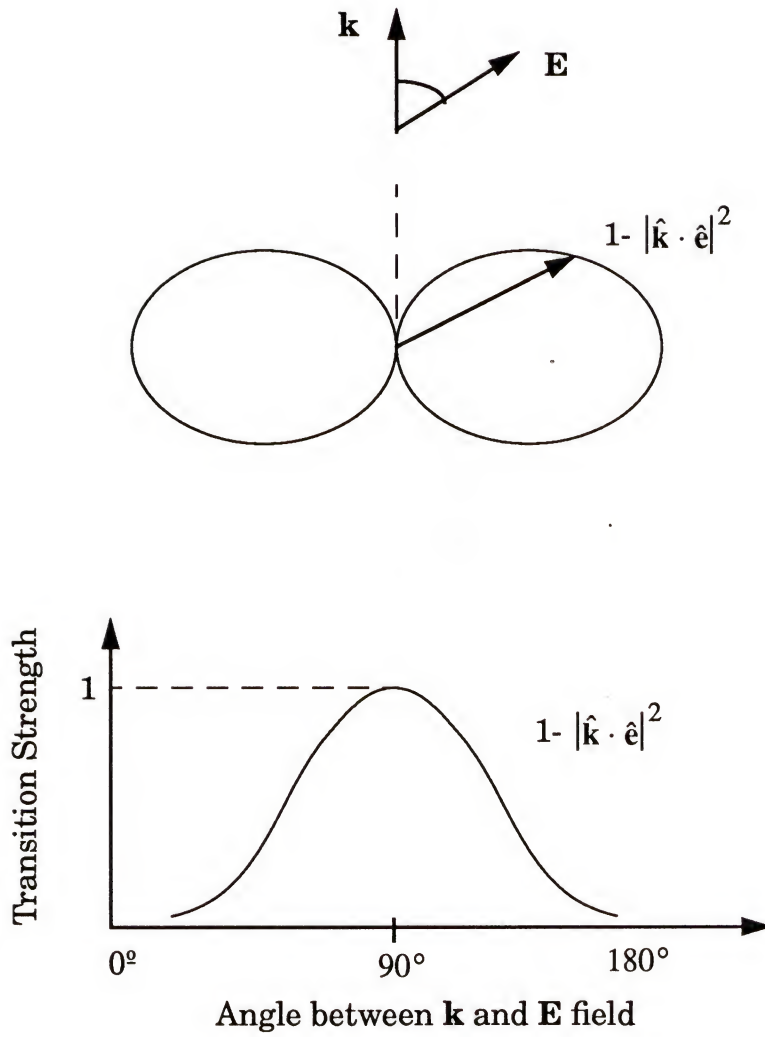


Figure 3.3 Dependence of the transition strength on angle between the electron's  $\mathbf{k}$  vector and the incident electric field vector  $\mathbf{E}$  for conduction-heavy hole transition.

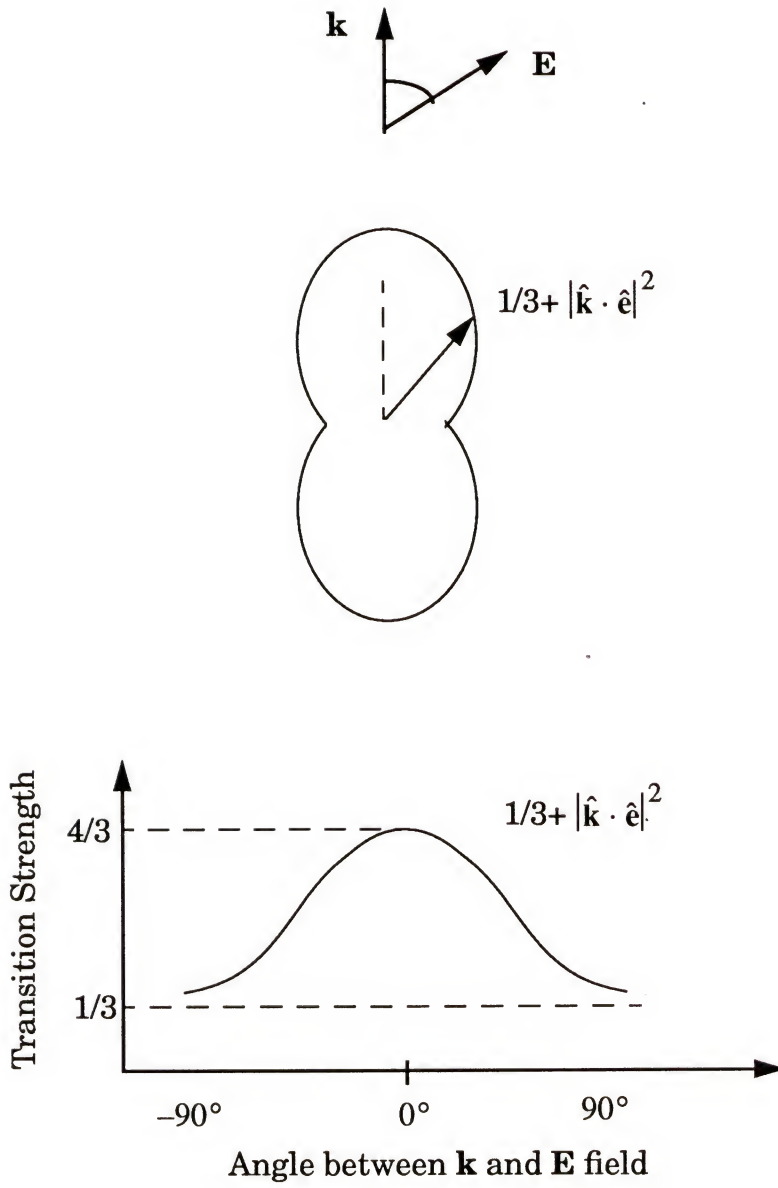


Figure 3.4 Dependence of the transition strength on angle between the electron's  $\mathbf{k}$  vector and the incident electric field vector  $\mathbf{E}$  for conduction-light hole transition.



$|M_T|^2/|M|^2$  on angle between the electron's  $\mathbf{k}$  vector and the incident electric field vector  $\mathbf{E}$  is shown. For the c-hh transition, the relative transition strength is maximum for the incident electric field ( $\mathbf{E}$ ) perpendicular to the electron  $\mathbf{k}$  vector( $\mathbf{k}$ ) and minimum for  $\mathbf{E}$  parallel to  $\mathbf{k}$ . The opposite holds for c-lh transition but it should be noted that the minimum transition strength does not vanish.

### 3.3 Polarization Anisotropy

In this section, the polarization anisotropy of the quantum well laser is considered based on the transition matrix element discussed in the previous section. For QW structure, the envelope functions are constructed from two or more plane wave states. Hence, cross terms between the various plane waves are contained which make up the confined state appears in Eq. (3.7) for QW structure [Zory 93]. However, this complexity can be simplified by restricting the region of interest into near the band edge and neglect the cross terms. In this situation, the electron  $\mathbf{k}$  vectors are quantized along certain direction. It is illustrated in Fig. 3.5 that how quantum confinement in a QW serve to polarized the momentum of the band edge electrons along certain directions. For QW lasers with heavy hole as a ground state, TE mode oscillation prevails because the transition strength is great when the light is polarized in the plane of the QW ( $\mathbf{E}$  parallel to the QW layer) as shown in Fig. 3.5(a). Conversely, when the light hole is a ground state, TM mode oscillation

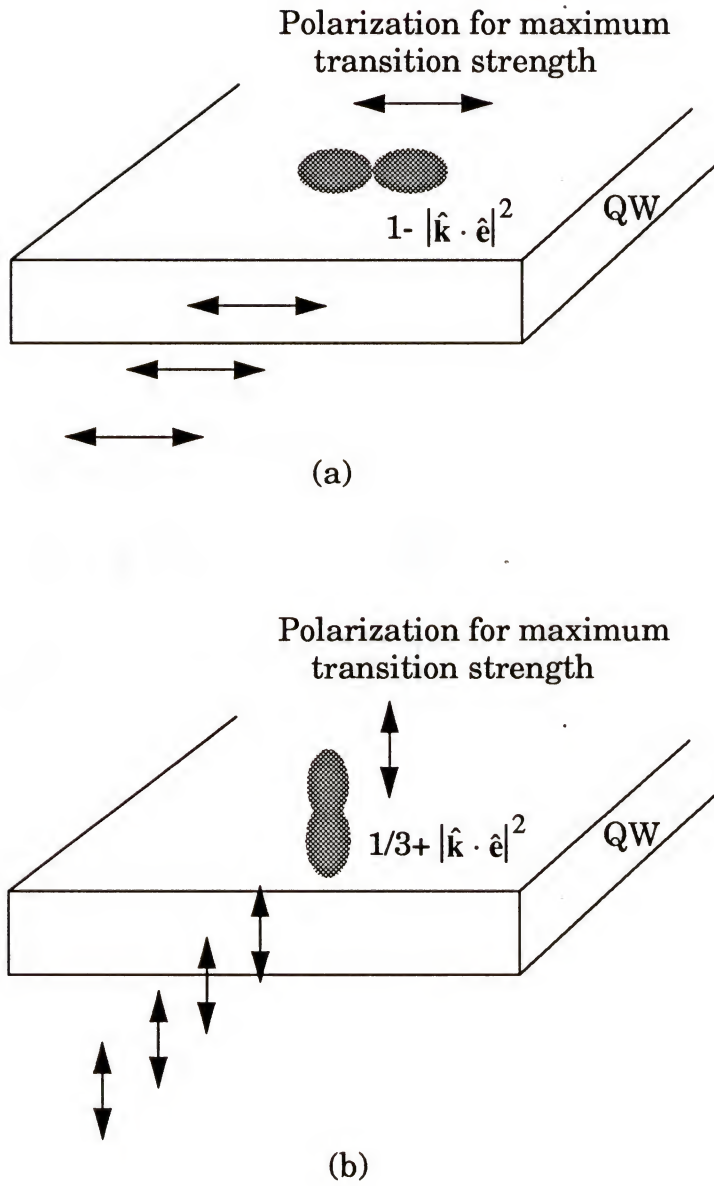


Figure 3.5 Illustration of how quantum confinement serves to polarize the momentum of band edge electrons for (a) C-HH and (b) C-LH transitions.

is predominant because the transition strength is maximum for  $\mathbf{E}$  perpendicular to the QW layer as shown in Fig. 3.5(b). The relative transition strength,  $|M_T|^2/|M|^2$ , is calculated as a function of the in-plane  $k$  vector for 80Å  $\text{Ga}_x\text{In}_{1-x}\text{P}/(\text{Al}_{0.6}\text{Ga}_{0.4})_{0.5}\text{In}_{0.5}\text{P}$  quantum well lasers with  $x=0.3, 0.4, 0.5$ , and  $0.6$  and illustrated in Fig. 3.6 for TE and Fig. 3.7 for TM polarization. For TE polarization, the transition strength of QW lasers with  $x=0.3, 0.4$ , and  $0.5$  are very strong near the band edge because the valence band ground state is heavy hole state for these devices. However, for TM polarization, the transition strength of QW lasers with  $x=0.6$  is much stronger than other materials because the light hole is the valence band ground state.

### 3.4 Experiment

In this section, the in-plane spontaneous emissions of 80Å  $\text{Ga}_x\text{In}_{1-x}\text{P}/(\text{Al}_{0.6}\text{Ga}_{0.4})_{0.5}\text{In}_{0.5}\text{P}$  quantum well lasers with  $x=0.3$  and  $0.4$  (compressive strain),  $x=0.5$  (lattice matched), and  $x=0.6$  (tensile strain) are investigated. Samples were grown by organometallic vapor phase epitaxy (OMVPE) provided by Xerox Palo Alto Research Center. The QW is contained within a typical diode laser structure as shown in Fig. 2.4. Confining layers are undoped  $(\text{Al}_{0.6}\text{Ga}_{0.4})_{0.5}\text{In}_{0.5}\text{P}$ , while p- and n-cladding layers are  $\text{Al}_{0.5}\text{In}_{0.5}\text{P}$ . Diodes were 100μm wide by 500μm long stripes with cleaved facets, which were probe contacted and pulse tested.

The emitted light was collected, and focused onto the entrance slit of a

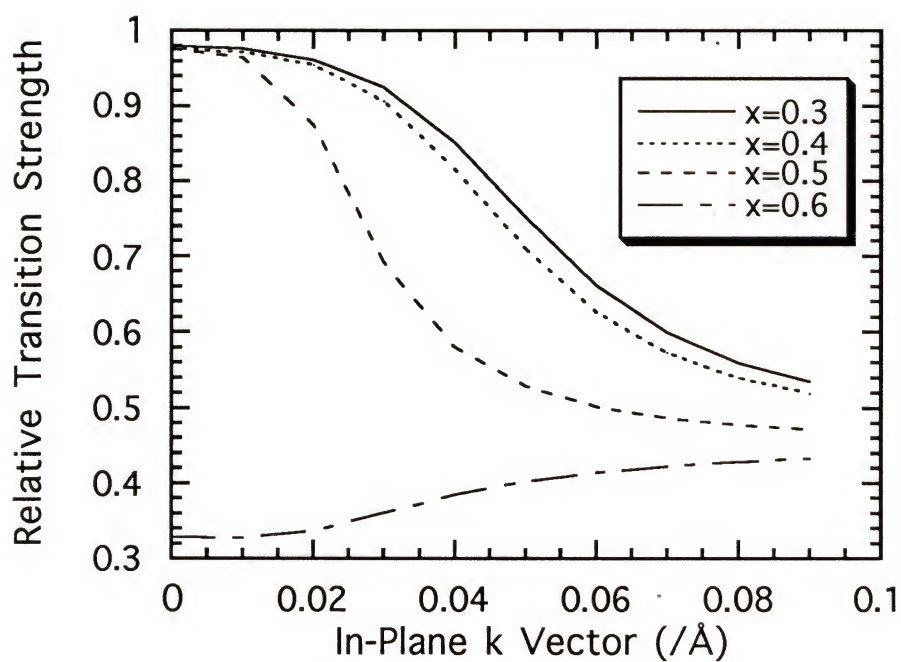


Figure 3.6 Relative transition strength of conduction to first valence band TE polarization for 80Å  $\text{Ga}_x\text{In}_{1-x}\text{P}/(\text{Al}_{0.6}\text{Ga}_{0.4})_{0.5}\text{In}_{0.5}\text{P}$  quantum well lasers with  $x=0.3, 0.4, 0.5$ , and  $0.6$



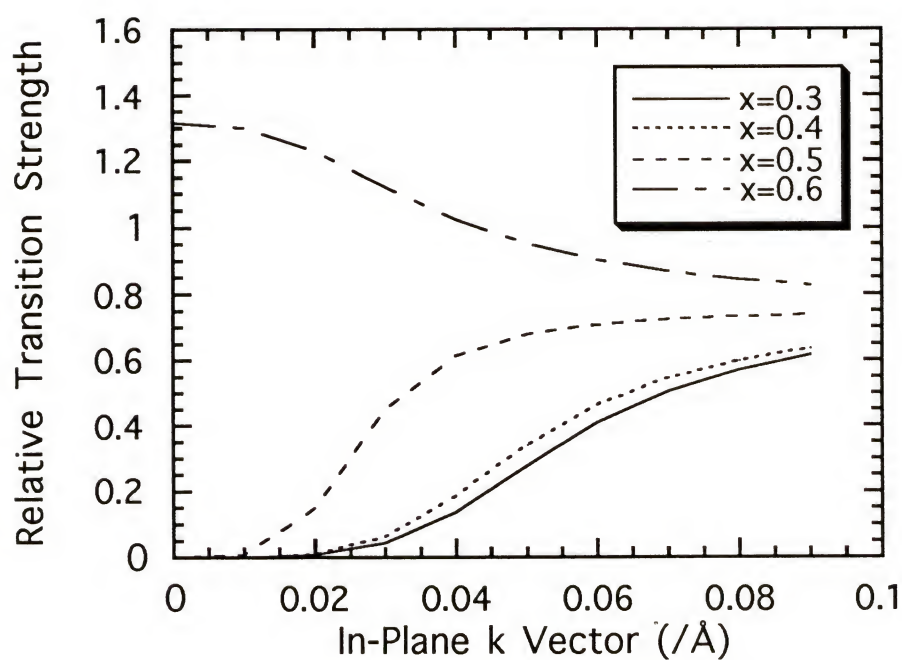


Figure 3.7 Relative transition strength of conduction to first valence band TM polarization for  $80\text{\AA}$   $\text{Ga}_x\text{In}_{1-x}\text{P}/(\text{Al}_{0.6}\text{Ga}_{0.4})_{0.5}\text{In}_{0.5}\text{P}$  quantum well lasers with  $x=0.3, 0.4, 0.5$ , and  $0.6$

spectrometer, using a microscope objective. A Glan-Thompson Air-Spacing Polarizer (clear aperture 10mm) was used to analyze the spontaneous emission in the desired polarization. Shown in Fig. 3.8, Fig. 3.9, and Fig. 3.10 are the TE mode and TM mode electroluminescence (EL) spectra of the three samples for  $x=0.4$ ,  $0.5$ , and  $0.6$ , taken at a current density of about 200, 130, and 100mA respectively. As the GaP alloy content in the QW is increased from  $x=0.4$  to  $x=0.6$ , the band gap increases and there is a net shift to shorter wavelength. The polarization of the EL spectra is anisotropic, with the e-hh transition TE polarized, and e-lh transition predominantly TM polarized.

For the compressively strained QWs ( $x=0.3$  and  $x=0.4$ ), the TE mode emission is strongest, because the hh band is ground state. The opposite is true for tensile strain ( $x=0.6$ ), in which case the TM mode emission is most intense because the valence band edges have become reversed. At very low current densities (less than  $5\text{A/cm}^2$ , for which band filling is negligible and the Boltzmann approximation to the Fermi distribution applies), the relative intensity between the TE and TM mode emission ( $I_{\text{TE}}/I_{\text{TM}}$ ) follows the ratio between the occupancy factors for the lh and hh bands, i.e.,  $\exp(\Delta E_{\text{TM-TE}}/kT)$ , where  $\Delta E_{\text{TM-TE}}$  is the hh-lh band edge difference, and  $kT$  is the thermal energy; this is summarized in Table 3.1. The case near lattice match ( $x=0.5$ ) has the lh and hh band edges nearly degenerate, resulting in similar wavelength and intensity. Exact degeneracy of the lh and hh band edges requires slight biaxial tension, however. For this QW thickness, the

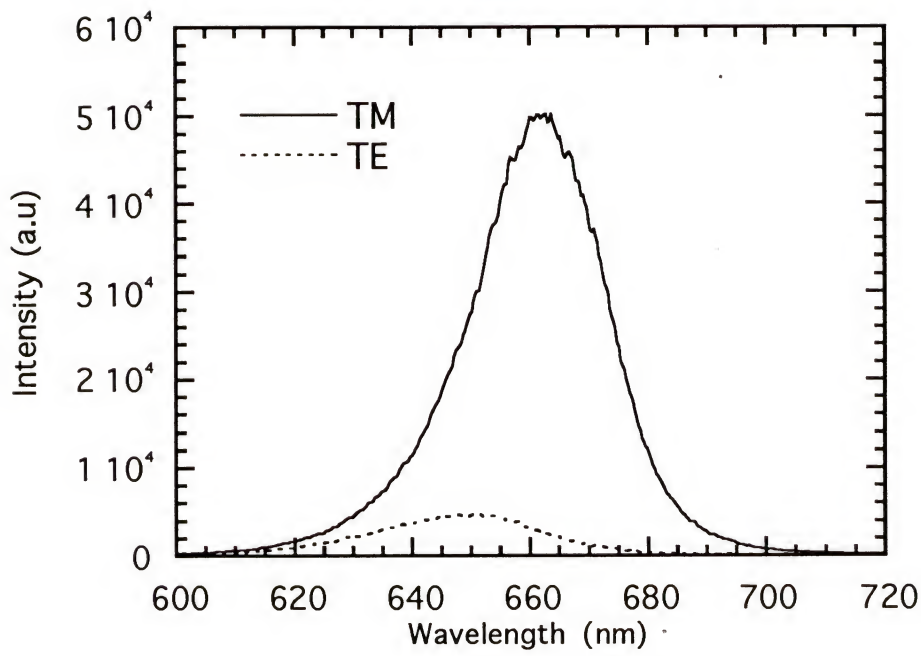


Figure 3.8 Electroluminescence of  $80\text{\AA}$   $\text{Ga}_x\text{In}_{1-x}\text{P}/(\text{Al}_{0.6}\text{Ga}_{0.4})_{0.5}\text{In}_{0.5}\text{P}$  quantum well lasers ( $x=0.4$ ) analyzed in both TE and TM polarizations, at a current  $I=200\text{mA}$ .

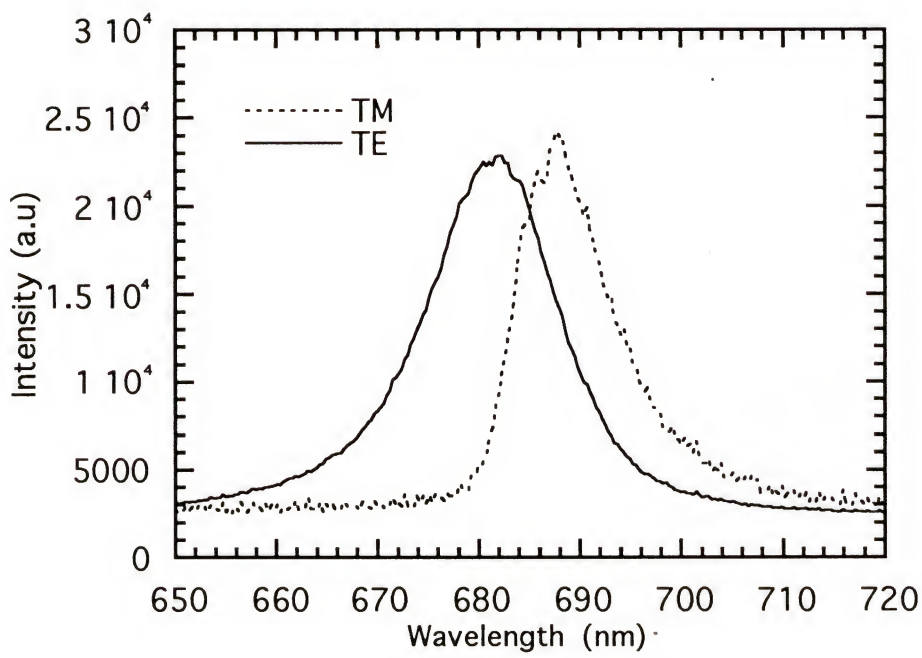


Figure 3.9 Electroluminescence of  $80\text{\AA}$   $\text{Ga}_x\text{In}_{1-x}\text{P}/(\text{Al}_{0.6}\text{Ga}_{0.4})_{0.5}\text{In}_{0.5}\text{P}$  quantum well lasers ( $x=0.5$ ) analyzed in both TE and TM polarizations, at a current  $I=130\text{mA}$ .



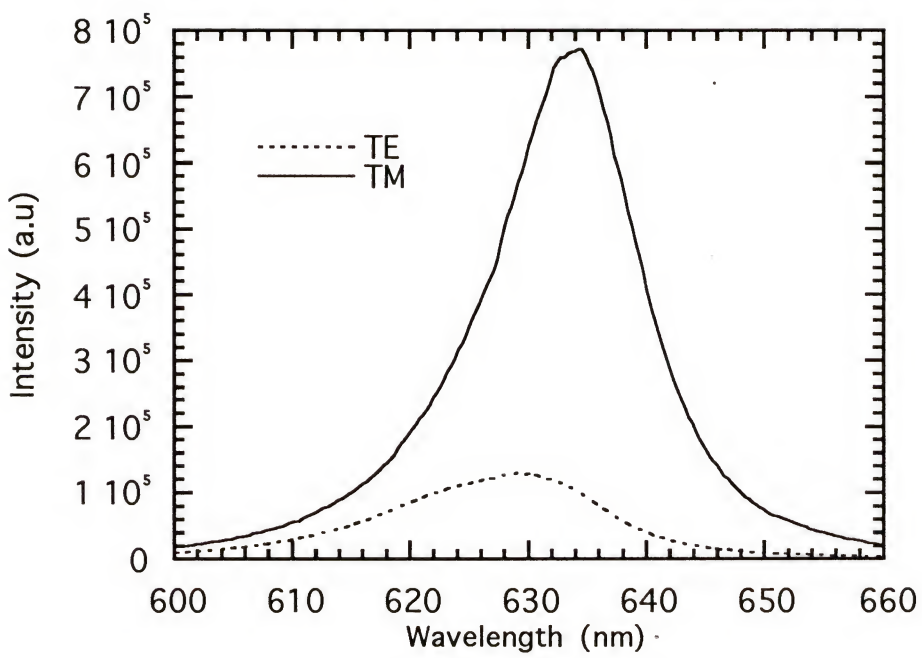


Figure 3.10 Electroluminescence of  $80\text{\AA}$   $\text{Ga}_x\text{In}_{1-x}\text{P}/(\text{Al}_{0.6}\text{Ga}_{0.4})_{0.5}\text{In}_{0.5}\text{P}$  quantum well lasers ( $x=0.6$ ) analyzed in both TE and TM polarizations, at a current  $I=100\text{mA}$ .

Table 3.1  
The comparison of the TE and TM emission

x	$I_{TE/TM}$	$\Delta E_{TM-TE}$ (Experiment)	$\Delta E_{TM-TE}$ (Theory)	$\exp(\Delta E_{TM-TE}/kT)$
0.3	6.5	42.0 meV	32.1meV	5.1
0.4	4.2	33.2 meV	32.7meV	3.6
0.5	0.95	-1.0 meV	6.1 meV	0.96
0.6	0.56	-12.4 meV	-30.1meV	0.62

appropriate composition is  $x=0.53$  [Bour 93]. The energy separation between the TE and TM mode spontaneous emission peaks reflects the energy difference between the light and heavy hole band edges. Contributing to this difference are both the strain induced splitting of the lh and hh bands, and the different quantum shifts of the two valence bands [Pan 88, Kond 91, Wang 90, Van 89]. The measured energy separation ( $\Delta E_{\text{TM-TE}}$ ) as well as the calculated value is given in the Table 3.1. The theoretical value was calculated based on the c-hh and c-lh  $n=1$  energy level difference calculated in Chapter II. Since the origin of the TE-TM peak wavelength separation is the hh and lh splitting at the band edge due to the shear strain deformation, the polarization anisotropy can be predicted simply by calculating the energy split defined in Eq. (2.12). There was significant disagreement between the theory and the experiment for  $x=0.3$  and  $0.4$  and this will be discussed in detail in the next section.

The current density dependence of the TE and TM mode spontaneous emission peak wavelength are shown in Fig. 3.11. The wavelength separation between TE and TM mode emission is constant at low current densities. At elevated current densities, however, bandfilling begins to occur, and the wavelength of the fundamental transition shortens with increasing injection current. This bandfilling effect is most pronounced in the devices with  $x=0.3$  and  $x=0.4$ , suggesting that the in-plane effective mass of heavy holes is reduced in such QWs under biaxial compression. Furthermore, the

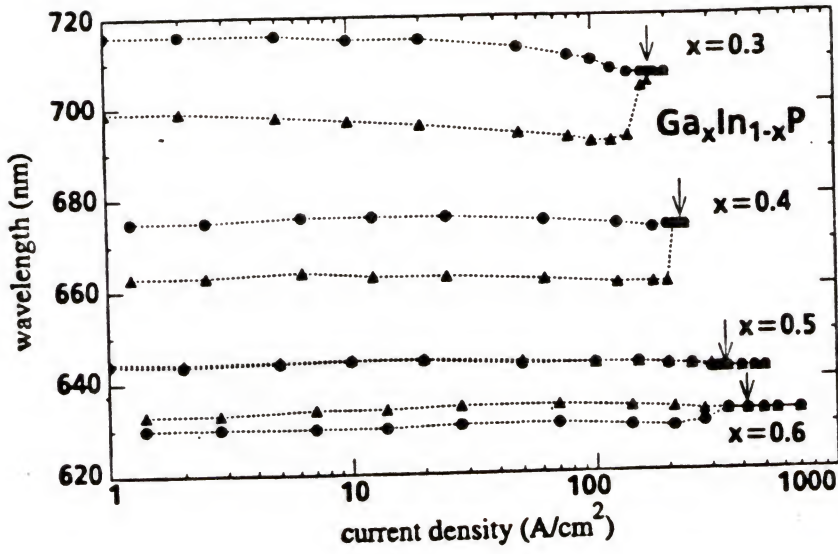


Figure 3.11 Current density dependence of spontaneous emission peak wavelength for 80Å  $\text{Ga}_x\text{In}_{1-x}\text{P}/(\text{Al}_{0.6}\text{Ga}_{0.4})_{0.5}\text{In}_{0.5}\text{P}$  quantum well lasers ( $x=0.3, 0.4, 0.5, 0.6$ ) analyzed in both TE and TM polarizations.



threshold current density is also lowest in these devices, because population inversion occurs at a lower QW carrier density when the in-plane effective mass of the hh band is reduced.

For the devices with  $x=0.5$  and  $0.6$ , a shift to shorter wavelengths at high current density is not apparent. This suggests that the in-plane hole effective mass might be greater than for the compressively strained QWs. Thresholds are also higher in these devices, increasing to  $400\text{A/cm}^2$  for the TM mode device with  $x=0.6$ . Presumably, this is due to both their higher in-plane effective masses, and the diminishing electron confinement at short wavelengths. This will be more clarified in the next section. Also in Fig. 3.11, the reversal in the hh and lh band edges is evident, as the biaxial QW strain progresses from compression to tension.

Above threshold, the polarization of stimulated emission was predominantly the same as that of the fundamental transition. The spectra for  $x=0.4$ , and  $0.6$  devices at the threshold and high injection for the alternative polarization (TM for  $x=0.4$  and TE for  $x=0.6$ ) are shown in Fig. 3.12, and Fig. 3.13. The lasing peak wavelength appeared at the same wavelength with the fundamental transition lasing peak rather than around the middle of the spontaneous emission spectrum and hence the polarization state of laser oscillation was not pure.

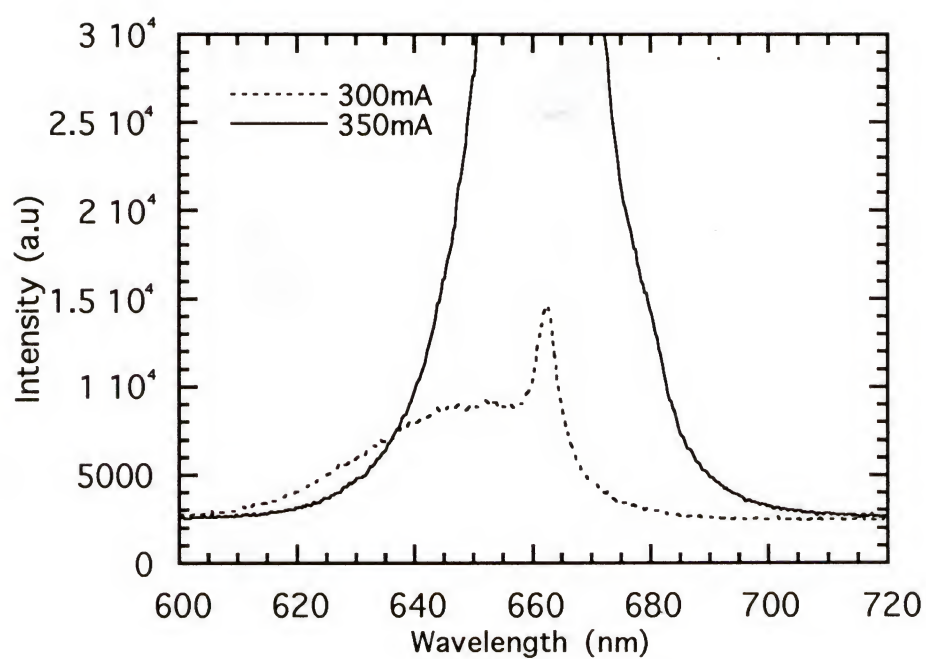


Figure 3.12 The measured TM spectrum of  $\text{Ga}_{0.4}\text{In}_{0.6}\text{P}$  80Å QW lasers near the threshold (300mA) and well above the threshold (350mA)

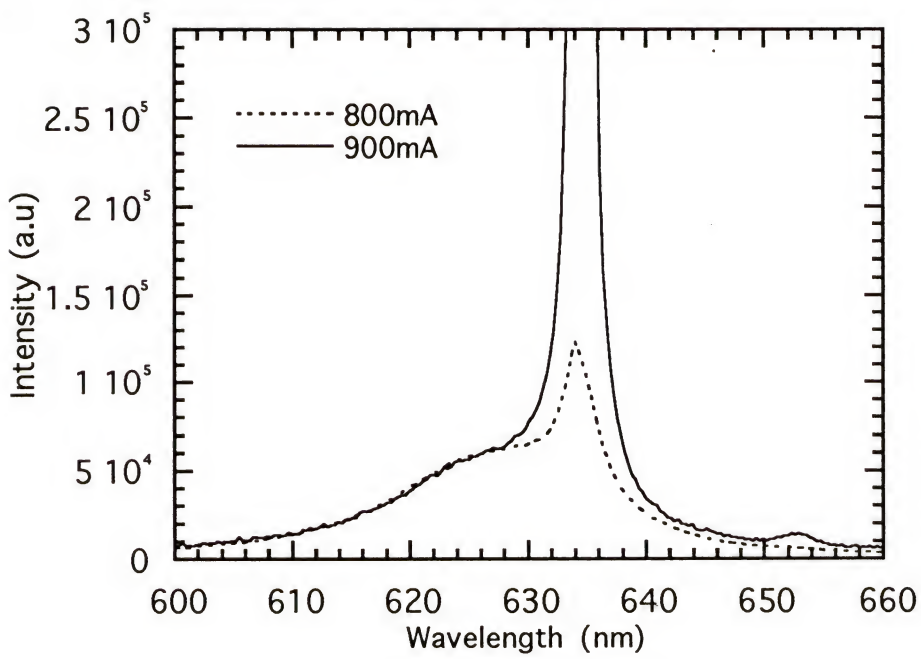


Figure 3.13 The measured TE spectrum of Ga<sub>0.6</sub>In<sub>0.4</sub>P 80Å QW lasers near the threshold (800mA) and well above the threshold (900mA)

### 3.5 Discussion

It has become apparent that the lowering of valence band effective mass can have considerable benefits for semiconductor lasers [Yabl 86]. The intentional incorporation of strain in QW layer has become popular technique for reduction of the valence band effective mass. The compressive strain as well as tensile strain causes a considerable reduction of the in-plane effective mass [Krij 92]. As a result, the hole density states is reduced and, in the ideal case, becomes comparable to the electron density of states. In such condition, the carrier density required for degeneracy would be minimized and the Bernard -Durauffourg condition [Bern 61]  $(F_c - F_v) > h\nu \geq E_g$  could be satisfied at a low carrier density with accompanying benefits in terms of threshold current density [Yabl 88].

The energy vs. in-plane  $k$  dispersion under the strain effect can be calculated by estimating the deformation potentials in the QW layer and inserting into the Hamiltonian as discussed in chapter II. The results were shown in Fig. 2.10 and Fig. 2.11. By assuming that the peak emission of light came from the band edge transition from conduction electron to the heavy hole (TE) and light hole (TM), the peak TE and TM wavelength difference ( $\Delta E_{TM-TE}$ ) were predicted as listed in Table 3.2. As discussed in the previous section, however, there was considerable disagreement in the  $\Delta E_{TM-TE}$  between the experiment and the theory. In determining  $\Delta E_{TM-TE}$ , the most important factor is the shear deformation potential because the hh and the lh state are



split by this strain. The splitting (S) is defined as [Poll 68, Gavi 70, Chan 77]

$$\begin{aligned} S &= \Delta E_h (\text{shear}) - \Delta E_l (\text{shear}) \\ &= \delta E_{001} - \frac{1}{2} \cdot \frac{(\delta E_{001})^2}{\Delta_o} \end{aligned} \quad (3.10)$$

where  $\delta E_{001}$  is the linear splitting of the  $p_{3/2}$  multiplet for stress parallel to [001] direction defined as  $\delta E_{001} = 2b(\epsilon_{zz} - \epsilon_{xx})$  and  $b$  is the shear deformation potential. The strain tensors  $\epsilon_{xx}$  and  $\epsilon_{zz}$  are given as

$$\begin{aligned} \epsilon_{zz} &= -\frac{2C_{12}}{C_{11}}\epsilon_{xx} \\ \epsilon_{xx} = \epsilon_{yy} &= \frac{a_{cb} - a_{qw}}{a_{qw}} \equiv \frac{\Delta a}{a_{qw}} \end{aligned} \quad (3.11)$$

Combining Eq. (3.10) and Eq. (3.11);

$$S = 2b\left(\frac{\Delta a}{a_{qw}}\right)\left(-\frac{2C_{12} + C_{11}}{C_{11}}\right) - \frac{2}{\Delta_o} \cdot \left(\frac{\Delta a}{a_{qw}}\right)^2 \left(-\frac{2C_{12} + C_{11}}{C_{11}}\right)^2 \quad (3.12)$$

The second term in Eq. (3.12) is often neglected for large  $\Delta_o$  such as GaAs ( $\Delta_o \approx 340\text{meV}$ ), but must be included for small  $\Delta_o$  such as GaInP ( $\Delta_o \approx 110\text{meV}$ ).

The parameters used in Eq. (3.12) for  $\text{Ga}_x\text{In}_{1-x}\text{P}$  were linearly interpolated from host alloys GaP and InP. The only factor in Eq. (3.12) which depends strongly on  $x$  is  $\Delta a/a_{qw}$  where  $\Delta a$  is the lattice constant difference between the quantum well and the barrier layer  $a_{\text{barrier}} - a_{qw}$ . In Fig. 3.14.,  $a_{\text{barrier}}/a_{qw}$  vs.  $x$  is plotted. The solid line is derived from linear interpolation of the lattice constants of GaP and InP and the triangles are determined so that the

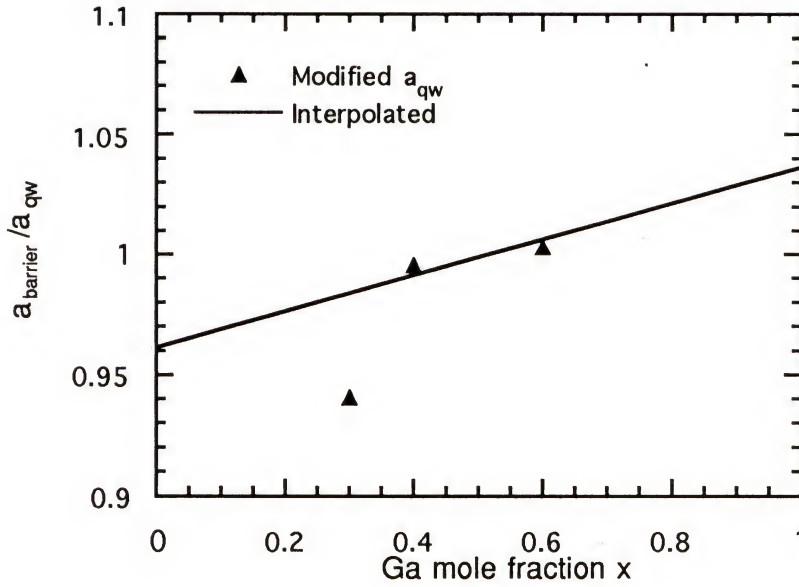


Figure 3.14 The ratio of  $a_{\text{barrier}}/a_{\text{qw}}$  of  $\text{Ga}_x\text{In}_{1-x}\text{P}$  as a function of Gallium mole fraction  $x$  assuming  $a_{\text{barrier}}=5.6533\text{\AA}$ . The solid line is linearly interpolated data from GaP and InP and the triangles are determined so that the calculated splitting  $S$  yields the same  $\Delta E_{\text{TE-TM}}$  as experiment.

calculated splitting yields the same  $\Delta E_{\text{TE-TM}}$  as experiment. For  $x=0.53$ , QW layer is nearly lattice matched to the barrier layer. As can be seen in Fig. 3.14, the ratios ( $a_{\text{barrier}}/a_{\text{qw}}$ ) for modified  $a_{\text{qw}}$  for  $x=0.4$  (about 0.8% lattice mismatch) and  $x=0.6$  (about 0.6% lattice mismatch) are close to the interpolated data. However, for  $x=0.3$  (about 1.6% lattice mismatch), there is a significant deviation from the interpolated data. This implies that the strain acting on the QW layer may not be simply derived from Eq. (3.12) but from a more complicated form for lattice mismatches beyond certain range. As shown in chapter II, the energy shift in a strained QW was defined based on the recoil force due to the lattice mismatch by analogy with Hook's law. Although a strained QW layer can avoid the development of interfacial dislocations if the thickness is less than a certain critical value, the strain effect can be more complicated for a highly strained layer. For the 1.6% lattice mismatch case ( $x=0.3$ ), it may be that Eq. (3.12) is no longer valid. On the other hand, it may be that the linear interpolation shown in Fig. 3.14 for GaInP is incorrect. In any event, polarization anisotropy spectroscopy provides a means for studying these new strained QW structure.

## CHAPTER IV

### TEMPERATURE DEPENDENCE OF THE THRESHOLD CURRENT DENSITY OF CdZnSe BLUE-GREEN QUANTUM WELL LASERS

#### 4.1 Introduction

Blue semiconductor lasers have great advantages over commonly used infrared (IR) lasers. For example, optical readout and storage densities can be increased by a factor of three if one substitutes a blue laser for an IR laser. Despite the advantages, the development of ZnSe-based blue semiconductor lasers has been slow because of the difficulty in growing good p-type material. Recently, a new p-type growth technique using a Nitrogen plasma during molecular beam epitaxy (MBE) has been developed [Park 90]. This technique was used to make the first blue-green semiconductor injection laser by researchers from 3M [Haas 91]. Since then, various kinds of II-VI material have been investigated for better performance and reliability. These achievements give us confidence that we are on the right path toward compact, room temperature operating blue diode lasers. Recently, Okuyama *et al* [Okyu 91] proposed ZnMgSSe as a new cladding layer material. Gaines *et al* [Gain 93] proved its superiority by achieving the lowest room temperature threshold current density and the highest operating temperature using a  $\text{Cd}_{0.2}\text{Zn}_{0.8}\text{Se}$  quantum well,  $\text{ZnS}_{0.06}\text{Se}_{0.94}$  barriers, and



$\text{Zn}_{0.9}\text{Mg}_{0.1}\text{S}_{0.1}\text{Se}_{0.9}$  cladding layers. Using this same QW structure, Haase *et al* [Haas 93] from 3M reported more recently the record low threshold current with a buried ridge waveguide design. In this chapter, we calculate the threshold current density of CdZnSe/ZnSe strained single quantum well diode lasers over a wide temperature range and compare with the published experimental data.

#### 4.2 Spontaneous emission rate and gain spectra

Using the  $E$  vs.  $k$  dispersion derived in the chapter 2, the quasi-Fermi energy levels were calculated. The carrier densities of the conduction and valence band can be written as

$$N = \frac{m_c k_B T}{\pi \hbar^2 L} \sum_n \ln \{ 1 + \exp [-(E_{cn} - E_{fc}) / (k_B T)] \}$$

$$P = 2 \sum_n \int_0^{k_{\max}} \rho^{2D}(k_{xy}) \{ 1 - f_v [E_{vn}(k_{xy})] \} dk_{xy}$$
(4.1)

where  $E_{fc}$  ( $E_{fv}$ ) is the quasi-Fermi level of the conduction (valence) band,  $L$  is the thickness of the QW,  $f_v$  is the fermi distribution function for the valence band,  $f_v = 1/[1 + \exp\{E - E_{fv}\}/k_B T]$ , and  $E_{cn}$  ( $E_{vn}$ ) are the quantized energy level of the conduction (valence) band. The density of the state,  $\rho(k_{xy})$ , for two dimensional electron system is given by  $\rho(k_{xy}) = \frac{k_{xy}}{2\pi} \cdot \frac{1}{L}$ . The summation in Eq. (4.1) should be done over all quantized energy states, even on the unbounded states which have higher energies than QW barrier as pointed out

by Nagarajan *et al* [Naga 89], for a numerical accuracy. This is important especially for high injection case. The quasi Fermi levels with respect to the carrier density, N or P, were found by assuming the charge neutrality,  $N=P$ , and the results are shown in Fig. 4.1 and Fig. 4.2.

The spontaneous emission rate ( $r_{sp}$ ) is given by [Zory 93]

$$r_{sp}(h\nu) = \left(\frac{2\pi}{\hbar}\right) \left(\frac{e}{m_0}\right)^2 \left(\frac{2\hbar(\omega/\epsilon)}{4\omega}\right) |M_T|^2 \rho_{red}(h\nu) \rho_{opt}(h\nu) f_c (1 - f_v) \quad (4.2)$$

where  $e$  is the electron charge,  $m_0$  is the free electron rest mass,  $\epsilon$  is the electric permittivity,  $\rho_{opt}(h\nu)$  is the optical mode density,  $|M_T|^2$  is the transition matrix element defined in Eq. (3.7),  $f_c(f_v)$  is the fermi distribution of conduction (valence) band, and  $\rho_{red}(h\nu)$  is the reduced density of states given by

$$\rho_{red}(h\nu) = \left[ \frac{\rho}{dE_{ch}/dk_{\parallel}} \right] \Big|_{E=h\nu} \quad (4.3)$$

Since one cannot use the closed form expression for  $\rho_{red}(h\nu)$  for the nonparabolic valence band case, we calculated numerically from the energy vs. in-plane  $k$  vector dispersion curve.

The spectral gain is given by [Zory 93]

$$g(h\nu) = \frac{2\pi e^2 \hbar}{\epsilon_0 \lambda n c m_0^2 h\nu} |M_T|^2 \rho_{red}(h\nu) (f_c - f_v) \quad (4.4)$$

where  $n$  is a refractive index parameter,  $c$  is the speed of light, and  $\lambda$  is the wavelength. The calculated spontaneous emission rate and the gain spectra for  $Cd_{0.2}Zn_{0.8}Se$  are shown in Fig. 4.3. and Fig. 4.4.

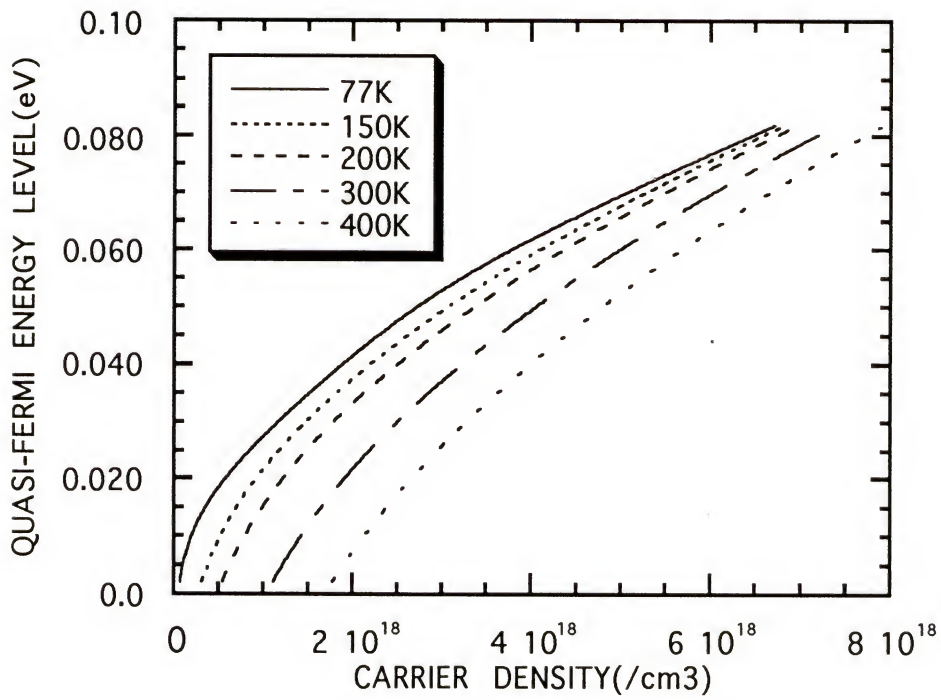


Figure 4.1 The quasi-Fermi energy levels for  $\text{Cd}_{0.2}\text{Zn}_{0.8}\text{Se}$  65Å QW structure. The zero energy level is the conduction band edge of the QW.

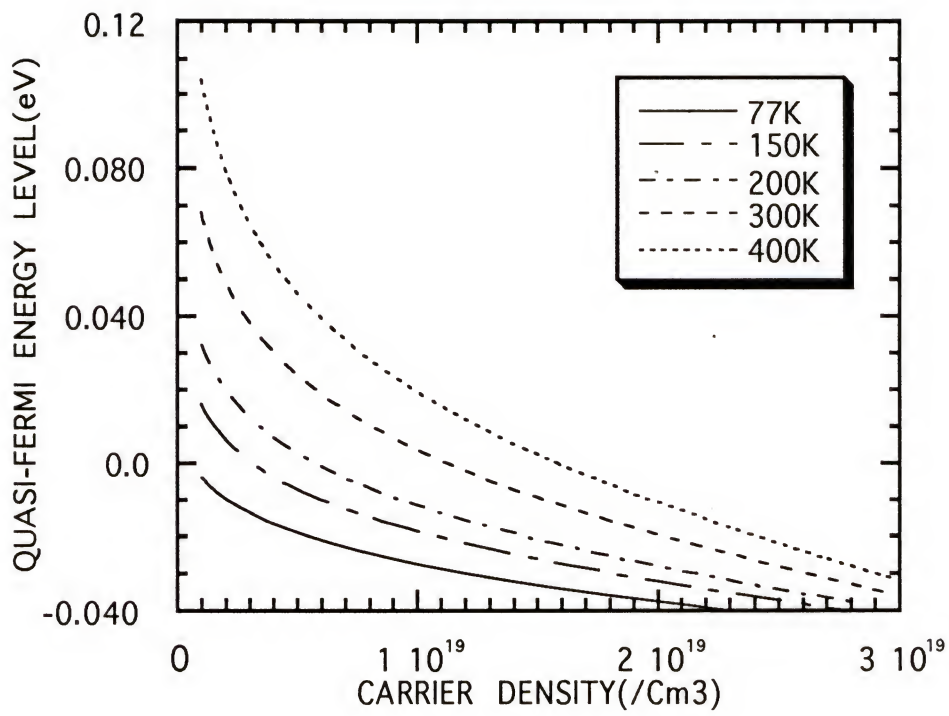


Figure 4.2 The quasi-Fermi energy levels for  $\text{Cd}_{0.2}\text{Zn}_{0.8}\text{Se}$  65Å QW structure. The zero energy level is the valence band edge of the QW.



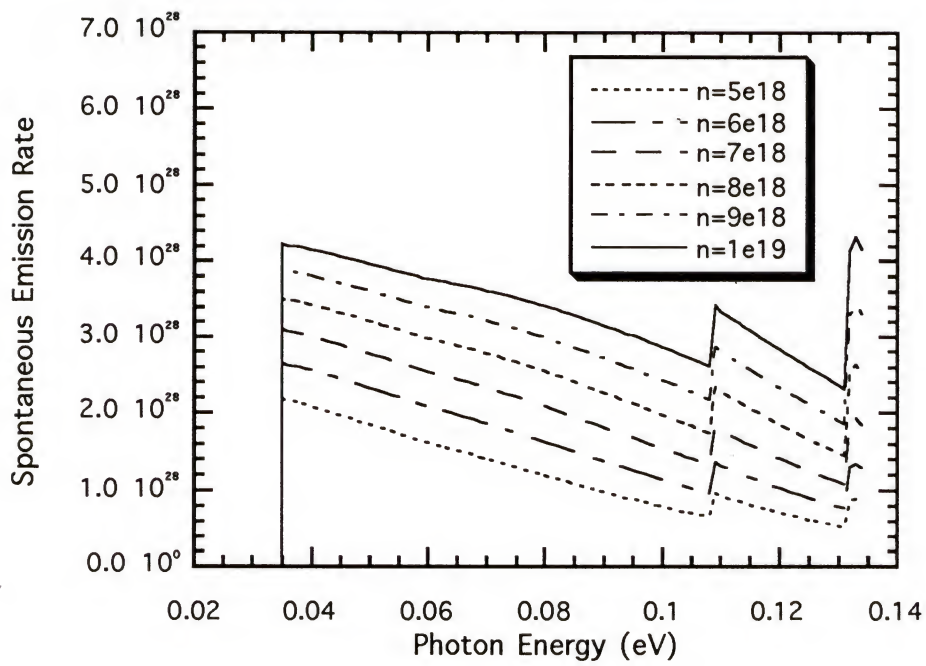


Figure 4.3 Spontaneous spectra of CdZnSe 65Å QW diode lasers.

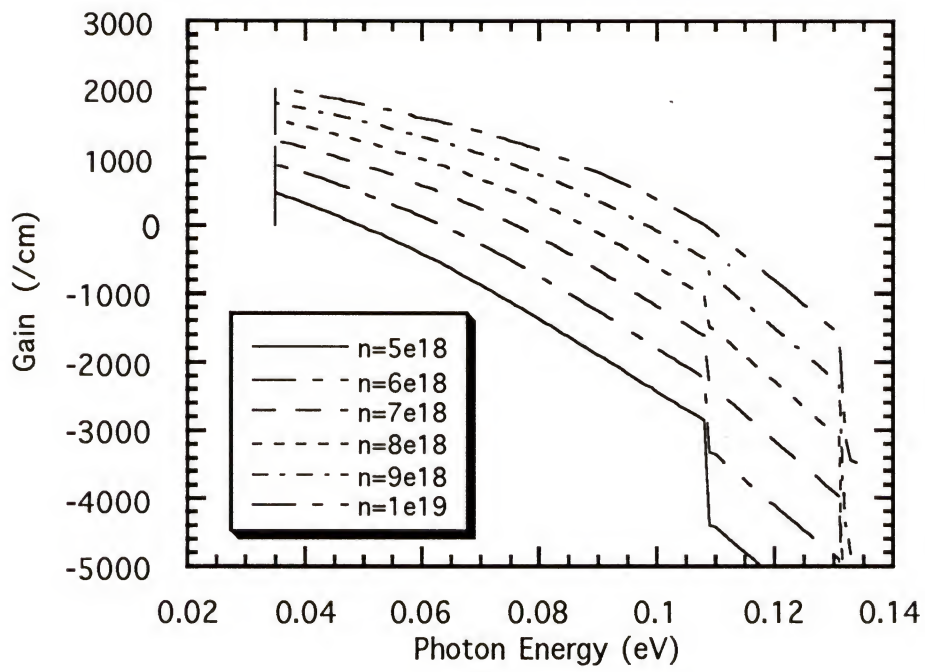


Figure 4.4 Spectral gain of CdZnSe 65Å QW diode laser

### 4.3 Intraband Relaxation and Line Shape Function

Line shape functions, representing homogeneous broadening due to carrier scattering, are defined as response functions of dipole phase damping [Yama 87]. Line shapes for optical transitions play an important role in estimating optical properties such as a gain and a spontaneous emission spectra. It is widely accepted that the line shape function for semiconductors is the Lorentzian function [Yama 81], in analogy with the gas laser theories. However, when the Lorentzian function is applied to QW semiconductor lasers, the gain coefficients are underestimated and an unnatural absorption region appears at photon energies below the band gap in gain spectra [Lim 91]. Recently, line shape functions for QW structures were theoretically analyzed by taking non-Markovian relaxation processes into account [Yama 87, Asad 89, Ohto 91]. It has been found that the line shape functions in low dimensional systems have a strong convergent characteristic and asymmetry. Since the scattering time of ZnSe-based material is known to be very short compared to conventional III-V materials such as GaAs [Nurm 93], the proper choice of the line shape function is very important.

The line shape function  $L(h\nu)$  is given by the Fourier transform of the optical dipole moment  $P(t)$  [Yama 87]:

$$L(h\nu) = \frac{1}{2\pi\hbar} \cdot \int_{-\infty}^{\infty} P(t) e^{\pm i\omega t} dt \quad (4.5)$$

The dipole moment  $P(t)$ , which is damped due to carrier scattering, can be

written as

$$P(t) = P(0) e^{\mp i\omega_0 t} e^{-F(t)} \quad (4.6)$$

where  $\omega_0$  is the resonant angular frequency and  $F(t)$  is the phase damping factor. Here, it is important to include the non-Markovian processes which bring about the nonlinear time dependence of the damping factor  $F(t)$ . This gives rise to the crucial difference between the present line shape and the conventional Lorentzian one. Without tracing the temporal behavior of dipole momentum  $P(t)$ , Asada obtained the Fourier transform of  $P(t)$  using the temperature Green's method [Asad 89]. In that work, hole-hole, hole-electron, and carrier-longitudinal optical (LO) phonon scattering time were analyzed. It has been found that hole-hole scattering is dominant among the various scattering due to its heavy effective mass. Moreover, an approximate form of the line shape  $L(h\nu)$  for numerical calculation has been derived for hole-hole scattering (which dominates the various scattering processes) as follows [Zory 93]:

$$L(h\nu - E_{cv}) \cong \frac{1}{\pi} \cdot \frac{\Gamma(h\nu - E_{cv})}{(h\nu - E_{cv} - \Delta)^2 + \Gamma^2(h\nu - E_{cv})} \quad (4.7)$$

where



$$\begin{aligned}
\Gamma(h\nu - E_{cv}) &\cong \frac{\hbar}{2\tau_v} \cdot \frac{1 + e^{(h\nu - E_{cv})/(kT)}}{1 + e^{-E_{fv}/kT}} e^{-K|E|/(kT)} \\
\Delta &\cong -\frac{e^2}{4\epsilon L_{vj}} T^{1/2} (0, k_v, k_v) n_{2D} \\
K &= \frac{e^4 \tau_v}{48\pi\epsilon^2 \hbar k T L_v^2} \cdot \frac{T(0, k_v, k_v)}{1 + e^{-E_{fv}/(kT)}} \cdot \frac{2m_v kT}{\hbar^2} \\
T(0, k_v, k_v) &\cong \left[ \frac{2}{\alpha} + \frac{1}{\alpha + 4k_v^2} \right] \\
\alpha &= \frac{\pi \hbar^2 \epsilon}{e^2} \left( \frac{1}{\sum_j [(m_c f_c(E_{cj})/L_{cj} + m_v f_v(E_{vj})/L_{vj})]} \right)
\end{aligned} \tag{4.8}$$

where  $\tau_v$  is the hole-hole scattering time,  $E_{fv}$  is the quasi-Fermi energy level,  $L_{vj}$  is the effective quantum well width for  $j$ th valence band holes,  $n_{2D}$  is the two dimensional carrier density,  $\epsilon$  is the electrical permittivity,  $m_c(m_v)$  is the electron (hole) effective mass,  $E_{cj}$  ( $E_{vj}$ ) is the  $j$ th energy level of the conduction (valence) band, and  $k_v$  is the valence band in-plane  $k$  vector. As defined in Eq. (4.8),  $\Gamma(h\nu - E_{cv})$  is a function of the photon energy. However, for the conventional Lorentzian line shape function,  $\Gamma(h\nu - E_{cv})$  is simply  $\hbar/\tau_{in}$ :

$$L(h\nu - E_{cv}) = \frac{1}{\pi} \cdot \frac{\hbar/\tau_{in}}{\pi(h\nu - E_{cv})^2 + \left(\hbar/\tau_{in}\right)^2} \tag{4.9}$$

where  $\tau_{in}$  is the intraband relaxation time. The comparison between the Lorentzian and modified Lorentzian line shape function for CdZnSe 65Å QW is illustrated in Fig. 4.5. As can be seen in the figure, the modified

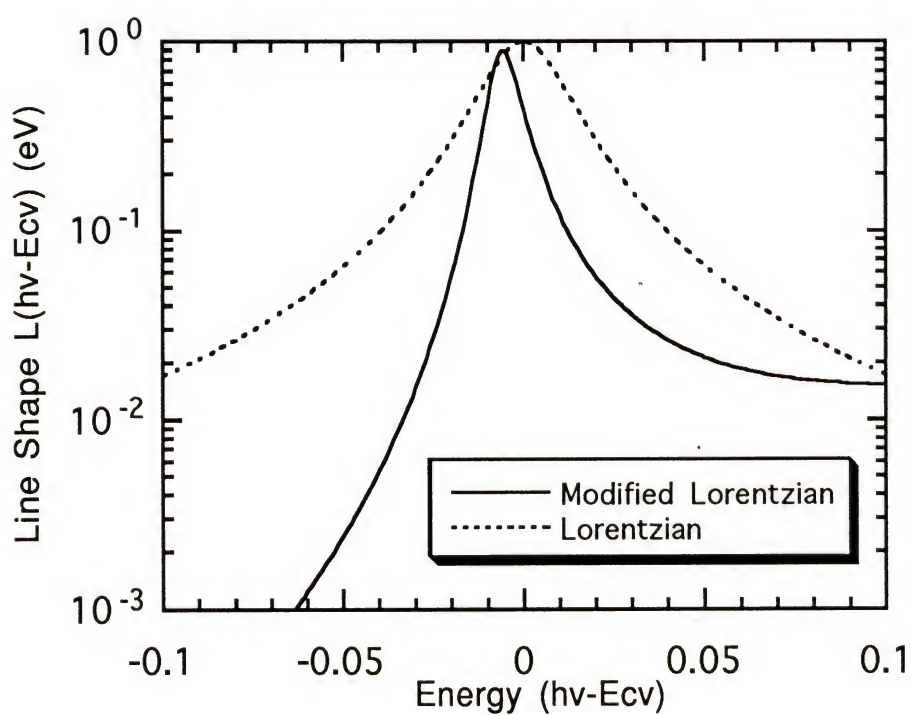


Figure 4.5 Calculated results of Lorentzian and modified Lorentzian line shape function at 300K for 65Å CdZnSe quantum well lasers. The scattering time is assumed 60 femtoseconds.

Lorentzian line shape is narrower and the low energy tail is much steeper than the Lorentzian; it decays exponentially. In calculating the line shapes in Fig. 4.5, the scattering time of 60 femtoseconds is assumed from a recent experimental result [Nurm 93]. This is a significantly shorter scattering time compared to conventional III-V materials. Since the scattering time is a function of temperature, the line shape changes at different temperatures. The variation of the scattering time with temperature is caused by the thermal distribution of the carriers and the inverse screening length  $\alpha$  which is defined in Eq. (4.8). For the calculation of the scattering time of  $\text{Cd}_{0.2}\text{Zn}_{0.8}\text{Se}$  QW lasers as a function of temperature, the data point of 60 femtoseconds at 300K was assumed and extrapolated. The results are shown in Fig. 4.6. The lineshapes for various temperatures were then calculated for hole-hole scattering. The parameters used for  $\text{Cd}_{0.2}\text{Zn}_{0.8}\text{Se}$  are listed in Table 4.1 and the lineshape for  $n=1$  transition at 85K, 150K, and 300K are shown in Fig. 4.7. The line shape functions are normalized so that the area under the curve is unity. As could be expected, the line shape function becomes narrower at low temperature which implies less spectral broadening of optical gain and spontaneous emission rate.

#### 4.4 Temperature Dependence of The Threshold Current Density of CdZnSe Blue-Green Quantum Well Lasers

Using the modified line shape function in section 4.3, the spectral gain was convolved in order to take into account the intraband relaxation which

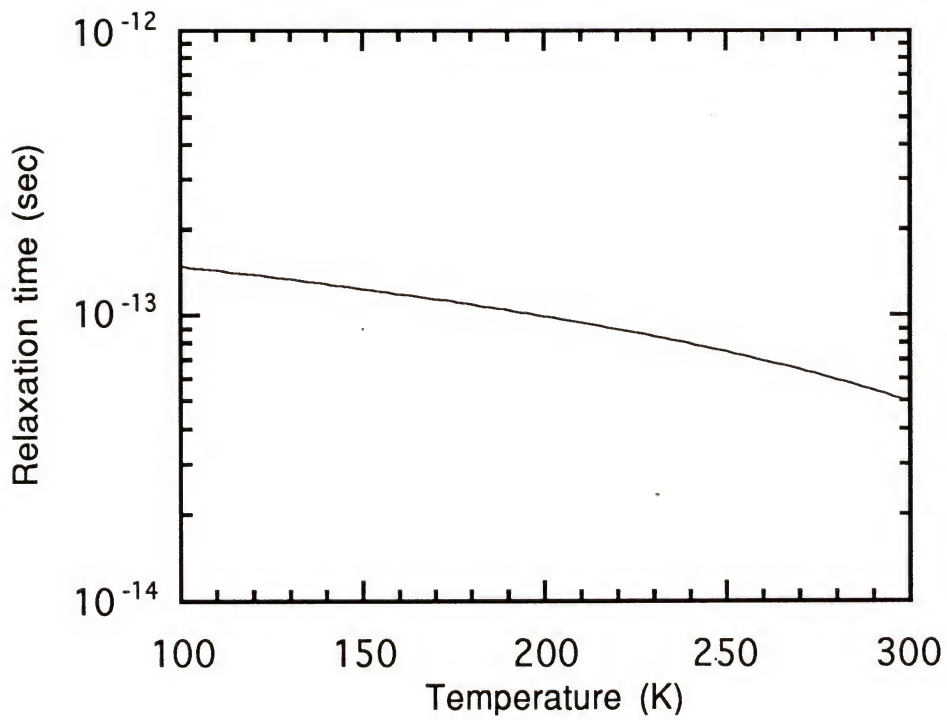


Figure 4.6 The calculated temperature dependence of scattering time of CdZnSe 65Å QW diode lasers. The data point of 60 femto-seconds at 300K was used as a fitting parameter.



Table 4.1  
Parameters of the  $\text{Cd}_{0.2}\text{Zn}_{0.8}\text{Se}$  65Å QW Lasers

$m_c$	$m_{hh}$	$m_{lh}$	$L_{c1}$	$L_{c2}$	$L_{v1}$	$L_{v2}$	$n$	$\Delta$
0.17mo	0.78mo	0.145mo	120Å	140Å	75Å	115Å	2.825	0.45eV

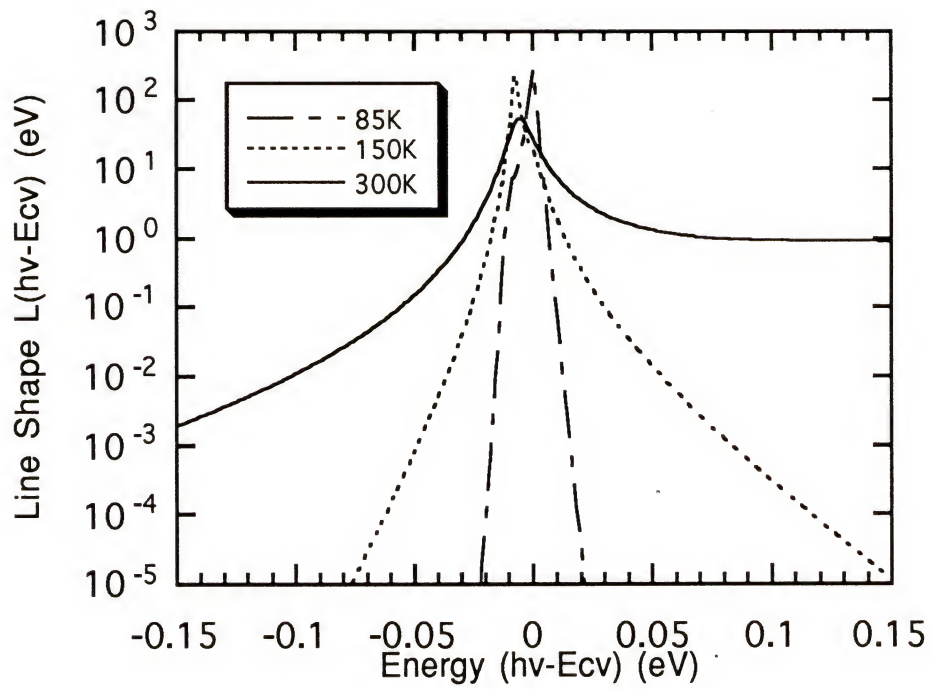


Figure 4.7 The modified line shape functions at various temperatures for CdZnSe 65Å QW laser.

gives rise to the spectral broadening of each transition. The intraband relaxation effect is taken into account in the gain calculation as follows:

$$g_c(h\nu) = \int_{E_g}^{\infty} g(E_{cv}) L(h\nu - E_{cv}) dE_{cv} \quad (4.10)$$

where  $g_c(h\nu)$  is the spectral gain including the effect of the intraband relaxation,  $E_g$  is the energy gap between the quantized energy levels of the conduction and valence band,  $h\nu$  is the photon energy,  $E_{cv}$  is the transition energy, and  $g(E_{cv})$  is the spectral gain without the intraband relaxation which is expressed in Eq. (4.4). The convolved gain  $g_c$  at a specific photon energy  $h\nu_0$  is determined by the sum of the unconvolved gain  $g$  multiplied by the lineshape function  $L$ . As a weighting factor, the line shape function  $L$  is maximum at the photon energy  $h\nu_0$  and decreasing for photon energies away from  $h\nu_0$ . However,  $g(h\nu)$  has a negative value at large photon energies as can be seen in Fig. 4.4 and the negative values are also included in the summation. Those negative terms are diverging because the weighting factor  $L$  approaches zero faster and hence, the total sum of the negative value is finite. The contribution of the finite negative sum gives rise to the decrease of the peak gain. Also it should be noted that the gain does not necessarily vanish for the photon energies less than  $E_g$  which was forbidden for unconvolved gain  $g$ . The convolved and unconvolved gain spectra of  $\text{Cd}_{0.2}\text{Zn}_{0.8}\text{Se}$  are shown in Fig. 4.8. It would be worth-while to consider the physical significance of the numerical result of the convolution. Without

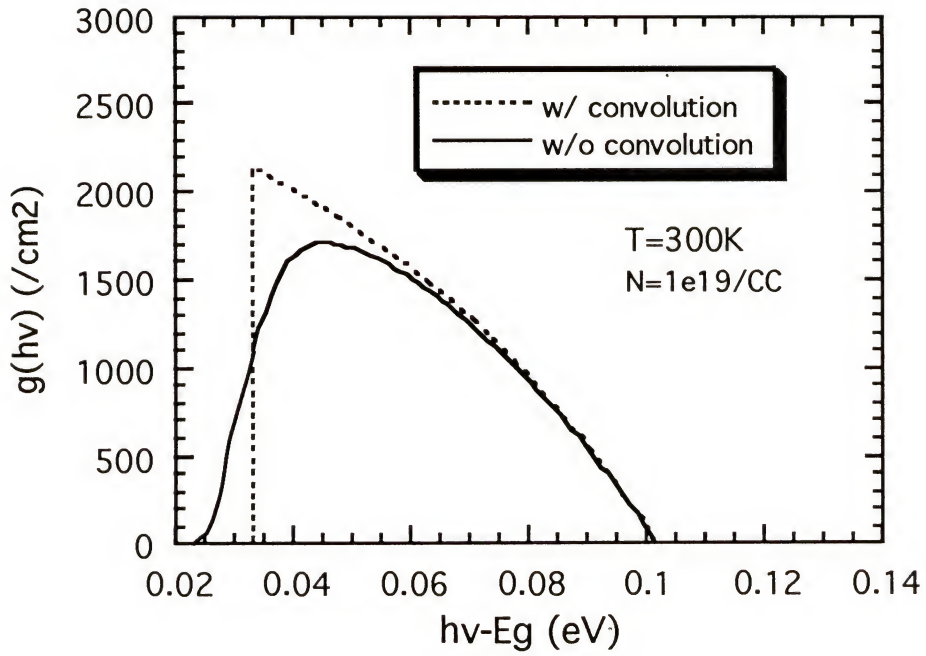


Figure 4.8 The convolved and unconvolved spectral gain of CdZnSe 65Å QW diode lasers at 300K for carrier density  $1\text{e}19\text{cm}^{-3}$ .



convolution, the gain is determined solely by the carrier distribution in the band and the transition matrix element which was discussed in chapter III. Without scattering, the carrier distribution in  $k$  space does not change in the steady state. In this situation, the carrier transition for the specific photon energy  $h\nu_0$  only occurs between electrons and holes for corresponding in-plane  $k$  vector  $k_0$ . However, with the carrier scattering included, the electrons and/or the holes which were not originally at  $k_0$ , contribute to the transition for the photon energy  $h\nu_0$  as illustrated in Fig. 4.9. Suppose that a transition with larger photon energy  $h\nu'$  at  $k'$  gives rise to a negative gain without convolution as shown in Fig. 4.10. The electrons or holes which were not involved in the transition at  $k=k_0$  when the scattering was neglected now contribute to the gain calculation through the convolution integral Eq. (4.10). Some of them may have larger  $k$  value than  $k'$  and hence correspond to a larger photon energy than  $h\nu'$  which gives rise to a negative gain. These negative gain terms are also weighted and included in the gain for the photon energy  $h\nu_0$ . This is why the convolved gain is smaller than the unconvolved one in spite of the momentum and the energy conservation of the carrier scattering process. Another important feature in Fig. 4.8 is that near the photon energy where the gain is zero ( $E'=h\nu'$  in Fig. 4.10), the convolved and unconvolved gain spectra coincide as opposed to Chinn *et al* [Chin 89]. This is a logical consequence because around  $k'$ , the contribution from either side (positive and negative gain) due to the scattering is about the same. If the

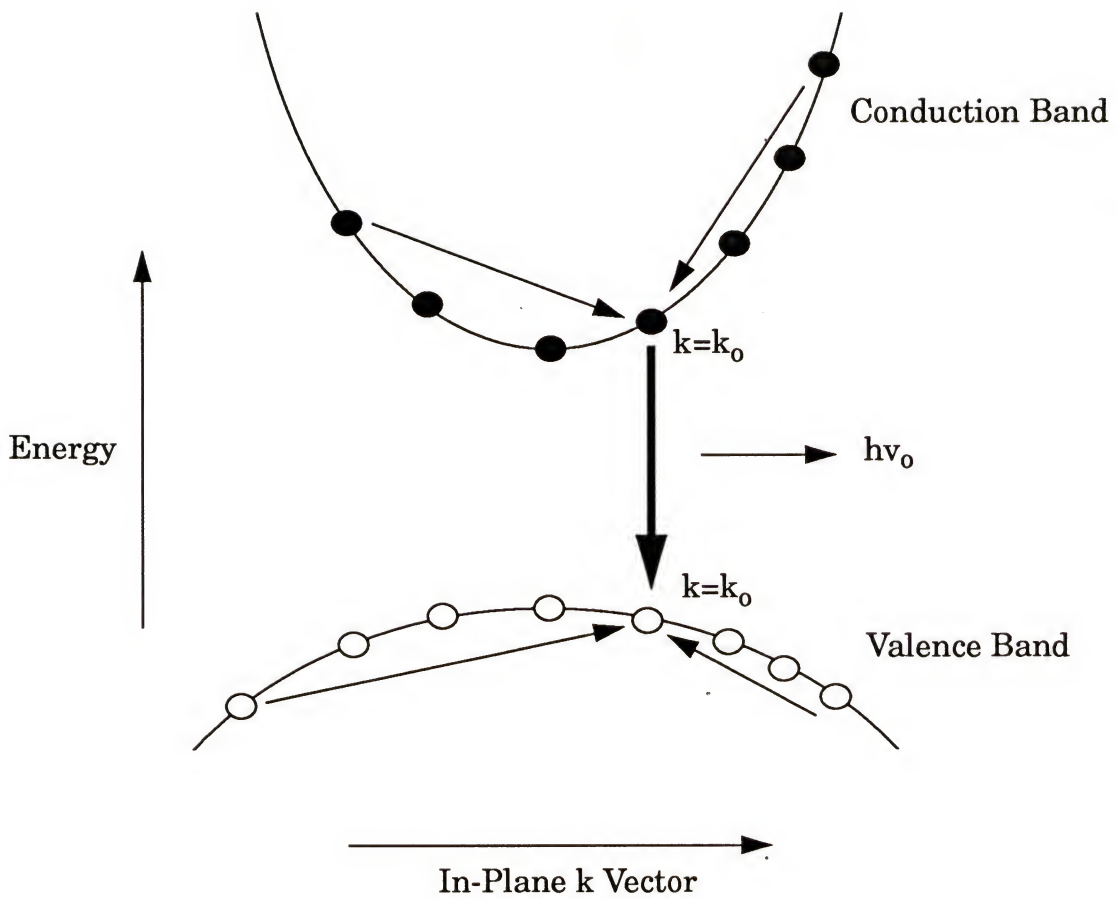
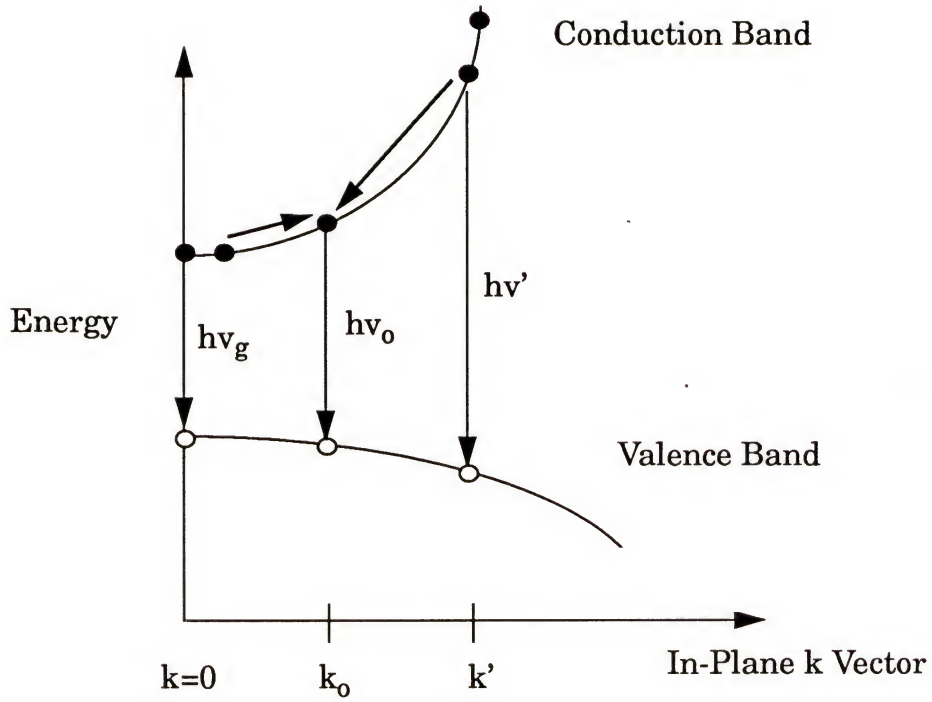
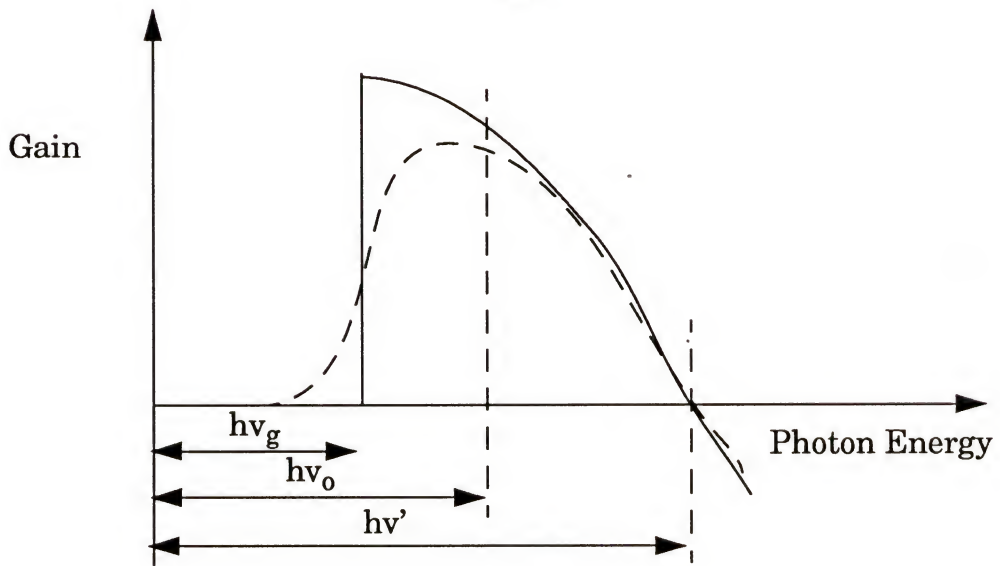


Figure 4.9 Schematics of carrier scattering in conduction and valence band.



(a)



(b)

Figure 4.10 Schematic illustrations of the effect of intraband scattering on spectral gain.

line shape function is perfectly symmetric, the cross point  $k'$  will be exactly the same provided that the gain decreases linearly around  $k'$ . Although the modified line shape function used here is asymmetric, it converges much faster than a conventional Lorentzian so the cross points are still quite close. If the line shape function did not converge fast, the large negative part of gain for  $k$  larger than  $k'$  would exceed the positive contribution. In this case, the cross point would have a smaller  $k$  than the unconvolved one.

In order to predict the threshold current density, the convolved gain  $g_c$  and the corresponding current density ( $J$ ) are determined the  $g$ - $J$  method as following procedure:

- 1) Specify carrier density  $N$  and temperature  $T$ .
- 2) Calculate the spectral dependence of the spontaneous recombination rate ( $r_{sp}(h\nu)$ ) and the convolved spectral gain ( $g_c(h\nu)$ ) and determine the peak gain  $g_{peak}$ .
- 3) Integrate  $r_{sp}(h\nu)$  to find the current density  $J$  corresponding to that value of  $g_{peak}$ .

The spontaneous recombination rate is related to current density  $J$  by

$$J = \frac{ed}{\eta_{sp}} \int r_{sp}(h\nu) d(h\nu) \quad (4.11)$$

where  $d$  is the active layer thickness and  $\eta_{sp}$  is the efficiency for converting  $J$  into spontaneous emission in the active layers. We assumed  $\eta_{sp} \approx 1$  which is a good approximation for long cavity laser at low temperature. The



schematic illustrations of the g-J method are shown in Fig. 4.11. From these relationships, we derived the peak gain vs. J for CdZnSe as shown in Fig. 4.12

Based on the g-J diagram, we found  $J_{th}$  by estimating the threshold mode gain ( $G_{th}$ ) which is given by

$$G_{th} = \Gamma g_{th} = \alpha_i + \frac{1}{L} \ln \frac{1}{R_1 R_2} \quad (4.12)$$

where  $\alpha_i$  is the mode loss coefficient, L is the cavity length,  $\Gamma$  is the mode confinement factor in the QW, and  $R_1, R_2$  is the facet refractivity. The calculated mode intensity profile for the CdZnSe structure in Fig. 2.5 is shown in Fig. 4.13. Those parameters used in the calculation are  $\alpha_i = 8.1 \text{ cm}^{-1}$ ,  $L = 1000 \text{ } \mu\text{m}$ ,  $R_1 = R_2 = 0.23$ , and  $\Gamma = 0.017$ . In our estimation,  $G_{th}$  was  $18.6 \text{ cm}^{-1}$  and hence  $g_{th}$  was  $1100 \text{ cm}^{-1}$ . In terms of the optical confinement point of view,  $\Gamma$  of the device structure shown in Fig. 2.5 was enhanced by about 25% compared to the first demonstrated blue-green laser ( $\Gamma = 0.0136$ ) [Haas 91] owing to the lower refractive index of the ZnSSe cladding layer.

The threshold current density was determined by the g-J curve and the estimated  $g_{th}$ . The theoretical values of  $J_{th}$  at various temperatures are compared with experiment as shown in Fig. 4.14. The predicted values agree well with the experiment up to 300K. Above 300K, the measured  $J_{th}$  was much higher than predicted, the discrepancy being due most likely to carrier leakage. One striking result is that the difference of the contour between the

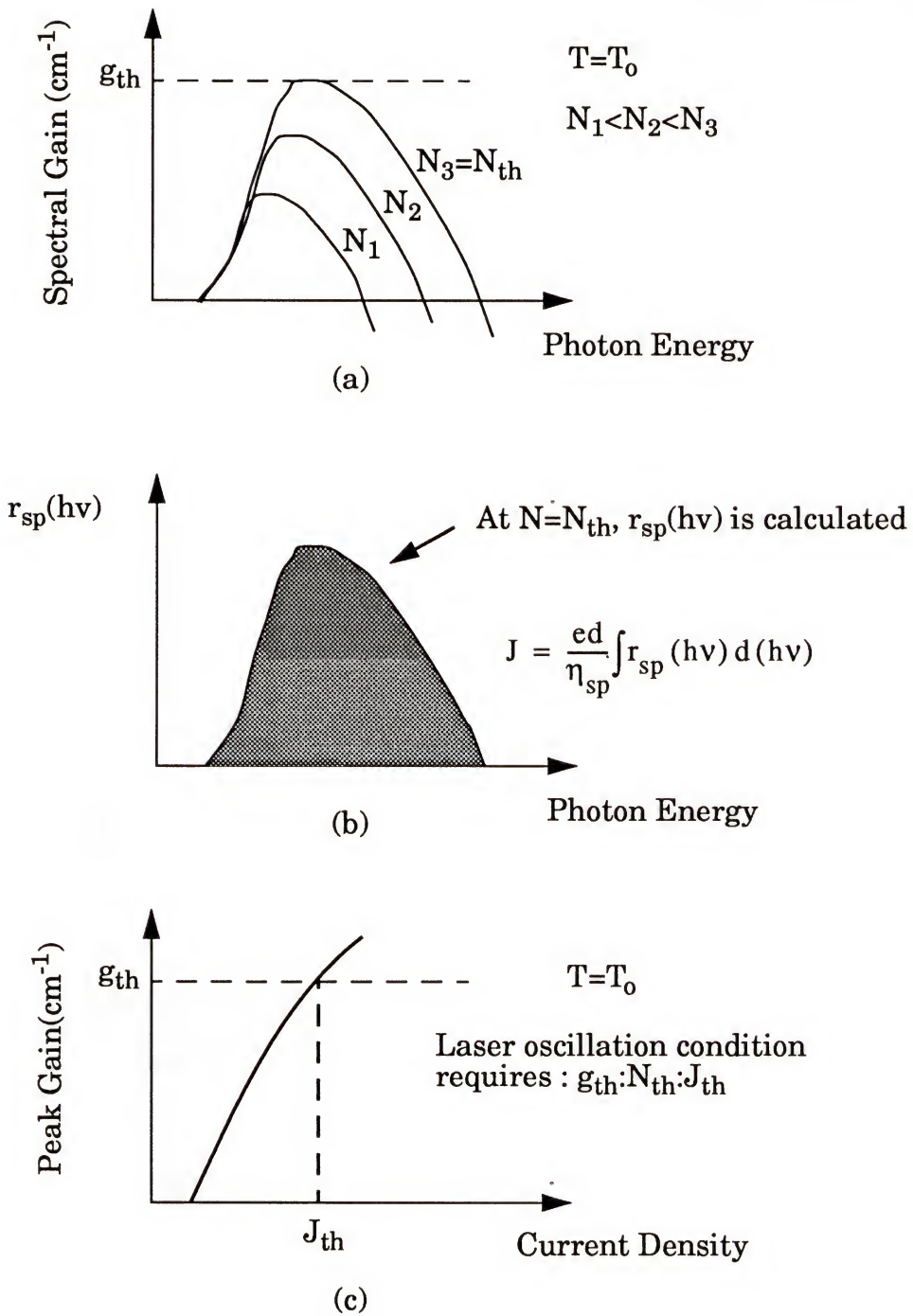


Figure 4.11 Schematics of the g-J method; (a) the spectral gain at various carrier densities (b) the relation between  $J$  and  $r_{sp}(h\nu)$  (c) the g-J curve

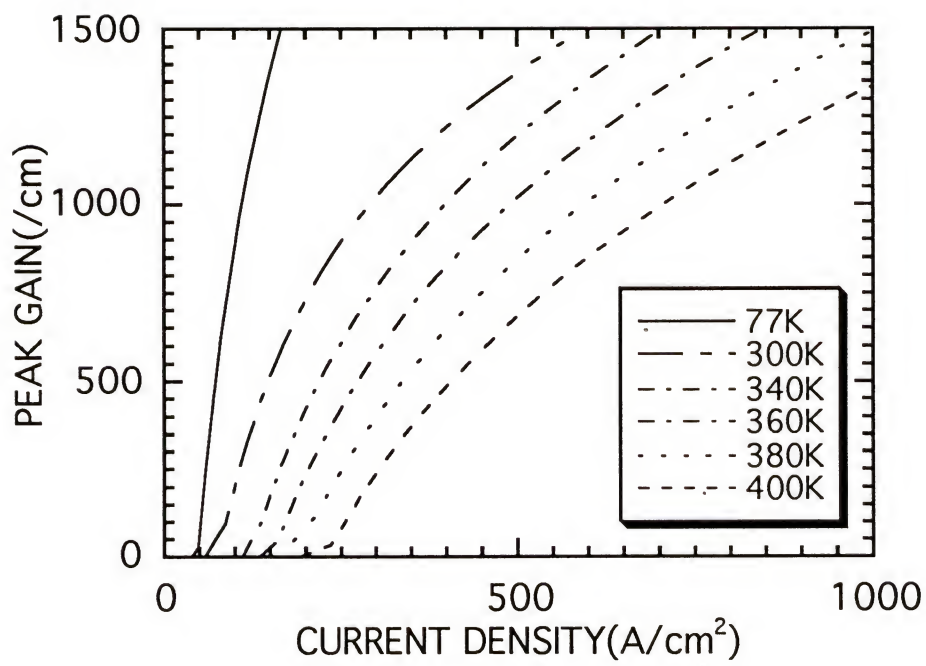


Figure 4.12 The peak gain vs. current density of  $\text{Cd}_{0.2}\text{Zn}_{0.8}\text{Se}$  QW lasers at various temperatures.

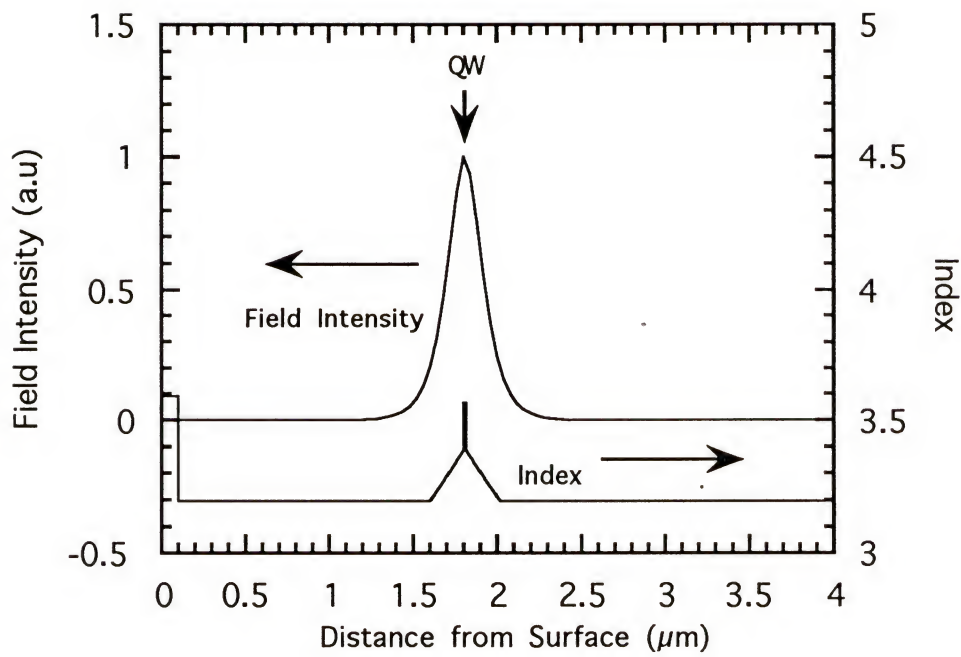


Figure 4.13 The mode intensity and the refractive index profile of  $\text{Cd}_{0.2}\text{Zn}_{0.8}\text{Se}/\text{ZnSSe}$  65Å QW lasers.



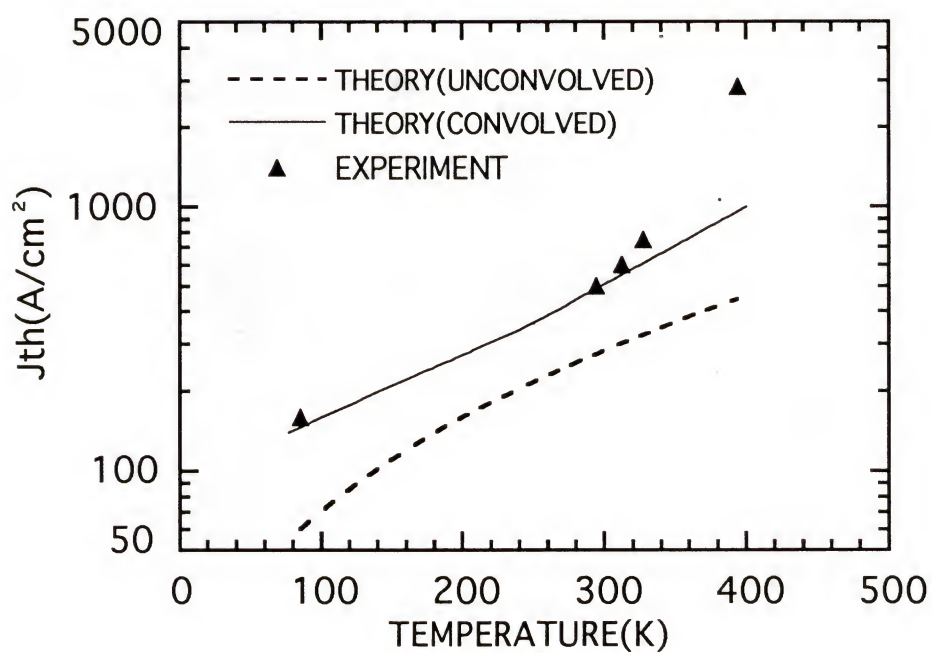


Figure 4.14 The calculated and measured temperature dependence of threshold current density of  $\text{Cd}_{0.2}\text{Zn}_{0.8}\text{Se}$  65Å QW lasers.

convolved and the unconvolved curves; the convolved curve is convex which is consistent with experimental data while the unconvolved one is concave [Park 93]. This is mainly due to the temperature dependence of the carrier scattering time. As shown in Fig. 4.6, the scattering time is exponentially decreasing as temperature increases and results in a wider line shape at higher temperature as illustrated in Fig. 4.7. As a consequence, the available peak gain diminishes by more at higher temperatures and hence, more current is required in order to reach the threshold gain which in turns increase the threshold current density.

#### 4.5 Summary

The conventional electron hole plasma (EHP) model, that optical gain is derived from k-conserved stimulated processes between free electrons and holes in quantum well subbands, has been used to predict the threshold current density of CdZnSe single quantum well lasers and good agreement with experiment was obtained up to 300K provided a hole-hole scattering time of 60 femtoseconds is assumed. Above 300K, the measured threshold current density was much higher than predicted, the discrepancy being due most likely to carrier leakage. A modified Lorentzian line shape function was used to include the intraband relaxation process caused by carrier scattering. The modified Lorentzian line shape function for the two dimensional system (QW) was much narrower than the conventional Lorentzian. The line shape was a

function of temperature and showed a stronger convergence characteristic at low temperatures.

## CHAPTER V

### DUAL PEAK WAVELENGTH OPERATION OF AlGaAs AND CdZnSe QW LASERS

#### 5.1 Introduction

The temperature dependence of threshold current in quantum well lasers can be quite complex. For example, in certain temperature ranges, single quantum well (SQW) GaAs lasers will show characteristic temperature ( $T_0$ ) discontinuities accompanied by large jumps in operating wavelength [Zory 86]. Despite the complexity of these phenomena, it has been possible to model them successfully by assuming that the optical gain is derived from k-conserved stimulated processes between free electrons and holes in quantum well subbands. As a consequence, many people now believe that this type of EHP model is the correct one to use when designing III-V QW lasers.

However, there have been reports that the optical gain in CdZnSe QW lasers is not derived from stimulated processes between free electrons and holes but between bound electron and holes or excitons [Ding 90, Ding 92, Pele 92]. As evidence, measurements of absorption spectra of quasi-three dimensional (active layer thickness  $d=200\text{\AA}$ ) and two dimensional (active layer thickness  $d=30\text{\AA}$ ) samples at various temperatures were used [Ding 90]. It has been observed that the dominant exciton peak at low temperature dis-



appeared at about 200K for  $d=200\text{\AA}$  sample while the  $n=1$  HH transition peak remains distinct at temperatures well beyond room temperature for  $d=30\text{\AA}$  sample. However, it should be noted that the step like nature of the density of state of a QW structure could give rise to such an absorption peak which can be observed even above room temperatures. In fact, those peaks have also been observed for GaAs QW structures, and hence it is questionable if an “excitonic gain (EX)” model rather than the EHP model would be appropriate for designing CdZnSe QW lasers. As shown in the previous section, the EHP model can be used to make quite accurate predictions of the temperature dependence of  $J_{th}$  for CdZnSe QW lasers. To further investigate the ability of the EHP model to predict QW lasing phenomena in CdZnSe lasers, we decided to see if we could obtain dual wavelength operation (simultaneous  $n=1$  and  $n=2$  transition lasing). In order to make sure that our predictive capabilities and experimental techniques were correct, we decided to first obtain dual wavelength operation on AlGaAs QW lasers.

## 5.2 Dual Peak Wavelength Operation of AlGaAs QW Lasers

For GaAs QW lasers, it has been shown that  $n=2$  transition lasing can be achieved by increasing cavity losses sufficiently [Zory 86]. There are a number of ways to increase the cavity losses; make the cavity length short, increase the device temperature, or make a stripe width narrower, etc. Utilizing short cavity lasers, a thermally induced peak wavelength shift of

about 500Å was observed from 50Å AlGaAs QW diode lasers. In that experiment, the peak wavelength shift occurred between 58°C and 60°C. In order to make the wavelength switching occur at low carrier densities at room temperature, a thicker AlGaAs QW laser (thickness=160Å) was chosen as shown in Fig. 5.1. The energy dispersion was calculated using multiband effective mass theory ( $\mathbf{k} \cdot \mathbf{p}$  method) for the valence band and the parabolic approximation for the conduction band. The results are shown in Fig. 5.2. In order to increase the cavity losses, short cavity length lasers with various stripe widths were used. The spectral gain and spontaneous emission rate was calculated using the EHP model discussed previously. The results are shown in Fig. 5.3 and Fig. 5.4. An important feature can be found in the calculated results; at some injection level,  $N=3 \times 10^{18}/\text{cm}^3$  for instance, gain is maximum at a low photon energy ( $n=1$  transition) while the spontaneous emission rate peaks at a high photon energy ( $n=2$  transition). It means that even though spontaneous emission at  $n=2$  is dominant at this carrier density, lasing action will occur at  $n=1$ . This can be explained by appreciating the formula for the spectral gain and the spontaneous emission rate given in Eq. (4.2) and Eq. (4.4), respectively. In terms of the thermal carrier distribution, the spontaneous emission rate depends on the multiplication of the electron and hole probability distribution functions,  $f_c(1-f_v)$ . However, the spectral gain depends on the difference between the distribution functions,  $f_c-f_v$ . On the other hand, at  $N=4.4 \times 10^{18}/\text{cm}^3$ , the peak gain for  $n=1$  and  $n=2$  are

		Au Electrode
		Oxide
p+ GaAs		
p Al <sub>.55</sub> Ga <sub>.45</sub> As	1.5μm	
p Al <sub>.28</sub> Ga <sub>.72</sub> As	0.2μm	
		Al <sub>.04</sub> Ga <sub>.96</sub> As
n Al <sub>.28</sub> Ga <sub>.72</sub> As	0.2μm	160Å QW
n Al <sub>.55</sub> Ga <sub>.45</sub> As	1.5μm	
n Al <sub>.15</sub> Ga <sub>.85</sub> As	1.0μm	
n GaAs	0.5 μm	
n GaAs substrate		
		Indium Electrode

Figure 5.1 Epitaxial structure of AlGaAs 160Å QW lasers

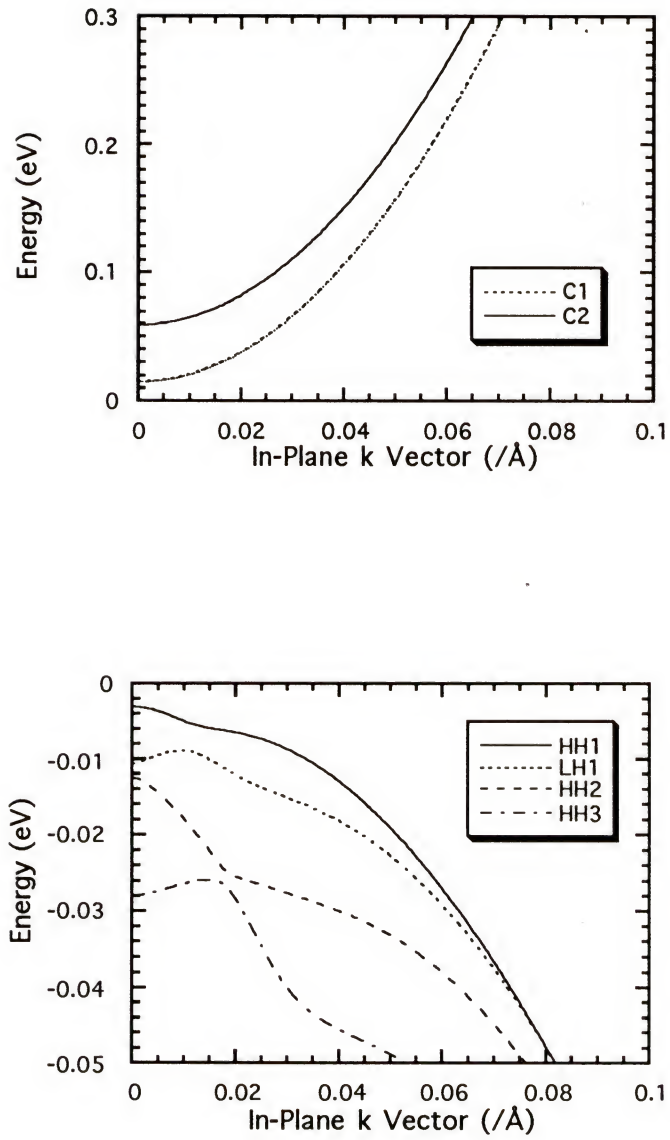


Figure 5.2 The energy vs. in-plane k vector dispersion for 160Å AlGaAs QW lasers.



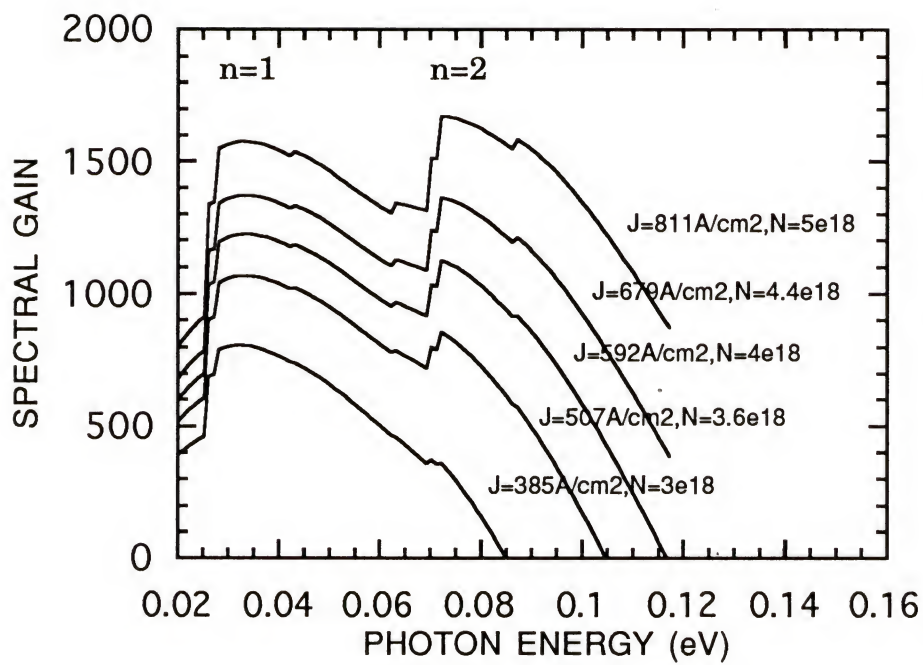


Figure 5.3 The spectral gain of AlGaAs 160Å QW lasers for various injection current at 300K.

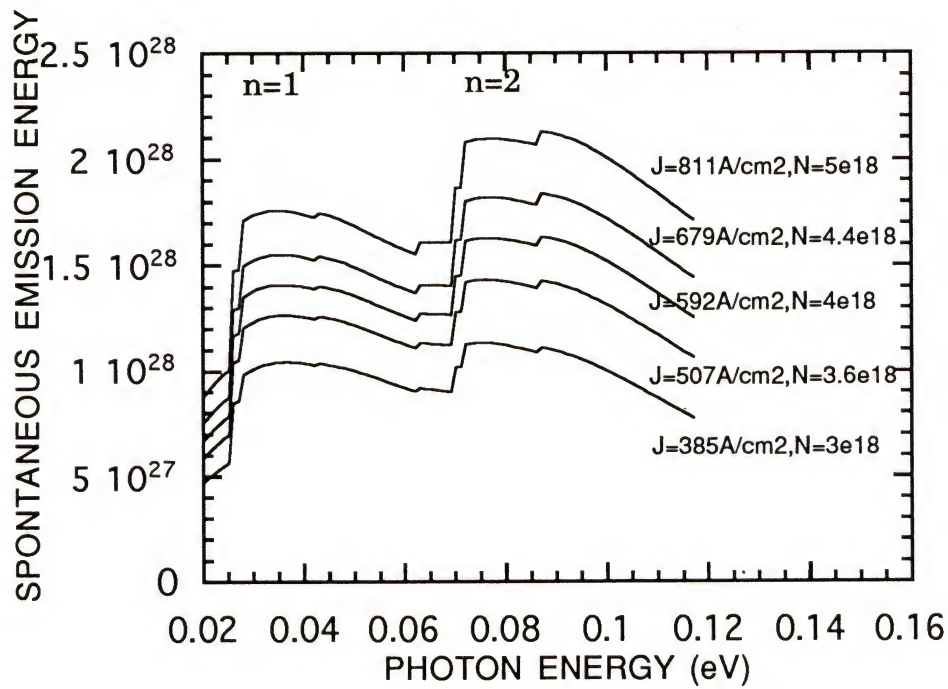


Figure 5.4 The spontaneous emission rate of AlGaAs 160Å QW lasers for various injection current at 300K.

comparable. If the peak gain at this carrier density (about  $1350\text{cm}^{-1}$ ) is about equal to the threshold gain, then it might be possible to see simultaneous lasing at  $n=1$  and  $n=2$  wavelengths. Hence, the diode laser cavity length was determined so that  $g_{\text{th}} \approx 1350\text{cm}^{-1}$  from Eq. (4.12). For this AlGaAs QW structure,  $\Gamma=0.06$ ,  $R_1=R_2=0.32$ ,  $\alpha_i=5.7\text{cm}^{-1}$ . So  $L=150\mu\text{m}$  was chosen and  $g_{\text{th}}=1360\text{cm}^{-1}$ . The measured spectra for stripe width( $w$ )  $10\mu\text{m}$ ,  $25\mu\text{m}$ , and  $50\mu\text{m}$  at various carrier densities are shown in Fig. 5.5, Fig. 5.6, and Fig. 5.7, respectively. As can be seen in the figures, it is quite clear that both the  $n=1$  and  $n=2$  peak wavelengths compete at low current injection level. As the current is increased, one of the transitions becomes more distinct. At high injection, lasing action was observed at  $775\text{nm}$  for narrow stripe lasers ( $w=10\text{nm}$ ), while for the wide stripe lasers, lasing occurred at  $800\text{nm}$ . This peak lasing wavelength difference ( $25\text{nm}$ ) corresponds to the energy difference between the maximum peak gains for  $n=1$  and  $n=2$  shown in Fig. 5.3. The peak wavelength difference between the wide and the narrow stripe lasers can be explained in terms of lateral (along the junction plane) mode confinement. In the estimation of the confinement factor  $\Gamma$ , only transverse (perpendicular to the junction) confinement was considered. It is a good assumption that the field intensity is well confined in the lateral direction for wide stripe lasers, but not for a narrow stripe laser in a gain guiding structure. For narrow stripe lasers, there can be a sizable mode loss in the lateral direction and hence, effectively,  $\Gamma$  in Eq. (4.12) decreases. As a

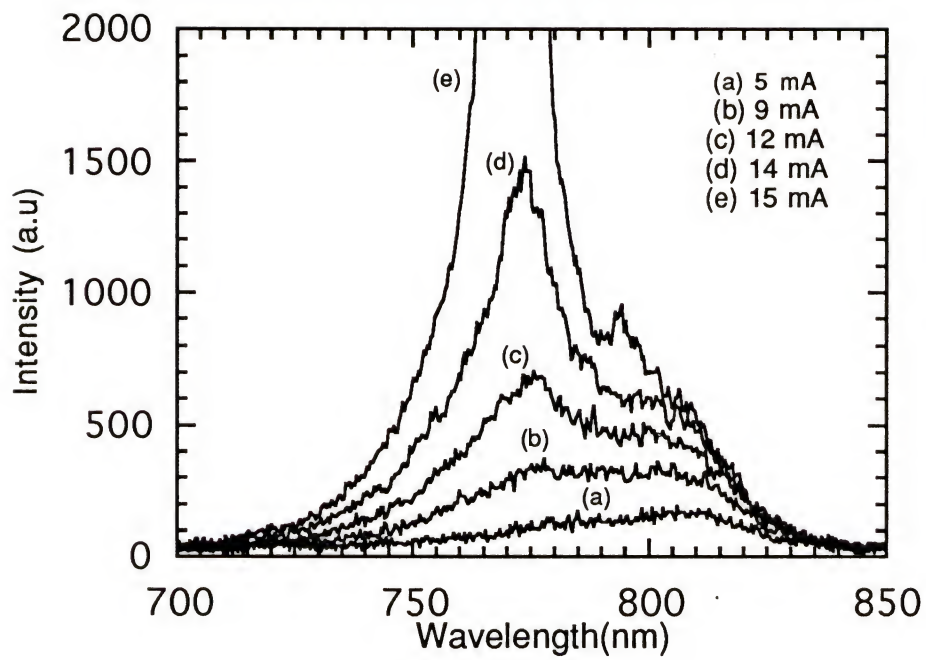


Figure 5.5 The measured spectrum of AlGaAs 160Å QW lasers for  $L=150\mu\text{m}$ ,  $w=10\mu\text{m}$  at 300K.



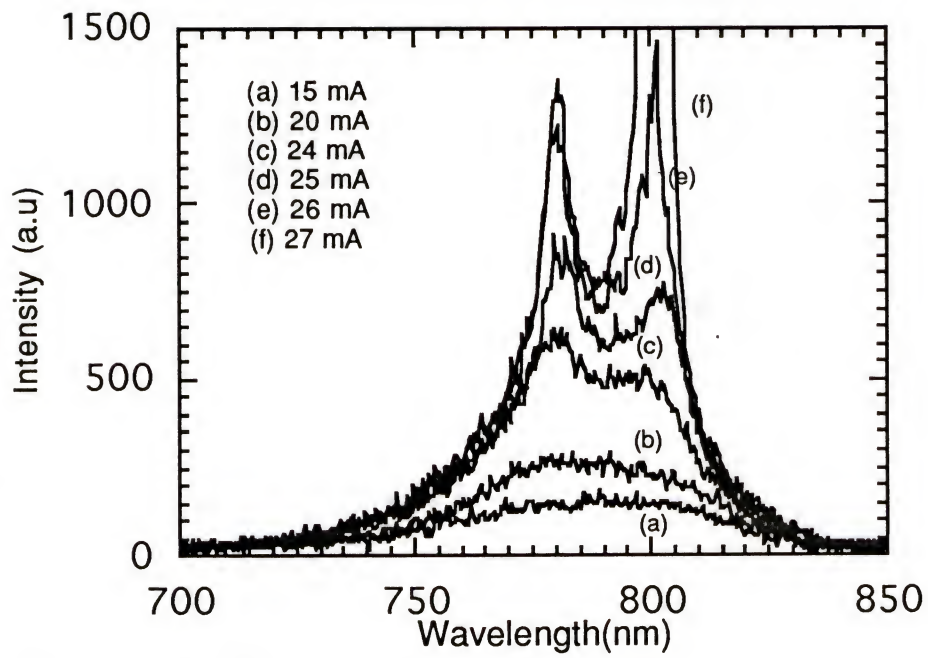


Figure 5.6 The measured spectrum of AlGaAs 160Å QW lasers for  $L=150\mu\text{m}$ ,  $w=25\mu\text{m}$  at 300K.

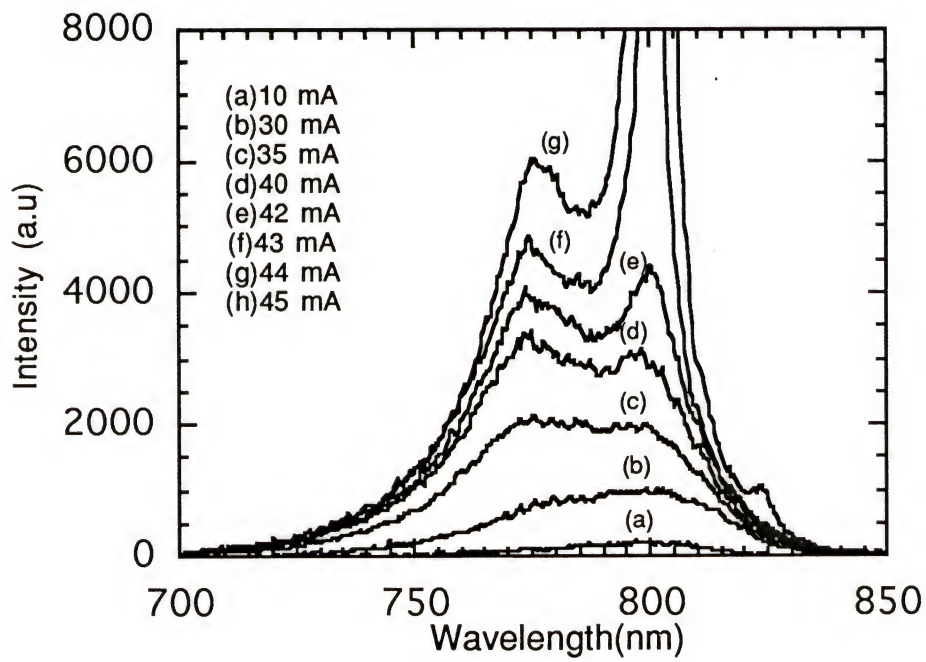


Figure 5.7 The measured spectrum of AlGaAs 160Å QW lasers for  $L=150\mu\text{m}$ ,  $w=50\mu\text{m}$  at 300K.

consequence, for a fixed threshold mode gain  $G_{th}$ , more peak gain is required to compensate the reduced effective confinement factor for narrow stripe lasers. The cavity length was decided so that both  $n=1$  and  $n=2$  peak gains reach  $g_{th}$  simultaneously for wide stripe lasers as is the case for  $w=25\text{nm}$  and  $w=50\text{nm}$ . For narrow stripe lasers, larger peak gain is required in order to compensate the lateral mode loss and such gain is achieved by  $n=2$  transition as can be seen in Fig. 5.3.

### 5.3 Dual Peak Wavelengths of CdZnSe QW Lasers

In order to reproduce a similar experiment for ZnSe based QW lasers, thinner QW thickness ( $100\text{\AA}$  instead of  $160\text{\AA}$ ) was selected because the effective masses of ZnSe are heavier than those of GaAs, and hence the spacing between each quantized energy levels is smaller for same thickness. The effective masses of GaAs and ZnSe are shown in Table 4.1. The laser material used in this experiment was grown by 3M Photonics Research Laboratory using the MBE technique. The epitaxial structure is identical with their first demonstrated blue-green laser as shown in Fig. 5.8. The energy dispersion was calculated with the multiband effective mass theory and the results are shown in Fig. 5.9. The spectral gain was calculated based on the energy dispersion for 80K, 150K, and 300K as given in Fig. 5.10, Fig. 5.11. and Fig. 5.12. The carrier density in the calculation was selected so that both  $n=1$  and  $n=2$  peak gain have about same value. The experiment was restricted to

Table 5.1  
The effective masses and the Luttinger parameters of GaAs and ZnSe

	GaAs	ZnSe
$m_c$	$0.067m_0$	$0.17m_0$
$m_{hh}$	$0.59m_0$	$0.78m_0$
$m_{lh}$	$0.09m_0$	$0.145m_0$
$\gamma_1$	6.85	3.77
$\gamma_2$	2.1	1.24
$\gamma_3$	2.9	1.67



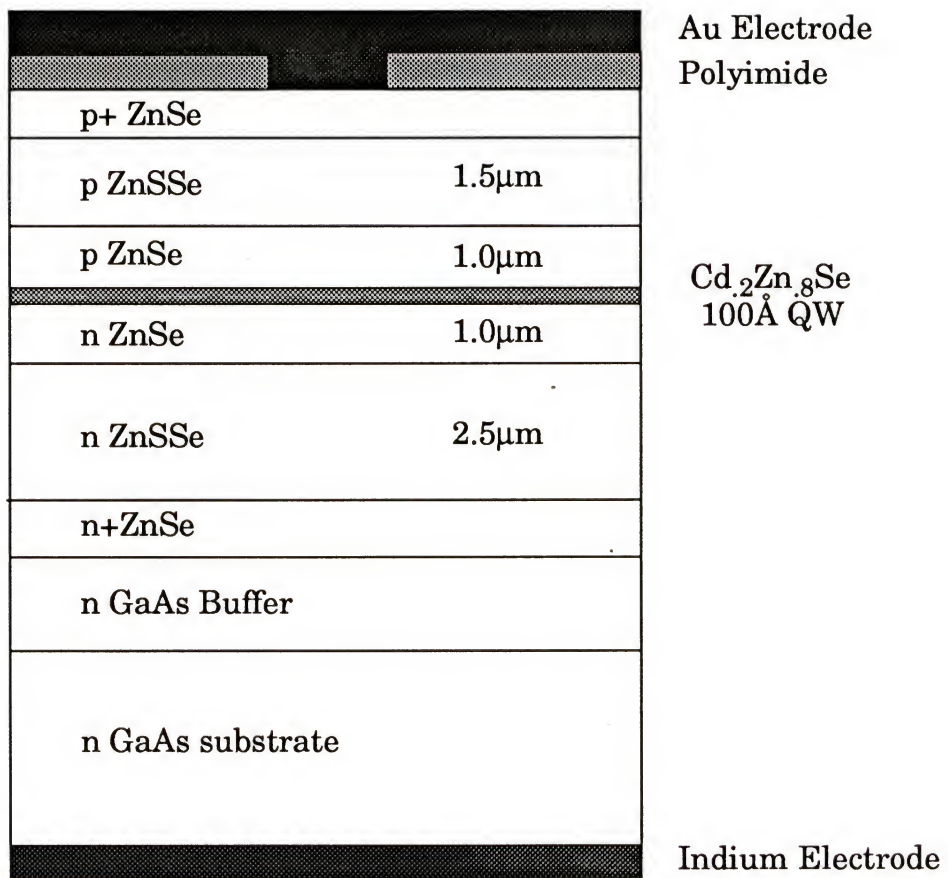


Figure 5.8 The epitaxial structure of ZnSe 100Å QW lasers.

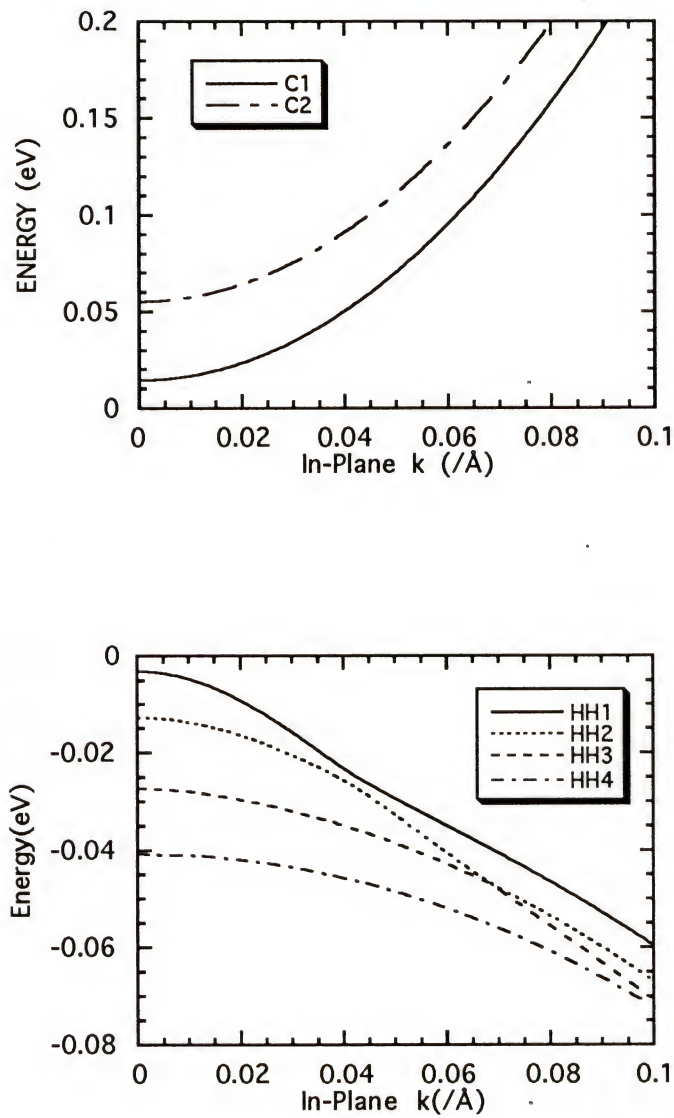


Figure 5.9 The energy dispersion of conduction and valence band of  $\text{Cd}_{0.2}\text{Zn}_{0.8}\text{Se}$  100Å QW laser

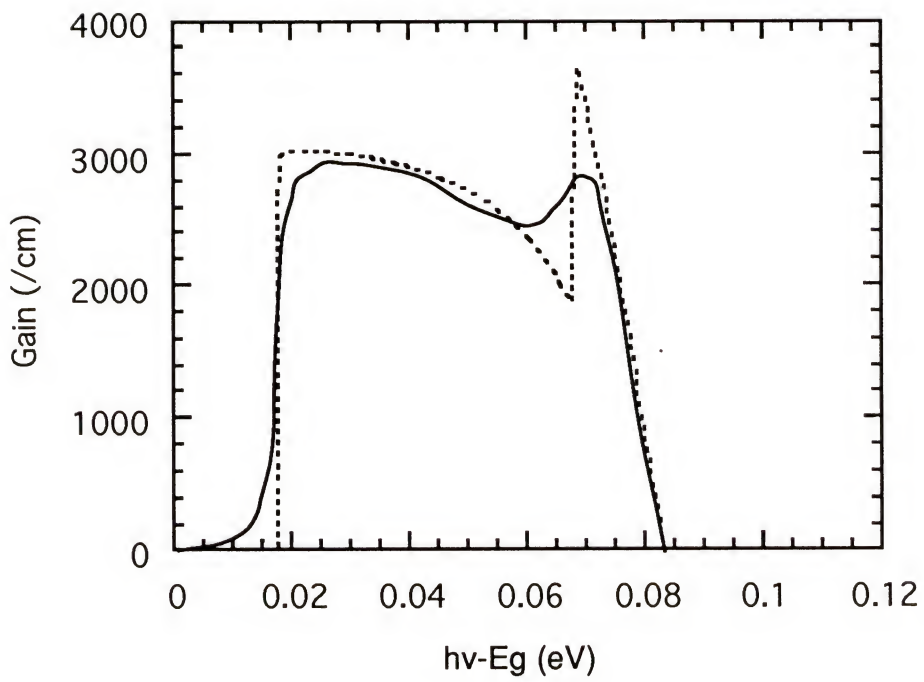


Figure 5.10 The convolved and unconvolved gain spectra of ZnSe 100Å QW lasers for  $N=4.5 \times 10^{18} \text{ cm}^{-3}$  at 80K.

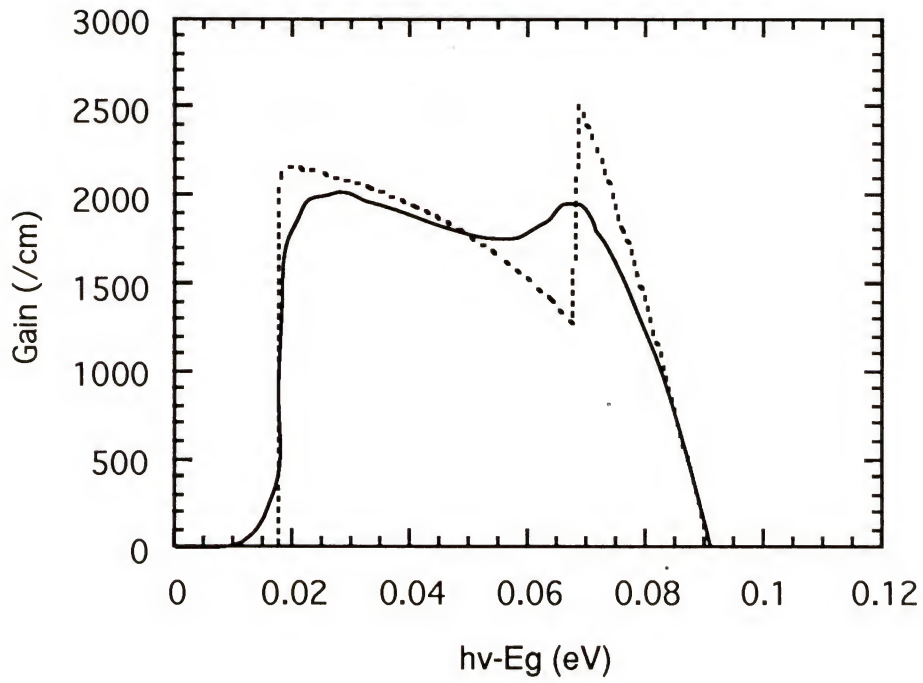


Figure 5.11 The convolved and unconvolved gain spectra of ZnSe 100Å QW lasers for  $N=6.5 \times 10^{18} \text{ cm}^{-3}$  at 150K.



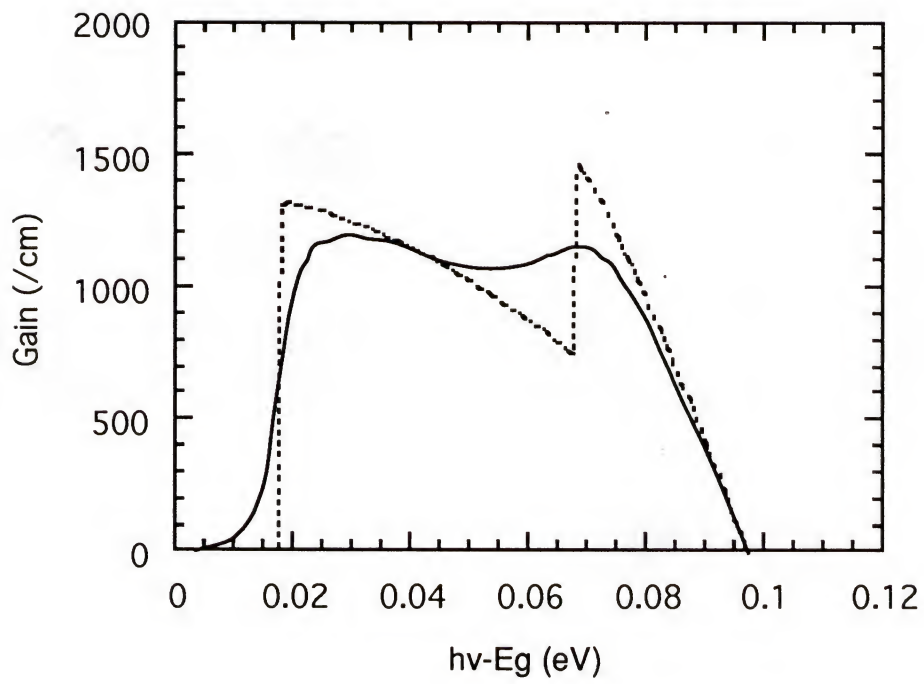


Figure 5.12 The convolved and unconvolved gain spectra of ZnSe 100Å QW lasers for  $N=9.8 \times 10^{18} \text{ cm}^{-3}$  at 300K.

low temperature for the following reasons; First, the luminescence efficiency of the material is poor and it did not lase at room temperature. Secondly, the carrier scattering time is much shorter at room temperature as discussed previously in section 4.3. The resulting wider line shape function tends to smooth the spectral gain curve to the point where the  $n=1$  and  $n=2$  transitions cannot be resolved. In a similar procedure with AlGaAs 160Å QW lasers discussed previously, CdZnSe diode lasers were designed so that both the  $n=1$  and  $n=2$  gain peaks have the same value at threshold. From Fig. 5.10 and Fig. 5.11, the proper  $g_{th}$  was found;  $2200\text{cm}^{-1}$  for 150K, and  $3000\text{cm}^{-1}$  for 80K. These threshold gains at each temperature can be achieved by designing the cavity length accordingly. The corresponding cavity lengths are  $430\mu\text{m}$  for 80K and  $650\mu\text{m}$  for 150K. The parameters used in the estimation are  $\alpha_1=8.1\text{cm}^{-1}$ ,  $R_1=R_2=0.23$  and  $\Gamma=0.014$ . Laser diodes were fabricated using the following procedure:

#### Cleaning

- 1.TCE soft boiling 2 minutes
- 2.Acetone rinse 2 times
- 3.Methanol rinse 2 times
- 4.Nitrogen blow

#### Photolithography I

- 1.P.R Coating 5500 rpm 30 second using Photoresist AZ1400-33
- 2.Soft Bake 90C 30 minutes

3.Mask align and expose at  $20\text{mW}/\text{cm}^2$  for 25 seconds

4.Develop for 30 seconds with developer AZ 319

### Metal Deposition

Deposit  $1000\text{\AA}$  of gold using electron beam evaporator

### Metal Lift-Off

Acetone Rinse

Methanol Rinse

### Photolithography II

1.P.R Coating 5500 rpm 30 second with Photoresist AZ1400-17

2.Soft Bake at  $90^\circ\text{C}$  for 30 minutes

3.Mask align and expose at  $20\text{mW}/\text{cm}^2$  for 15 seconds

4.Develop for 20 seconds in the developer AZ 319

### Metal Deposition

Deposit Ni  $1000\text{\AA}$ /Au  $1000\text{\AA}$  using electron beam evaporator

### Cleaving

Cleave the wafer with  $250\mu\text{m}$  cavity length

The diode laser chips were scribed from the laser bars and attached on copper blocks and wire bonded. The near field pattern was measured for each sample and poor devices screened out. The samples were placed in a dewar chamber and the air pressure reduced with a cryogenic pump down to 30millitorr. Then liquid nitrogen was poured into the dewar and the chamber connected with a temperature controller unit. The spectral

measurements which showed the most evidence for dual wavelength operation are shown in Fig. 5.13 and Fig. 5.14. Although a dip can be seen in each spectra, the data was recorded at sub-lasing threshold currents. At threshold and above, dual wavelength lasing of the type demonstrated for the AlGaAs QW lasers could not be observed. The reason is due, we believe, to the fact that carrier scattering process in ZnSe based materials are much faster than in GaAs based materials.

#### 5.4 Summary

Spectral measurements were made for AlGaAs and CdZnSe QW lasers. The QW thickness and cavity length were chosen so that both  $n=1$  and  $n=2$  peak gain reached threshold at the same carrier density. For AlGaAs 160Å QW lasers, dual wavelength lasing operation was clearly seen. For CdZnSe 100Å QW lasers, those peaks were not quite distinct due to the shorter scattering time.



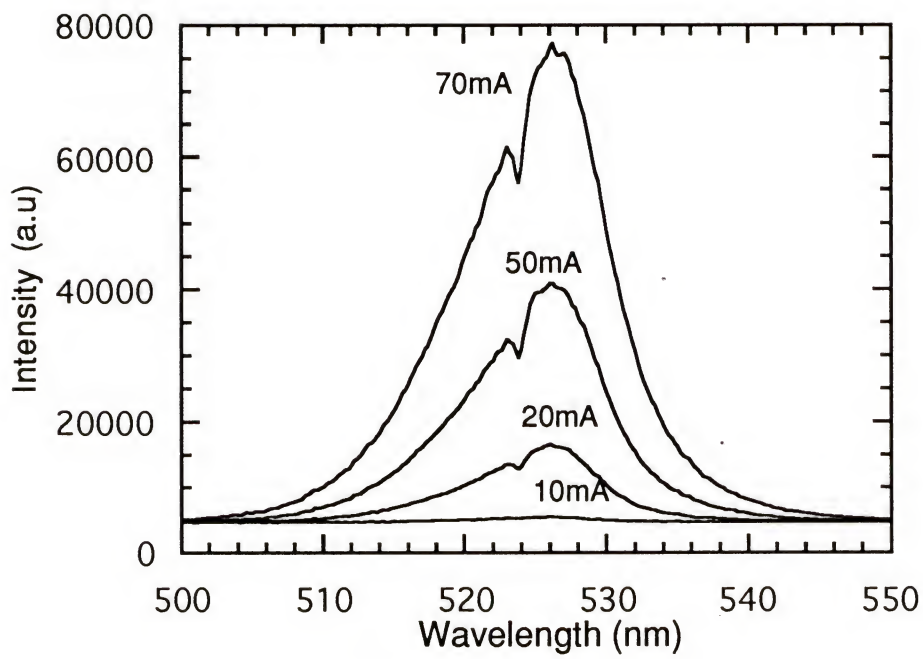


Figure 5.13 The measured spectrum of ZnSe 100Å QW lasers for various injection current at 80K. ( $L=430\mu\text{m}$ ,  $w=10\mu\text{m}$ )

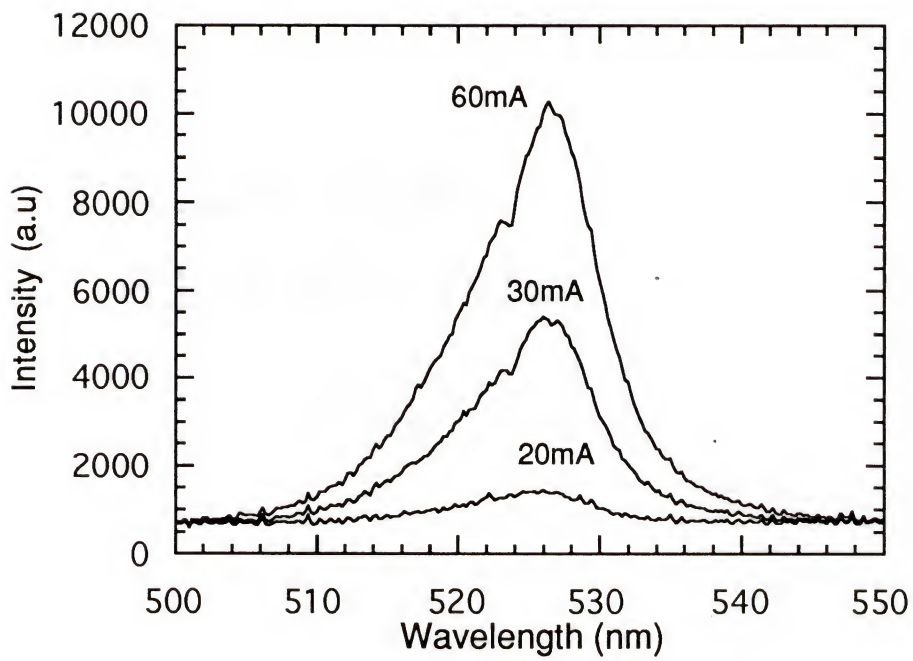


Figure 5.14 The measured spectrum of ZnSe 100Å QW lasers for various injection current at 150K. ( $L=650\mu\text{m}$ ,  $w=25\mu\text{m}$ )

## APPENDIX

For  $k=0$ ,

$$H|n, 0\rangle = E_{n0}|n, 0\rangle \quad (A.1)$$

where  $E_{n0}$  is the eigenvalue of band  $n$  at  $k=0$ . From Eq. (2.3),

$$|n, k\rangle = e^{i\mathbf{k} \cdot \mathbf{r}} |n, 0\rangle \quad (A.2)$$

Hence,

$$\begin{aligned} -i\hbar \nabla |n, k\rangle &= e^{i\mathbf{k} \cdot \mathbf{r}} (\hbar \mathbf{k} - i\hbar \nabla) |n, 0\rangle \\ -i\hbar^2 \nabla^2 |n, k\rangle &= e^{i\mathbf{k} \cdot \mathbf{r}} \left( \hbar^2 k^2 - 2i\hbar^2 \mathbf{k} \cdot \nabla - \hbar^2 \nabla^2 \right) |n, 0\rangle \end{aligned} \quad (A.3)$$

Using  $H$  from Eq. (2.1) we have

$$\begin{aligned} H|n, k\rangle &= e^{i\mathbf{k} \cdot \mathbf{r}} \left( H - \frac{i\hbar^2 \mathbf{k} \cdot \nabla}{m_0} + \frac{\hbar^2 k^2}{2m_0} \right) |n, 0\rangle \\ &= \left( E_{n0} + \frac{\hbar^2 k^2}{2m_0} \right) |n, k\rangle + \frac{e^{i\mathbf{k} \cdot \mathbf{r}} \hbar \mathbf{k}}{m_0} \cdot (-i\hbar \nabla) |n, 0\rangle \end{aligned} \quad (A.4)$$

Hence,

$$\begin{aligned} \langle n, k | H | n, k' \rangle &= \left( E_{n0} + \frac{\hbar^2 k^2}{2m_0} \right) \delta_{n, n'} \delta_{\mathbf{k}, \mathbf{k}'} + \frac{\hbar \mathbf{k}}{m_0} \cdot \langle n, 0 | e^{i(\mathbf{k} - \mathbf{k}') \cdot \mathbf{r}} (-i\hbar \nabla) | n, 0 \rangle \\ &= \left( E_{n0} + \frac{\hbar^2 k^2}{2m_0} \right) \delta_{n, n'} \delta_{\mathbf{k}, \mathbf{k}'} + \frac{\hbar \mathbf{k} \cdot \mathbf{P}_{nn'}}{m_0} \delta_{\mathbf{k}, \mathbf{k}'} \end{aligned} \quad (A.5)$$

where  $\mathbf{P}_{nn'}$  is defined in Eq. (2.5).

## REFERENCES

- [Adam 86] A. R. Adams, "Band structure engineering for low threshold high efficiency semiconductor lasers," *Electron. Lett.*, vol. 22, pp.249-250, 1986
- [Ahn 88] D. Ahn and S. L. Chuang, "Valence band mixing effects on the gain and the refractive index change of quantum-well Lasers," *J. Appl. Phys.*, vol. 64, pp.4056-4064, 1988
- [Alta 85] M. Altarelli, U. Ekenberg, A. Fasolino, "Calculations of hole subbands in semiconductor quantum wells and superlattices," *Phys. Rev. B*, vol. 32, pp.5138-5143, 1985
- [Asad 89] M. Asada, "Intraband relaxation time in quantum-well lasers," *IEEE J. Quan. Electron.*, vol. QE-25, pp.2019-2026, 1989
- [Bast 81] G. Bastard, "Supperlattice band structure in the envelope function approximation," *Phys. Rev. B*, vol. 24, pp.5693-5697, 1981
- [Bern 61] M. G. A. Bernard and G. Duraffourg, "Laser conditions in semiconductors," *Phys. Stat. Solidi*, vol. 1, pp.699-703, 1961
- [Boer 90] M. J. B. Boermans, S. H. Hagen, M. N. Finke, and J. M. M. Van der Heyden, "Investigation of TE and TM polarized laser emission in GaInP/AlGaInP lasers by growth-controlled strain," *Electron. Lett.*, vol. 26, pp.1438-1439, 1990
- [Bour 93] D. P. Bour, T. L. Paoli, R. L. Thornton, D. W. Treat, Y. S. Park, and P. S. Zory, "Polarized electroluminescence spectra of  $\text{Ga}_x\text{In}_{1-x}\text{P}/(\text{Al}_{0.6}\text{Ga}_{0.4})_{0.5}\text{In}_{0.5}\text{P}$  quantum wells", *Appl. Phys. Lett.* vol. 62, pp.3458-3460, 1993
- [Broi 85] D. A. Broido and L. J. Sham, "Effective masses of holes at GaAs-AlGaAs interface," *Phys. Rev. B*, vol. 31, pp.888-892, 1985



- [Broi 86] D. A. Broido and L. J. Sham, "Valence-band coupling and fano-resonance effects on the excitonic spectrum in undoped quantum wells," *Phys. Rev. B*, vol. 34, pp.3917-3923, 1986
- [Capa 87] F. Capaso and G. Margaritondo ed., *Heterojunction band discontinuities*, North-Holland, Amsterdam, 1987
- [Chan 77] M. Chandrasekhar and F. H. Pollak, "Effects on uniaxial stress on the electroreflectance of Ge and GaAs," *Phys. Rev. B*, vol. 15, pp.2127-2144, 1977
- [Chin 86] S. R. Chinn, P. S. Zory, A. R. Reisinger, "A model for GRIN-SCH-SQW diode lasers," *IEEE J. Quan. Electron.*, vol. QE-24, pp.2191-2214, 1988
- [Ding 90] J. Ding, N. Pelekanos, A. V. Nurmiko, H. Luo, N. Samarth, and J. K. Furdyna, "Room-temperature excitonic absorption in (Zn,Cd)Se/ZnSe quantum wells at blue-green wavelengths," *Appl. Phys. Lett.*, vol. 57, pp.2885-2887, 1990
- [Ding 92] J. Ding, H. Jeon, T. Ishihara, M. Hagerott, A. V. Nurmiko, H. Luo, N. Samarth, and J. K. Furdyna, "Excitonic gain and laser emission in ZnSe based quantum wells," *Phys. Rev. Lett.*, vol. 69, pp.1707-1710, 1992
- [Dres 55] G. Dresselhaus, A. F. Kip, and C. Kittel, "Cyclotron resonance of electrons and holes in Silicon and Germanium Crystals," *Phys. Rev.*, vol. 98, p.368, 1955
- [Gavi 70] A. Gavini and M. Cardona, "Modulated Piezoreflectance in semiconductors," *Phys. Rev. B*, vol. 1, pp.672-682, 1970
- [Gain 93] J. M. Gaines, R. R. Drenten, K. W. Haberern, T. Marshall, P. Mensz, and J. Petruzzello, "Blue-green injection lasers containing pseudomorphic  $\text{Zn}_{1-x}\text{Mg}_x\text{S}_y\text{Se}_{1-y}$  cladding layers and operating up to 394K," *Appl. Phys. Lett.*, vol. 62, pp.2462-2464, 1993
- [Gobe 85] E. O. Gobel, R. Hoger, J. Kuhl, H. J. Polland, and K. Ploog, "Homogeneous gain saturation in GaAs/AlGaAs quantum well lasers," *Appl. Phys. Lett.*, vol. 47, pp.781-783, 1985

- [Haas 91] M. A. Haase, J. Qui, J. M. DePuydt, and H. Cheng, "Blue-green laser diodes," *Appl. Phys. Lett.*, vol. 59, pp.1272-1274, 1991
- [Haas 93] M. A. Haase, P. F. Braude, M. S. Hagedorn, J. Qui, J. M. DePuydt, H. Cheng, S. Guha, G. E. Fofler, and B. J. Wu, "Blue-green buried-ridge laser diodes," *Device Research Conference Proceedings*, Boulder, 1993
- [Kane 57] E. O. Kane, "Band Structure of Indium Antimonide," *J. Phys. Chem. Solids*, vol. 1, pp.249-261, 1957
- [Kond 91] M. Kondo, K. Domen, C. Anayama, T. Tanahasi, and K. Nakajima, "MOVPE growth and optical properties of AlGaInP/GaInP strained single quantum well structures," *J. Cryst. Growth*, vol. 107, pp.578-582, 1991
- [Krij 92] M. P. C. M. Krijn, G. W. 't Hooft, M. J. B. Boermans, P. J. A. Thijs, T. van Dongen, J. J. M. Binsma, and L. F. Tiemeijer, "Improved performance of compressively as well as tensile strained quantum-well lasers," *Appl. Phys. Lett.* vol. 61, pp.1772-1774, 1992
- [Lim 91] G. Lim, Y. Park, C. A. Zmudzinski, P. S. Zory, L. M. Miller, T. L. Cockerill, J. J. Coleman, C. S. Hong, and L. Figueroa, "Predicting diode laser performance," *SPIE vol. 1418 Laser Diode Technology and Applications III*, pp.123-131, 1991
- [Lim 92] G. Lim, "On predicting the threshold current density of quantum well diode lasers," Ph. D thesis, 1992
- [Lutt 55] J. M. Luttinger and W. Kohn, "Motion of electrons and holes in perturbed periodic fields," *Phys. Rev.*, vol. 97, pp.869-883, 1955
- [Made 78] O. Madelung, *Introduction to solid-state theory*, Springer-Verlag, Berlin, 1978
- [Made 82] O. Madelung, ed., *Numerical data and functional relationships in science and technology*, Group III, vol. 17, Springer-Verlag, Berlin, 1982



- [Naga 89] R. Nagarajan, T. Kamiya, and A. Kurobe, "Band filling in GaAs/AlGaAs multiquantum well lasers and its effect on the threshold current," *IEEE J. Quan. Electron.*, vol. QE-25, pp.1161-1170, 1989
- [Nurm 93] A. Nurmikko, DARPA/ONR URI Review, unpublished, 1993
- [Ohto 91] T. Ohtoshi and M. Yamanishi, "Optical line shape functions in quantum-well and quantum-wire structures," *IEEE J. Quan. Electron.*, vol. QE-27, pp.46-53, 1991
- [Okuy 91] H. Okuyama, K. Nakano, T. Miyajima, and K. Akimoto, "Epitaxial growth of ZnMgSSe on GaAs substrate by molecular beam epitaxy," *Jpn. J. Appl. Phys.* vol. 30, pp.L1620-L1623, 1991
- [Onto 71] A. Onton, M. R. Lorentz, and W. Reuter, "Electronic structure and luminescence processes in  $\text{In}_{1-x}\text{Ga}_x\text{P}$  alloys," *J. Appl. Phys.*, vol. 42, p.3420, 1971
- [Pan 88] S. H. Pan, H. Shen, Z. Hang, F. H. Pollak, W. Zhuang, Q. Xu, A. P. Roth, R. A. Masut, V. Lacelle, and D. Morris, "Photoreflectance study of narrow-well strained-layer  $\text{In}_x\text{Ga}_{1-x}\text{As}/\text{GaAs}$  coupled multiple-quantum-well structures," *Phys. Rev. B*, vol. 38, pp.3375-3382, 1988
- [Park 90] R. M. Park, M. B. Troffer, C. M. Rouleau, J. M. Depuydt, and M. A. Haase, "p-type ZnSe by nitrogen atom beam doping during molecular beam epitaxial growth," *Appl. Phys. Lett.*, vol. 57, pp.2127-2129, 1990
- [Park 93] Y. S. Park and P. S. Zory, "Temperature dependence of the threshold current density of CdZnSe blue-green quantum well diode lasers," *LEOS Proceedings*, San Jose, pp.648-649, 1993
- [Pele 92] N. T. Pelekanos, J. Ding, M. Hagerott, A. V. Nurmikko, H. Luo, N. Smarth, and J. F. Furdyna, "Quasi-two-dimensional excitons in (Zn,Cd)Se/ZnSe quantum wells: Reduced exciton-LO-phonon coupling due to confinement effects," *Phys. Rev. B*, vol. 45, pp.6037-6042, 1992

- [Piku 60] G. E. Pikus and G. L. Bir, "Effects of deformation on the hole energy spectrum of germanium and silicon," *Sov. Phys. Solid State*, vol. 1, pp.1502-1517, 1960
- [Poll 68] F. H. Pollak and M. Cardona, "Piezo-electroreflectance in Ge, GaAs, and Si," *Phys. Rev.*, vol. 172, pp.816-837, 1968
- [Thij 91] P. J. A. Thijs, L. F. Tiemeijer, P. I. Kuindersma, J. J. M. Binsma, and T. van Dongen, "High-performance 1.5 $\mu$ m wavelength InGaAs-InGaAsP strained quantum well lasers and amplifiers," *IEEE J. Quan. Electron.*, vol. 27, pp.1426-1439, 1991
- [Van 86] C. G. Van de Walle, and R. M. Martin, "Theoretical calculations of heterojunction discontinuities in the Si/Ge system," *Phys. Rev. B*, vol. 34, pp.5621-5634, 1986
- [Van 88] C. G. Van de Walle, K. Shahzad, and D. J. Olego, "Strained-layer interfaces between II-V compound semiconductor," *J. Vac. Sci. Technol. B.*, vol. 6, pp.1350-1353, 1988
- [Van 89] C. G. Van de Walle, 'Band lineups and deformation potentials in the model-solid theory," *Phys. Rev. B*, vol. 38, pp.1871-1883, 1989
- [Wang 90] T. Y. Wang, A. W. Kimball, G. S. Chen, D. Birkedal, and G. B. Stringfellow, "Atmospheric pressure organometallic vapor-phase epitaxial growth and characterization of Ga<sub>0.4</sub>In<sub>0.6</sub>P/(Al<sub>0.4</sub>Ga<sub>0.6</sub>)<sub>0.5</sub>In<sub>0.5</sub>P strained quantum wells," *J. Appl. Phys.*, vol. 68, pp.3356-3363, 1990
- [Wang 93] M. C. Wang, K. Kash, C. E. Zah, R. Bhat, and S. L. Chuang, "Measurement of nonradiative Auger and radiative recombination rates in strained-layer quantum-well systems," *Appl. Phys. Lett.*, vol. 62, pp.166-168, 1993
- [Welc 91] M. J. Welch, T. Wang, and D. R. Scifres, "Low threshold current laser emitting at 637nm," *Electron. Lett.*, vol. 27, pp.693-694, 1991
- [Whit 81] S. White and L. J. Sham, "Electronic properties of flat band semiconductor heterostructures," *Phys. Rev. Lett.*, vol. 47, pp.879-882, 1981




- [Yabl 86] E. Yablonovitch and E. O. Kane, "Reduction of lasing threshold current density by the lowering of valence band effective mass," J. Lightwave Technol., vol. 4, pp.504-506, 1986
- [Yabl 88] E. Yablonovitch and E. O. Kane, "Band structure engineering of semiconductor lasers for optical communications," J. Lightwave Technol., vol. 6, pp.1292-1299, 1988
- [Yama 81] M. Yamada and Y. Suematsu, "Analysis of gain suppression in undoped injection lasers," J. Appl. Phys., vol. 52, pp.2653-2664, 1981
- [Yama 87] M. Yamanishi and Y. Lee, "Phase dampings of optical dipole moments and gain spectra in semiconductor lasers," IEEE J. Quan. Electron., vol. QE-23, pp.367-370, 1987
- [Zory 86] P. S. Zory, A. R. Reisinger, R. G. Waters, L. J. Mawst, C. A. Zmudzinski, M. A. Emanuel, M. E. Givens, and J. J. Coleman, "Anomalous temperature dependence of threshold for thin quantum well AlGaAs diode lasers," Appl. Phys. Lett. vol. 49, pp.16-18, 1986
- [Zory 93] P. S. Zory ed., *Quantum Well Lasers*, Academic Press, Inc., San Diego, 1993

## BIOGRAPHICAL SKETCH


Youngsoh Park was born in Seoul, Korea, in 1960. He received the B.S. degree in physics from Seoul National University, Seoul, Korea. From January 1986 to July 1988 he was with Samsung Semiconductor and Telecommunications, Kiheung, Korea, where he worked on optoelectronic devices.

He received the M.S. degree in electrical engineering from the University of Florida in 1990. Since August 1988, he has been pursuing his Ph.D. degree in Department of Electrical Engineering at the University of Florida, Gainesville, Florida, working on the III-V and II-VI semiconductor laser modeling and processing. His research interests include modification of the electronic properties in the valence band in the quantum well lasers.

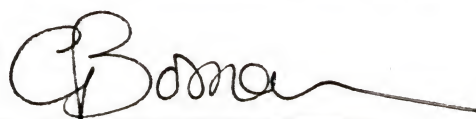
I certify that I have read this study and that in my opinion it conforms to acceptable standards of scholarly presentation and is fully adequate, in scope and quality, as a dissertation for the degree of Doctor of Philosophy.

  
Peter S. Zory, Chairman  
Professor of Electrical Engineering

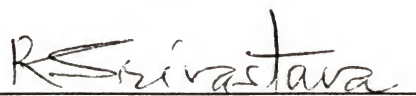
I certify that I have read this study and that in my opinion it conforms to acceptable standards of scholarly presentation and is fully adequate, in scope and quality, as a dissertation for the degree of Doctor of Philosophy.

  
Sheng S. Li  
Professor of Electrical Engineering

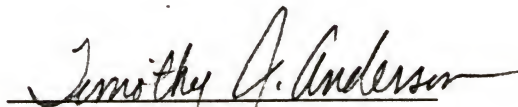
I certify that I have read this study and that in my opinion it conforms to acceptable standards of scholarly presentation and is fully adequate, in scope and quality, as a dissertation for the degree of Doctor of Philosophy.

  
Gijs Bosman  
Professor of Electrical Engineering

I certify that I have read this study and that in my opinion it conforms to acceptable standards of scholarly presentation and is fully adequate, in scope and quality, as a dissertation for the degree of Doctor of Philosophy.

  
Ramakant Srivastava  
Professor of Electrical Engineering


I certify that I have read this study and that in my opinion it conforms to acceptable standards of scholarly presentation and is fully adequate, in scope and quality, as a dissertation for the degree of Doctor of Philosophy.



Timothy J. Anderson  
Professor of Chemical Engineering

This dissertation was submitted to the Graduate Faculty of the College of Engineering and to the Graduate School and was accepted as partial fulfillment of the requirements for the degree of Doctor of Philosophy.

April 1994

fr   
Winfred M. Phillips  
Dean, College of Engineering

---

Karen A. Holbrook  
Dean, Graduate School